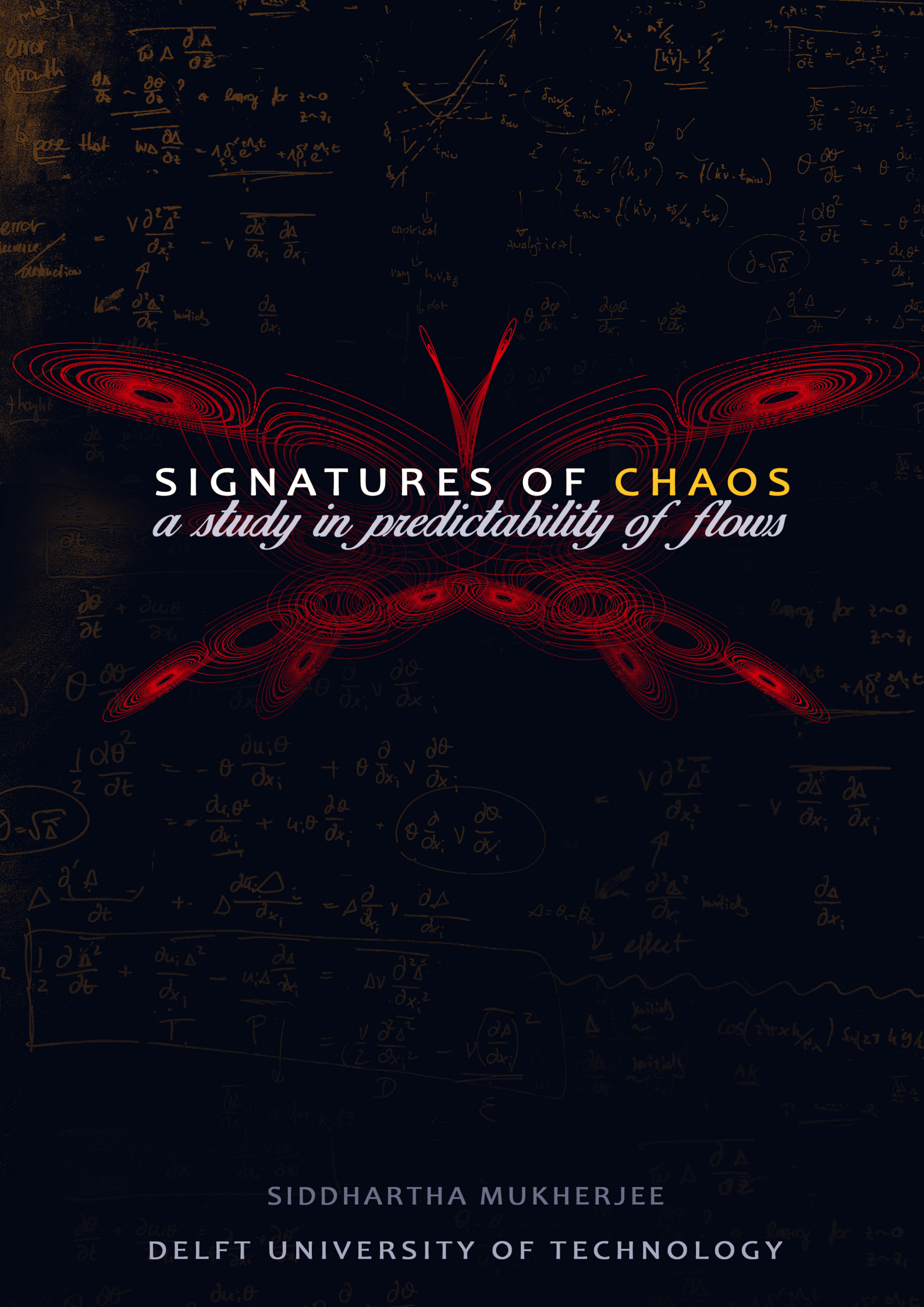

SIGNATURES OF CHAOS

a study in predictability of flows

SIDDHARTHA MUKHERJEE

DELFT UNIVERSITY OF TECHNOLOGY

SIGNATURES OF CHAOS

A study in predictability of flows

Siddhartha Mukherjee

Master's Thesis

Thesis Supervisors:
Prof.dr.H.J.J. Jonker
Ir. Jerôme Schalkwijk

Exam Committee Members:
Dr.R. Delfos
Prof.dr.H.J.J. Jonker
Dr.S.R. de Roode
Ir.Jerôme Schalkwijk

Dept. Mechanical Engineering - Solid and Fluid Mechanics
&
Dept. Geoscience and Remote Sensing - Atmospheric Physics

Delft University of Technology

Report Number:
P&E: 2647
Internal: MEAH-282

September 20, 2014

Dedicated to
The Mother

"The question is no longer *whether* God plays dice with the Universe, the question is *how* he plays it."
Ian Stewart

Abstract

This research investigates predictability in atmospheric systems. First, a study on forecasting is conducted using the Lorenz (1963) model, employing data assimilation techniques of increasing complexity, which combine model forecasts with observations for prediction. It is shown that using a fixed fraction of the model forecast with observations outperforms using observations alone. This is surpassed by ensemble spread based predictions, which assesses the model quality at each forecast interval to determine its contribution in an adaptive manner. A further improvement is seen upon using a multivariate estimate, assessing the model sensitivity individually for each variable, a method that can also aid forecasting when the observations available are incomplete. These techniques readily apply to more complicated systems and are often encountered in Numerical Weather Prediction.

Next, the Dutch Atmospheric Large Eddy Simulation (DALES 3.1.1) was adapted to investigate predictability in high resolution *Large Eddy Simulations* and *Direct Numerical Simulations* of a dry convective boundary layer. An exponential error growth similar to the Lorenz model is observed, characterized by a *Lyapunov exponent* Λ. Releasing controlled perturbations (with a fixed wavenumber k) in the potential temperature field shows, strikingly, this growth to be independent of k. Rather, the error energy spectrum rapidly attains a self similar shape dominated by the higher wavenumbers within minutes of seeding. The initial phase of error evolution is marked by a small dip due to dissipation, which depends on the initial location of the perturbation in the boundary layer and its wavenumber (where a higher k dissipates more). The error begins to grow with the fixed Lyapunov exponent after it is advected to the surface and the thermal inversion, corresponding to strong zones of variance production. Contrary to the classical notion of saturation of smaller scales at a faster pace, an octave analysis of the power spectrum evolution shows that the different scales of the system saturate at the same rate in these simulations. The value of Λ depends on the Reynolds number, increasing without signs of saturation as the flow becomes more turbulent. Further, upon changing the dynamics of the system by doubling the convective timescale $t_\star$, it is seen that the dimensionless pair $\Lambda t_\star$ remains invariant and increases linearly with the Reynolds number. Extrapolating $\Lambda t_\star$, if the curve remains consistent, to Reynolds numbers encountered in the atmosphere ($\sim 10^8$) would imply amplification of an initial error, however small, to saturation within the timescales of the smallest eddies.

Contents

List of Figures

CHAPTER 1

Introduction

The problem with accurate weather prediction has been found to be twofold. First is a limitation of computing, which although faithful to Moore's law [Moore et al., 1965] in its promise of ever increasing capacity, is simply a conceited curve bound by the second problem. It is this, fundamentally rooted in the very fabric of nature, that tends to elude a purely numeric inquiry, inciting a more elegant examination of a phenomena ubiquitous to our universe. Ever since the discovery of *chaos*, Numerical Weather Prediction (henceforth referred to as *NWP*) has transitioned in its scope from deterministic to a probabilistic estimate of the several possible states the climate can assume. This research delves into the issue of predictability in atmospheric flows by first studying the method of forecasting in a chaotic system, and then investigating predictability in high resolution numerical simulations of a turbulent atmospheric boundary layer.

1.1 Faltering Determinism

In his efforts to grossly simplify the equations governing atmospheric dynamics, Lorenz successively worked with fewer abstract equations that preserved the greater essence of the phenomena. Much into his forays in finding non periodic solutions, he finally settled for a group of three differential equations, the solutions to which showed irregular variability. To further probe the long term behaviour of the system, he once integrated the equations using his handwritten halfway values from another simulation. Startlingly, he observed that after a brief initial phase of coinciding, the solutions rapidly diverged to completely uncorrelated values, stumbling upon the system's extreme sensitivity to initial conditions[1], the hallmark of instability. He soon found that there were, in fact, an infinite number of unstable non-periodic trajectories bound by the system, smearing unpredictability onto determinism. Lorenz was quick to realize its implications on practical weather prediction. He postulated that given the ambit of atmospheric dynamics,

[1]Historically, the first mention of *sensitivity to initial conditions* can be dated back to Maxwell's essays on 'Determinism and Free Will' [Hunt and Yorke, 1993]. Maxwell luminously wrote: "When the state of things is such that an infinitely small variation of the present state will alter only by an infinitely small quantity the state at some future time, the condition of the system is said to be stable; but when an infinitely small variation in the present state may bring about a finite difference in the state of the system in a finite time, the condition of the system is said to be unstable." This notion applicable to the study of stability is often seen in chaotic systems. Poincaré's work on the celestial three body problem then showed that a solvable physical problem can still be unpredictable owing to this sensitivity to initial conditions, where small uncertainties amplify in time.

which possesses multiple scales of motion, initial errors, albeit small, would rapidly amplify and further excite larger scales of error growth. This would greatly bound the *predictability horizon*, whereby simply reducing the initial error by an arbitrary amount would not result in a comparable gain in extending predictability. This beautiful, yet unsettling discovery forms the basis of this research.

1.2 Numerical Weather Prediction and Data Assimilation

The application of numerics to predicting future states of the atmosphere can be traced back to the seminal work of Lewis Fry Richardson, compiled in his extraordinary treatise *Weather Prediction by Numerical Process* in 1922. What has been popularized by Lynch [2006] as 'Richardson's dream' is the symbiosis of numerical weather prediction and theoretical meteorology. It is since accepted that NWP is an initial/boundary value problem, i.e. given an observation of the current state of the atmosphere (which serves as initial conditions), and appropriate 'boundary conditions', a model can simulate (or forecast) the future states of the atmosphere by integrating the governing equations in time. The observational errors, however, grow over the evolution of the system, leading to exponential departures from the "true state" attained by the atmosphere after the forecasting duration. This inability of observations alone to form a robust set of initial conditions for predictions urged meteorologists to seek an alternate approach. This led to the dawn of methods that are "a statistical combination of observations and short-range forecasts" [Kalnay, 2003], now termed *Data Assimilation*, whose purpose as defined by Talagrand [1997] is "using all available information, to determine as accurately as possible the state of the atmospheric (or oceanic) flow". Model predictions and observations together comprise the *available information*, and their synthesis for initializing forecasts demonstrates better prediction capabilities than using observations alone. The first part of this study (Chapter 2) explores some Data Assimilation preliminaries, applying different methods for forecasting in the Lorenz model and testing their performance. Then, predictability is studied in a more realistic physical system that exhibits sensitivity to initial conditions, i.e the evolution of a turbulent boundary layer.

1.3 Predictability in a Turbulent Boundary Layer

Turbulence lends an inscrutable facade to fluid motion, which over the years has revealed an underlying complexity that is hard to define. An understanding of turbulence has largely been aided by experiments, both physical and numerical. High resolution CFD methods like *Large Eddy Simulations* and *Direct Numerical Simulations* have now defined the norm in studying the dynamics of boundary layers, and are being widely applied to turbulence in the atmosphere. These simulations have a very high resolution, around 4-5 orders of magnitude finer compared to their climate model counterparts, and can *resolve* turbulent motions as well as *model* them. Using these simulations for predictions, or coupling them with larger circulation models poses an exciting opportunity for high resolution forecasting. The problem of predictability in climate models has been investigated in several studies. These models, however, do not simulate turbulent motions, and error propagation in resolved 3-dimensional turbulence remains unresearched. Chapter 4 begins to address this issue by studying the evolution of controlled perturbations in high resolution *LES* of a dry convective planetary boundary layer, discussing the implications on predictability. Parameters such as the wavenumber of the perturbation, its location in the boundary layer, the flow Reynolds number etc are examined. A similar study is then extended to *DNS* simulations that resolve all the scales of turbulence in Chapter 5.

CHAPTER 2

Forecasting in the Lorenz Model

The Lorenz 3 equation model, although a simple approximation of atmospheric processes, is still highly chaotic and makes for an appropriate subject for studying the nuances of forecasting. In this chapter, Data Assimilation *(DA)* is performed on the Lorenz Model for short term forecasting. Some of the common DA methods are conceptually tested and studied in these simulations, which readily extend to more complicated models.

2.1 The Lorenz (1963) Model

We first look at the governing equations of the Lorenz Model, which arise out of a simplification of the 2-dimensional Rayleigh-Bénard convection between two heated plates.

2.1.1 The Chaotic Trinity

The system consists of the following three ODEs

$$\begin{aligned} \dot{x} &= \sigma(y - x) \\ \dot{y} &= rx - y - xz \\ \dot{z} &= xy - bz \end{aligned} \tag{2.1}$$

with the parameters $\sigma = 10$, $b = 8/3$ and $r = 28$ [Lorenz, 1963]. Here, σ is the *Prandtl number* (the ratio of momentum diffusivity and thermal diffusivity), r is the *Rayleigh number* (the ratio of heat transfer due to conduction and convection), and b is a geometric parameter. Furthermore, x is proportional to convective motion, y is proportional to the temperature difference between ascending and descending currents and z is proportional to the distortion of the vertical temperature profile [Sparrow, 1982]. Lorenz studied the system with these specific values for the parameters, and found non-periodic solutions. The equations are solved in time and a classical phase portrait (along with planar projections) of the solution shows the celebrated *Lorenz attractor* in Figure 2.1. Note that the crossing-over of the trajectory is an artifact of projecting the attractor in two dimensions, which does not physically happen as the attractor exists in a higher spatial dimension.

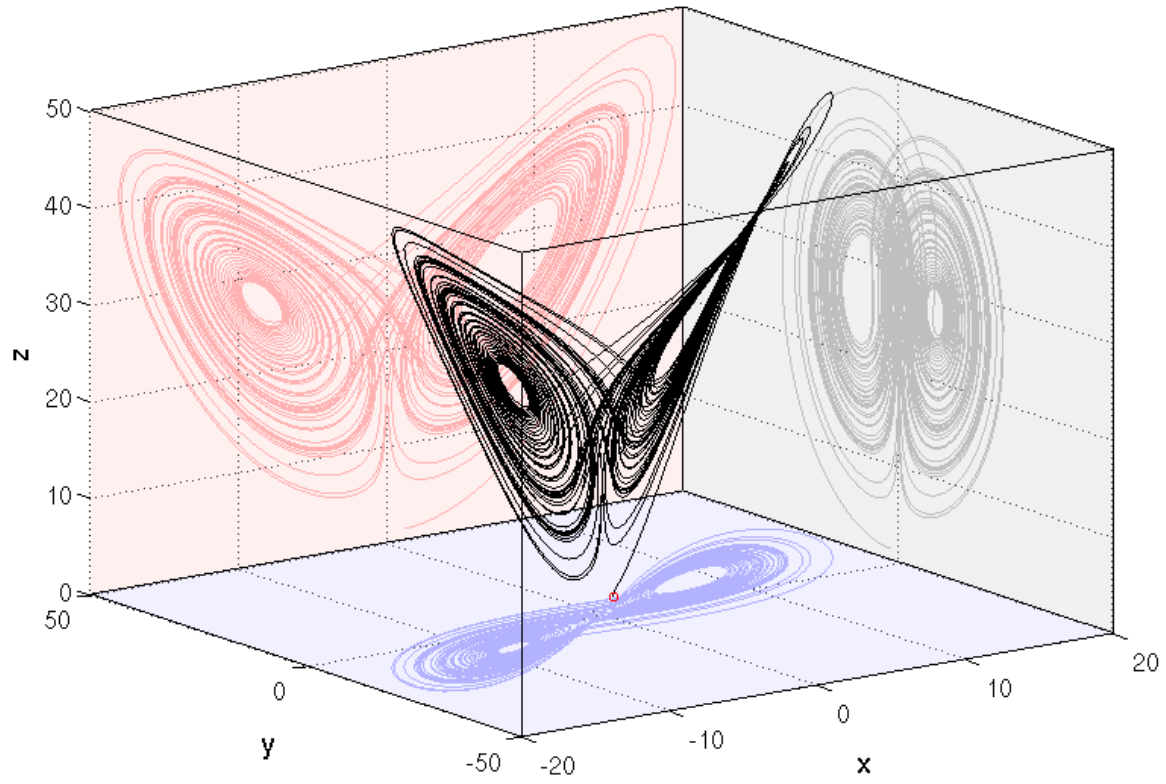

Figure 2.1: A solution to the Lorenz equations integrated in time (with arbitrary initial conditions marked in *red*) is visualized in phase-space along with projections on the XY, YZ and XZ planes. The trajectory lies on an *attractor* which now goes by the name of the *Lorenz Butterfly*.

2.1.2 The Lorenz Attractor

As in the Lorenz model, the trajectories for most chaotic systems are bounded by a complex geometrical object in the phase-space called a *strange attractor*, which is characterized by a *fractal dimension*. Lorenz [1963] called this an *infinite complex of surfaces*. Fractals are self similar objects, often associated with a non-integer spatial (or embedding) dimension, which makes them extremely convoluted and complex, and have been increasingly found in the physical world and phase-spaces describing dynamical processes alike [Mandelbrot, 1983]. This dimension of the Lorenz attractor is found to be approximately 2.06. The Lorenz system is also a dissipative one, which implies that finite initial volumes are contracted to zero, through their evolution in the phase-space. Some properties of the attractor are now evaluated through the evolution of trajectories, which give an overview of the dynamics of the system.

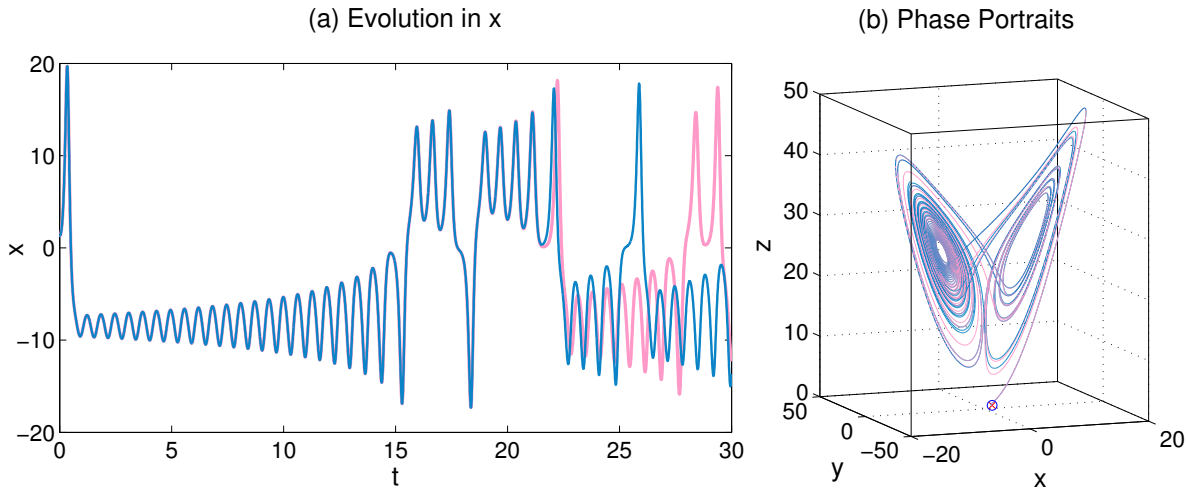

Figure 2.2: Two identical trajectories with slightly different initial conditions ($\sim 10^{-4}$) are seen to rapidly diverge, although they evolve on the same attractor (seen on the right).

Signs of Chaos

"Now here, now there, now down, now up, it drives them."
$\sim$ Dante Alighieri[1]

Chaotic systems are marked by their extreme sensitivity to initial conditions. The dynamics of a set of initial conditions often involves repeated *stretching* and *folding* in phase-space, which causes points that are nearby to diverge and vice-versa, in an almost unpredictable manner. This is demonstrated by initiating a pair of identical trajectories, of which one is slightly perturbed. This is done by integrating the first solution from arbitrary initial conditions $\{x_0, y_0, z_0\}$, and the other from $\{x_0 + \epsilon, y_0 + \epsilon, z_0 + \epsilon\}$, where ϵ is a random perturbation of the order $\sim 10^{-4}$. The initial phase of their evolution is shown in Figure 2.2. On the left panel, the trajectories (along x) are seen to evolve in a similar fashion for a short duration, after which they diverge and evolve independently. The panel on the right shows that although the trajectories are soon uncorrelated, they lie on the same attractor which binds them in the phase-space.

2.1.3 Average Error Growth

Exponential error propagation characterizes a chaotic system, which is now investigated for the Lorenz model. Looking again at Figure 2.2, the difference between the two trajectories (the Euclidean norm) $\delta(t)$ is calculated as follows

$$\delta(t) = \sqrt{(x_1(t) - x_2(t))^2 + (y_1(t) - y_2(t))^2 + (z_1(t) - z_2(t))^2} \tag{2.2}$$

This value represents the error at time t. It is essential to realize that such comparisons of diverging trajectories are affected by the choice of initial conditions to a small extent, whereas the governing rate of error propagation is universal to the system. To eliminate these local

[1] *"Di qua, di là, di giù, di sù li mena"* in the original [as appears in Mandelbaum et al., 1980]. These words seem to bear timeless relevance in describing the dynamics of chaotic systems, as the trajectories are driven hither and tither around the phase-space. Two trajectories, bounded by the attractor and hence close-by in space, are never to meet again, quite like the lamenting souls stuck in the eternal whirlwind of Dante's Inferno.

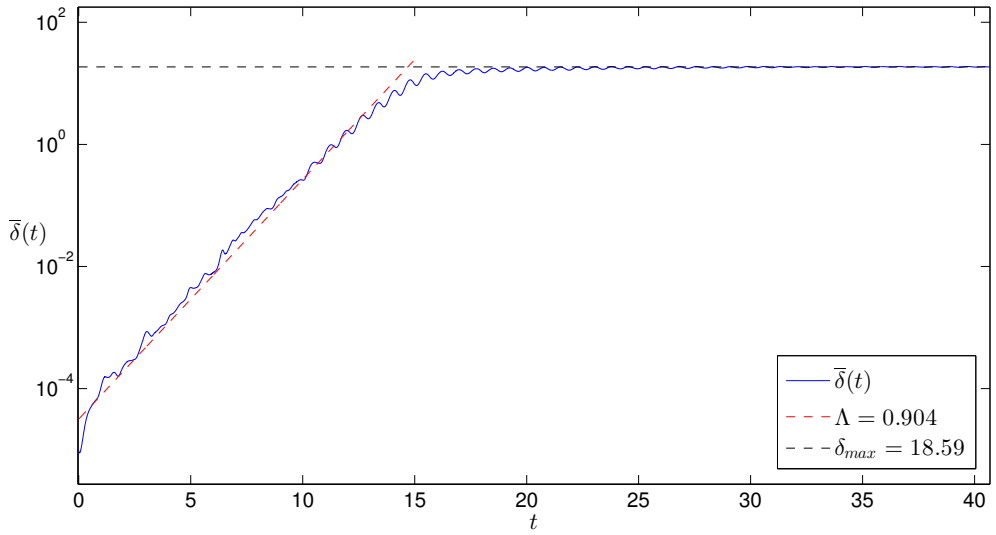

Figure 2.3: Error growth in the Lorenz Model shown as an average over $10,000$ realizations. The average error grows exponentially with a constant slope, which is known as the Lyapunov exponent of the system and saturates at a maximum value, owing the the boundedness of the attractor.

variability effects and to give the general nature of error growth in this system, it is estimated for $10,000$ ensemble pairs starting from uncorrelated points spread over the attractor. The average error evolution in these runs gives an unbiased estimate of its growth in the model, and is calculated as

$$\bar{\delta}(t) = \sum_{n=1}^{N} \frac{\delta_n(t)}{N} \tag{2.3}$$

Figure 2.3 shows this growth (the blue curve), the slope of which is found from the best exponential fit (the broken line in red). This value is known as the *effective* **Lyapunov Exponent** Λ of the system and is found to be 0.904, which can be used to express the growth of error in the exponential regime in the form

$$\delta = \delta_0 e^{\Lambda t} \tag{2.4}$$

where δ_0 is the initial error and t is the evolution time. This relation later helps state the bounds on t, when we wish to limit the growth of error to within specific values. Chaotic systems are marked by individual Lyapunov exponents along each degree of freedom. A negative exponent causes trajectories to contract towards the attractor, whereas a positive exponent causes divergence along the attractor. The effective Lyapunov exponent is always between the smallest and largest Lyapunov exponents.

2.1.4 Sensitivity of the Attractor

The attractor exhibits different sensitivity at different locations. It can be interpreted as locally acting Lyapunov exponents. Such variability effects the convergence/divergence of trajectories locally, impacting predictions as shall be seen in the study of ensemble based predictions in Section 2.8.2. This is demonstrated by initiating a pair of runs from several points spread over the attractor, which are left to evolve until their initial separation δ_0 is amplified by a factor α.

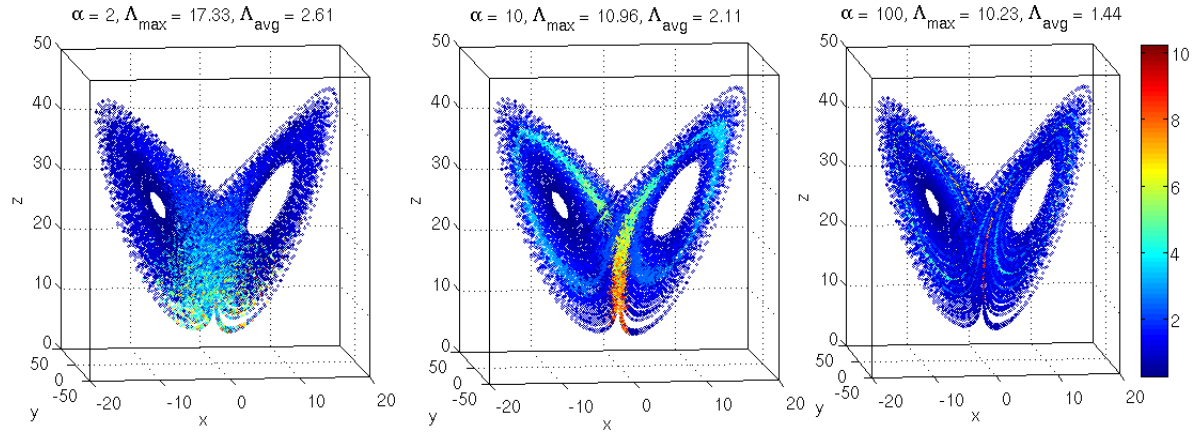

Figure 2.4: Attractor sensitivity is shown as the locally acting Lyapunov exponent, calculated from the time taken for a fixed amplification of an initial separation between two trajectories. It is seen that on a short timescale, a very large positive Lyapunov exponent can act on the system.

The formula for error growth from Equation 2.4 now becomes

$$\begin{aligned} \alpha\,\delta_0 &= \delta_0\, e^{\Lambda_l T} \\ \Lambda_l &= \frac{\log(\alpha)}{T} \end{aligned} \tag{2.5}$$

where the time taken (T) for an amplification of α varies for each point depending on its location on the attractor, reflecting the locally acting Lyapunov exponent (Λ_l). This reflects the sensitivity of the different zones on the attractor, marking those where a large positive Λ_l can rapidly amplify the error. These are calculated and shown for several values of α in Figure 2.4. The first figure on the left ($\alpha = 2$) shows that the initial doubling of an error can have Λ_l as large as 17.83 and can occur within a short time of 0.04 units. For $\alpha = 10$ there is a fine band that exists towards the middle of the wings where a large Λ_l can act. For larger α values (~ 100 and more), the average Λ_l is seen to converge to the effective Lyapunov exponent of the system. The largest local Lyapunov exponent can still be as high as 10.3, increasing the initial error a hundred-fold in a short time of 0.46 units. This is specially observed on the lower part of the attractor where trajectories can split to either of its two wings.

A plume of 1000 initial conditions starting within a distance of 0.001 from each other is now allowed to evolve over a long duration, and their initial phase is shown in Figure 2.5. The data from their time series is used to study some statistical features of the three variables.

2.1.5 Probability Distribution of the Triad

The PDFs of the variables is shown in Figure 2.6 (with the solid black curve showing the ensemble averaged PDF). Although the trajectories are seen to diverge quite rapidly, the probability distribution of x, y and z has a very similar shape for each, and is invariant of the choice of initial conditions, alluding to the fact that they are all bound by the same attractor. The trajectories are seen to *visit* and linger more on the left wing and the lower half of the attractor, as can be interpreted from the slight skewness of the PDFs, which is further seen in the intensity constructed by projecting the PDFs to the horizontal axis, and the color range marks the probability. Next, the power spectrum of the three variables is studied.

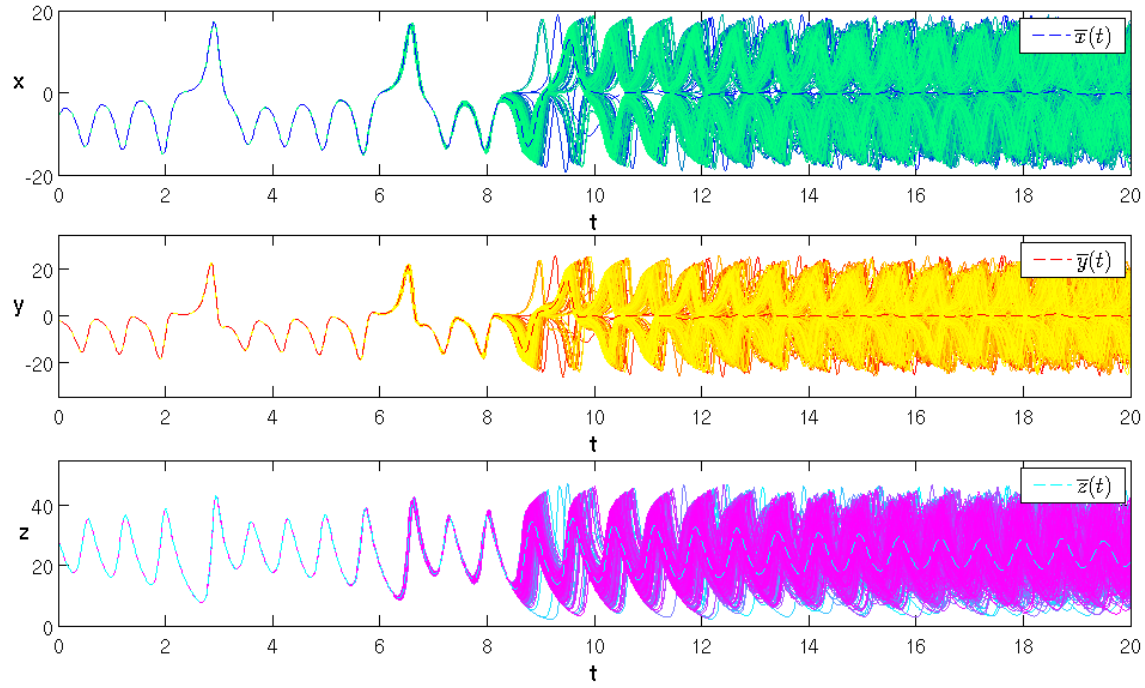

Figure 2.5: The initial evolution of a plume of 1000 trajectories within a distance of 10^{-3} is shown. The 'x' and 'y' evolution shows how the initially close-by trajectories split to either wings of the attractor around $t = 8.5$, and eventually become uncorrelated around $t = 14$.

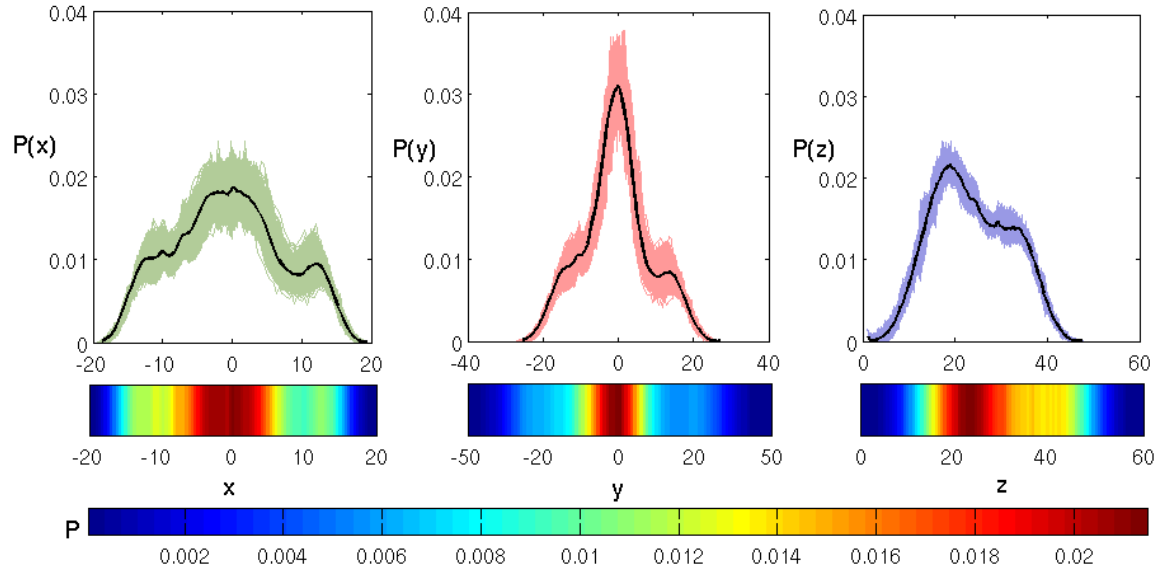

Figure 2.6: The probability distribution of x, y and z, which is seen to be invariant of the choice of initial conditions after a long enough evolution of the system. Intensity maps are made by projecting the PDF to the horizontal axis, which show some *preferred* or recurring zones visited by trajectories.

2.2 Power Spectrum Analysis

A Discrete Fourier Transform (DFT) is used to transform a time series (or data points in space) to its frequency (or wavenumber) domain to study the distribution of energy in the different scales of the system. The transform is given as

$$\hat{\mathcal{F}}_k = \sum_{n=0}^{N-1} f_n e^{-2\pi i n k/N} \tag{2.6}$$

where $\hat{F}_k$ gives the the contribution of the dimensionless wavenumber k to the function f [Oppenheim et al., 1989]. Here k represents the frequency with respect to the total duration of the signal (or the number of oscillations over the domain length). The energy in the original function f (for instance a temperature field) can be related to the Fourier transform with Parseval's theorem as follows

$$\sum_{n=0}^{N-1} |f_n|^2 = \frac{1}{N} \sum_{k=0}^{N-1} |\hat{\mathcal{F}}_k|^2 \tag{2.7}$$

The power spectrum, is therefore simply given as

$$E(k) = |\hat{\mathcal{F}}(k)|^2 = \hat{\mathcal{F}}(k)\hat{\mathcal{F}}^\star(k) \tag{2.8}$$

where the asterisk denotes the complex conjugate, and $E(k)$ gives the contribution of each wavenumber to the total energy contained in the field, which can lastly be calculated by integrating the power over all wavenumbers

$$E_{\text{tot}} = \sum_{k=1}^{\infty} E(k) \tag{2.9}$$

2.2.1 Power Spectra of the Time Series

Studying the time series of the three variables in the frequency domain provides insight into the distribution of the energy contained in the signal over different frequencies of motion. Such an analysis reveals the timescales which contain the maximum energy, and are known to correlate well with the timescales containing the maximum error energy as well. This timescale dominates the growth of error and is a crucial yardstick for predictability. An averaged power spectrum of the three variables is presented in Figure 2.7. The spectrum is seen to peak at a frequency of around 0.8, which corresponds to a timescale of $t \sim 1.25$ units. This shows that the fluctuations over a time of around 1.25 contain the maximum energy in the system. The energy rapidly falls off with smaller timescales (higher frequencies) showing that smaller fluctuations contain less energy. Figure A.1 in the appendix shows the evolution of trajectories from random points on the attractor for several T values, where it becomes clear that over a time of $T \sim 1.25$ a trajectory goes around one wing of the attractor.

The process of forecasting is now simulated in the Lorenz model by developing a framework for data assimilation, and several techniques are applied and compared in the following sections.

2.3 Data Assimilation Preliminaries

The climate system has been extensively studied and has well established governing equations that describe its dynamics. An analytic solution to these, however, has been impossible to find,

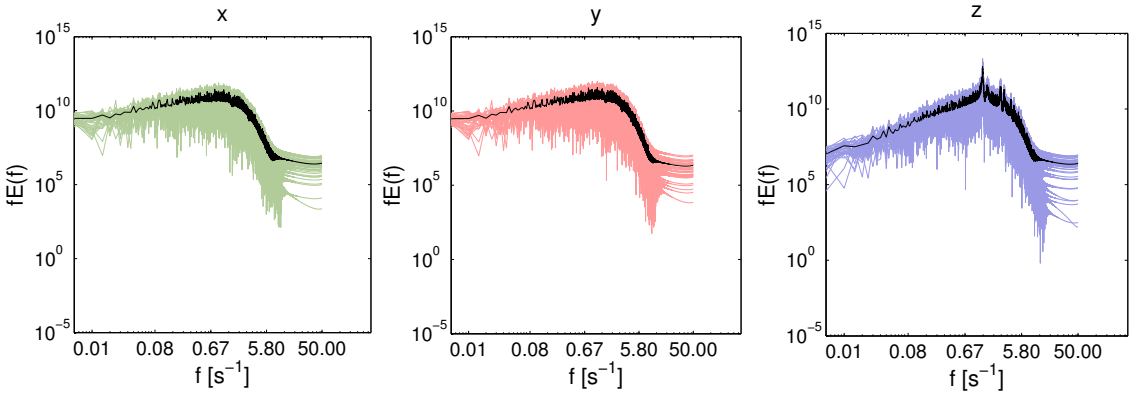

Figure 2.7: The power spectrum of the x, y and z variables shows a peak corresponding to a frequency of about ~ 0.8, which corresponds to a timescale of $T \sim 1.25$. This is approximately the time it takes for a trajectory to go around one wing of the attractor, and contains the maximum energy which makes it a relevant timescale for forecasting.

isolating numerics as the only viable approach to solving them. This is done by treating the system as an initial value problem, where using some information of the physical state of the atmospheric variables through measurements serving as initial conditions, the governing equations are solved in time to predict future states. Although, since these measurements are not completely error free, the smallest uncertainties in their values rapidly magnify to soon give disparate predictions from the real physical state that is later observed. Using observations alone for predictions, hence, has a limited scope. This gave rise to techniques of Data Assimilation which statistically combine observations along with model predictions to form a better performing set of initial conditions. Before some of these methods are studied, a framework is described for simulating forecasts in the Lorenz Model (which is generally applicable to other dynamical systems as well), beginning with the generation of observations from a control run.

2.3.1 Generating Observations from a Control Run

First a *true solution* (or the control run) is set up, which represents the state of the atmosphere and is simply a solution to the equations integrated from arbitrary initial conditions for a chosen duration. Practically, this simulates the evolution of *unknown* physical variables encountered in the atmosphere like temperature, pressure etc, that are measured by observations. To that effect, the total evolution time of the true solution is divided into 'N' *measurement intervals* of duration T each, which are the instances where an 'observation' is generated by using the 'true state' at each interval and adding a normalized random perturbation of the order of ϵ, which is the fixed 'observational error' margin. In real forecasting, this error arises from error of the measurement instrument, or from atmospheric noise. This gives us observations at each interval as follows

$$\vec{x}_{\mathrm{o}} = \vec{x}_{\mathrm{t}} + \vec{\epsilon} \tag{2.10}$$

where $\vec{x}_{\mathrm{t}}$ is the true solution vector, $\vec{\epsilon}$ is a random vector (ϵ_x, ϵ_y,ϵ_z) that lies within specified bounds of the observational error.

2.3.2 Determining the 'Analysis'

For forecasting (or predicting a future state), the model is initiated with the observation at the zeroth interval t_0, and the system is solved in time upto the first measurement interval t_1. The

value now obtained is the 'forecast', and is called the *model value* $\vec{x}_{\rm m}$ (as it is the value predicted by the model). Now, an analysis is performed, to estimate the initial conditions for the next interval, and is termed as $\vec{x}_{\rm a}$. It is calculated using the model forecast and the observation at that point, such that

$$\vec{x}_{\rm a}(t_n) = \vec{x}_{\rm m}(t_n) + w\left(\vec{x}_{\rm o}(t_n) - \vec{x}_{\rm m}(t_n)\right) \tag{2.11}$$

where t_n is the interval number with $n \in \{1..N\}$. The new parameter w is the *weight* which makes $\vec{x}_{\rm a}$ a specific combination of $\vec{x}_{\rm m}$ and $\vec{x}_{\rm o}$. Simply put, using w as a scalar value lying between 0 and 1, the analysis can be one of the following

$$\begin{aligned} w = 0 &\rightarrow \vec{x}_{\rm a} = \vec{x}_{\rm m} && \text{(Free running model)} \\ w = 1 &\rightarrow \vec{x}_{\rm a} = \vec{x}_{\rm o} && \text{(Model initiated with Observations)} \\ 0 < w < 1 &\rightarrow \vec{x}_{\rm a} = \vec{x}_{\rm m} + {\rm w}(\vec{x}_{\rm o} - \vec{x}_{\rm m}) && \text{(Model initiated between } \vec{x}_{\rm m} \text{ and } \vec{x}_{\rm o}) \end{aligned} \tag{2.12}$$

Figure 2.8 shows a schematic of how these steps work. The control run or the true solution is

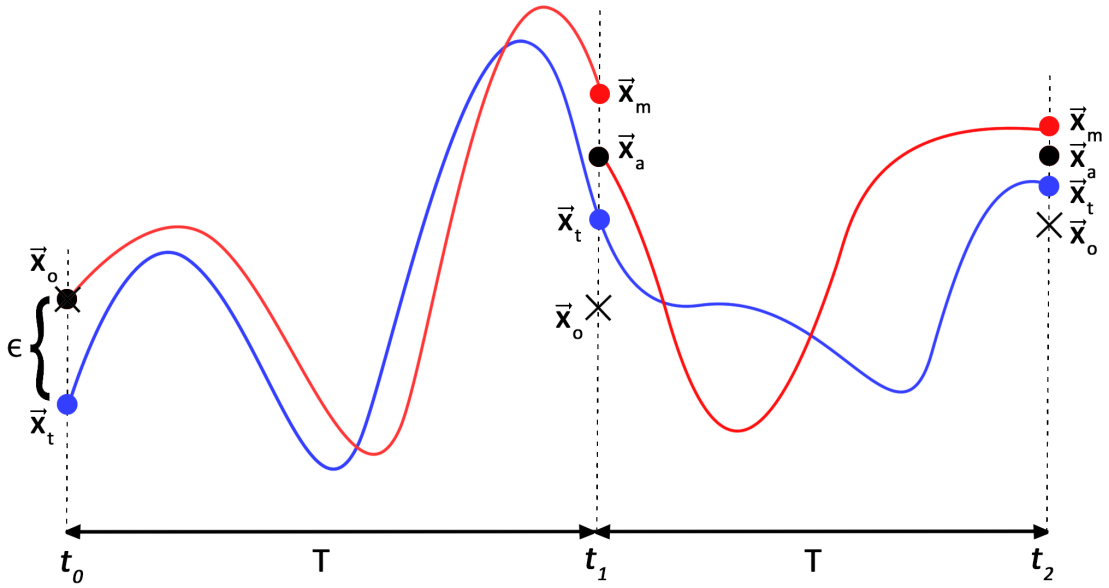

Figure 2.8: A schematic showing the steps involved in the process of Data Assimilation. The blue curve represents the *true* state, divided into 2 intervals of length T. The cross marks at t_0, t_1 and t_2 are the observations within an error range ϵ. Further, $\vec{x}_{\rm m}$ is the model prediction (the red curve) and $\vec{x}_{\rm a}$ is the analysis value at each interval, which serves as initial conditions for forecasting.

shown as the blue curve evolving in time along the horizontal axis, divided into two measurement intervals of length T. The black cross at t_0 marks the first observation (within an error range of ϵ) with which the model is initiated. At the first interval, t_1, the model prediction is given as $\vec{x}_{\rm m}$, and another observation is made. Using these two pieces of information at t_1, and Eq. 2.11, an analysis value $\vec{x}_{\rm a}$ is determined, which is used as the initial condition for the next interval upto t_2.

This method is repeated, generating the prediction of the model after each interval, governed by w and ϵ. This is a simple representation of how the analysis can be performed, and can be generalized by allowing w to vary based on the variances in the different variables, which is studied later. The performance of the model is now estimated by defining a term for the relative error growth.

2.3.3 A Measure for Relative Error

To gauge the quality of model forecasts, a quantity is defined based upon the error of prediction at each measurement interval. First, the error δ at every interval t_n is calculated as the vectorial distance between the true state and the model forecast

$$\delta(t_n) = \sqrt{\big(x_{\mathrm{m}}(t_n) - x_{\mathrm{t}}(t_n)\big)^2 + \big(y_{\mathrm{m}}(t_n) - y_{\mathrm{t}}(t_n)\big)^2 + \big(z_{\mathrm{m}}(t_n) - z_{\mathrm{t}}(t_n)\big)^2} \tag{2.13}$$

where $x_{\mathrm{m}}(t_n)$ is the model prediction and $x_{\mathrm{t}}(t_n)$ is the true state at interval t_n. These values are then averaged over the entire simulation as follows

$$\langle\delta\rangle = \exp\left\{\sum_{n=1}^{N}\left(\frac{1}{N}\log\delta(t_n)\right)\right\} \tag{2.14}$$

Lastly, the *relative error* E is defined as

$$E = \frac{\langle\delta\rangle}{\epsilon} \tag{2.15}$$

where normalizing $\langle\delta\rangle$ with ϵ gives the relative growth of error independent of the observational error. This measure was developed specially for this study. Several other definitions representing the model performance were also tested, including a root mean square error. They were discarded because they showed high sensitivity to parameters like the initial perturbation ϵ_0 and the number of measurement intervals, and were seen to be often dominated by single extreme values (specially for the RMS Error) and did not clearly reflect the performance of the model. As shown further, a definition based upon the logarithmic error is quite robust and quantifies the model performance more closely, independent of the choice of initial error, converging well with a sufficiently large number of measurement intervals.

The smaller the value of E, the lesser the model diverges from the control run, reflecting a better overall prediction. This value is only dependent on the choice of the weight w which determines the model contribution to each $\vec{x}_{\mathrm{a}}$, and the measurement interval duration T, which determines the time allowed for the growth of model error, before it is nudged to the analysis value at the next interval. This growth can be estimated by Eq. 2.4, and holds until the error diverges to its maximum value (ref Figure 2.3) after which the error erratically oscillates around the maximum. The relative error values presented hereafter are taken as the average over several realizations in each case.

2.4 Analysis Using Fixed Weights

Forecasting is now done for the Lorenz Model by using fixed scalar weights for the analysis ($w \in [0, 1]$). This enables the system to have a fixed fraction of model and observation contributions in the initialization of forecasting. To test this method, the relative error is plotted as a function of weight for a measurement interval length of $T = 0.25$ in Figure 2.9.

Clearly, a large E is seen corresponding to $w = 0$, which represents a free running model that constantly diverges, and is a meaningless regime. As the observations start weighing in, there is a steep drop at a critical w around 0.2, and the error reduces around 4 orders of magnitude. The part of the curve after this point is relevant and is separately shown in the plot inlay. Here, the error is small, as the model contribution begins to assist observations. Forecasting using observations alone (marked as a blue circle at $w = 1$), yields a small relative

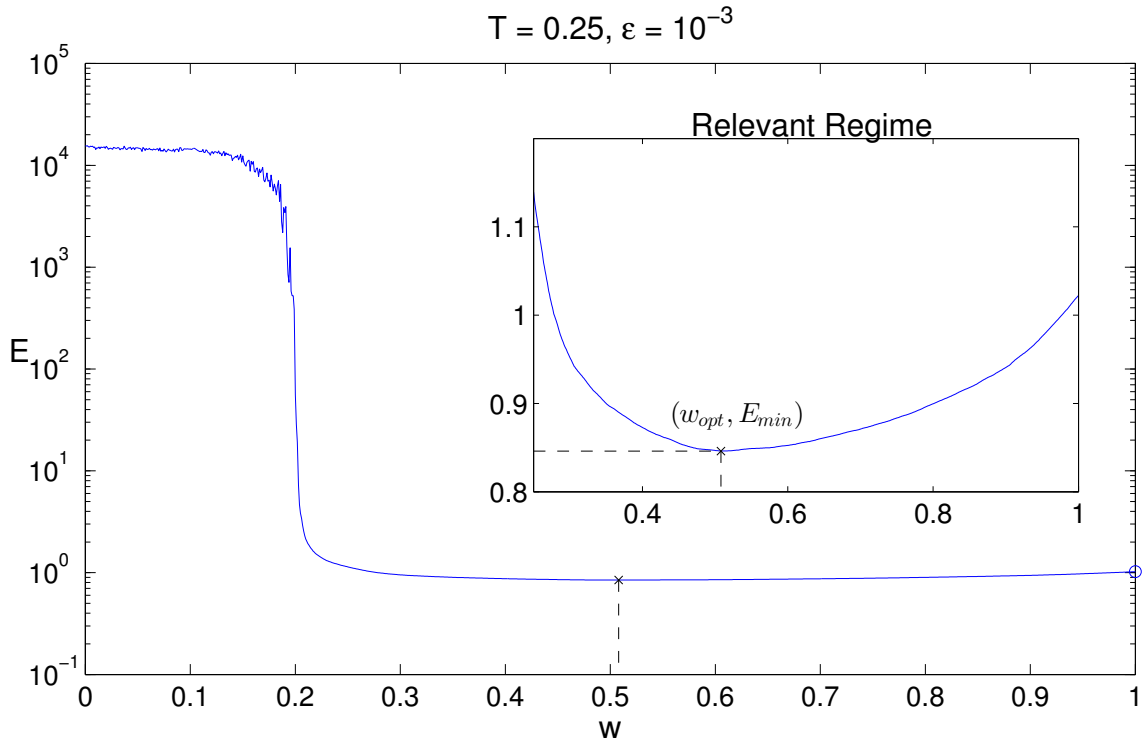

Figure 2.9: Relative error E plotted against the scalar weight w. The inlay shows that using a fixed fraction of the model contribution performs *better* than using a purely observation based forecast (which corresponds to $w = 1$), marking the existence of an optimal weight $w_{\mathbf{opt}}$ for a given T.

error. However, it is interesting to observe that there is a weight less than 1 which yields the *minimum* error, performing better than solely observation based forecast (shown as the cross mark, also projected to the x-axis marking what is called an *optimal weight* w_{opt}). The error dips to the optimum weight, and then increases upto $w = 1$. This directly indicates the utility of having even a *fixed* model contribution in initializing forecasts.

To verify whether the definition of E (ref Eq. 2.15) is independent of the choice of ϵ, it is studied for several cases of ϵ marking the optimal weight in Figure 2.10. It is seen that the minimum error (marked by the 'x') does not change for varying ϵ values. Furthermore, at $w = 1$, the error is the same for all the cases which emerges from Eq. 2.4 reducing to $\delta = e^{\Lambda T}$ due to the normalization by ϵ, and is only dependent on the choice of T (and can be analytically found to be 1.2536 for $T = 0.25$ and $\Lambda = 0.904$). For $w = 0$, or the free running model, the error grows to its maximum (around 18.59 as seen in Figure 2.3), and upon normalizing with ϵ gives a larger value for a smaller ϵ (marked by circles on the vertical axis for each case).

After verifying these properties of the measure E, forecasting is now done for varying T values, imposing that the measurement interval should never be so long as for the error to grow to its maximum value within a single interval. Since ϵ is fixed as 0.001, according to Eq. 2.4, this limits the measurement interval to be sufficiently smaller than 10.87. The relative error is plotted as a function of w for different T values (taken as ensemble averages over several realizations) in Figure 2.11, and the corresponding optimal weights are marked. The value of the integration time step dt was limited to at least two orders of magnitude lower than T, forecasting for 10^4 measurement intervals for each case. The weight is incremented in a step size of 10^{-3}.

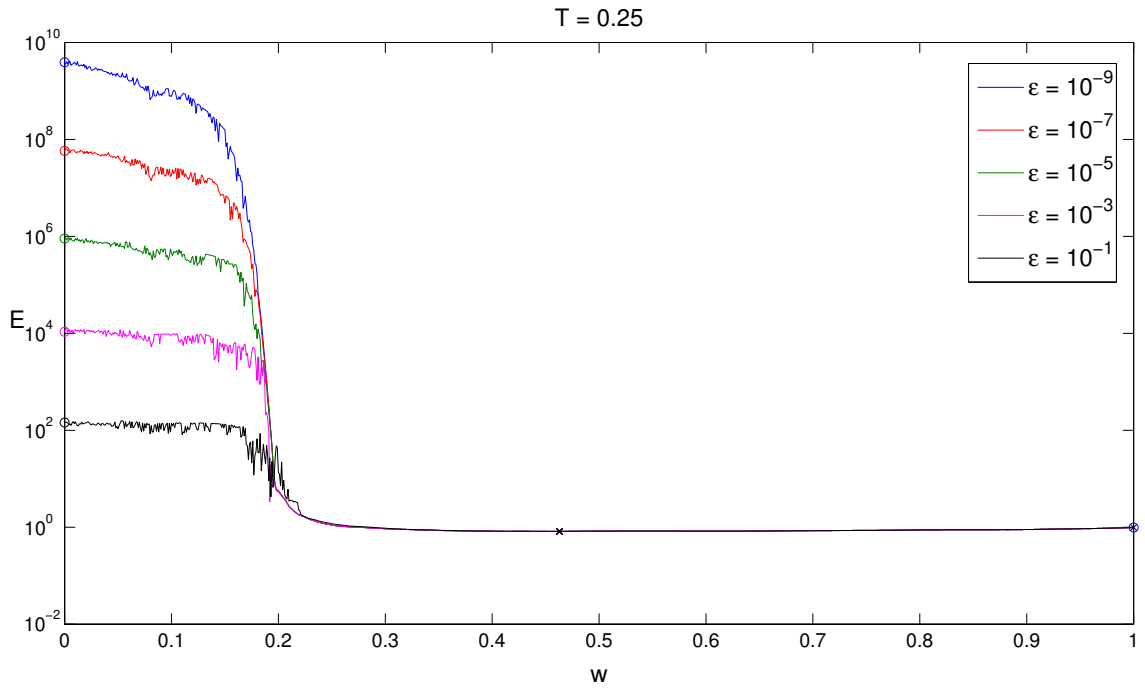

Figure 2.10: E **VS** w **plot for different** ϵ **values shows that the minimum relative error does not vary with the choice of** ϵ**, yielding the same** $w_{\mathbf{opt}}$**.**

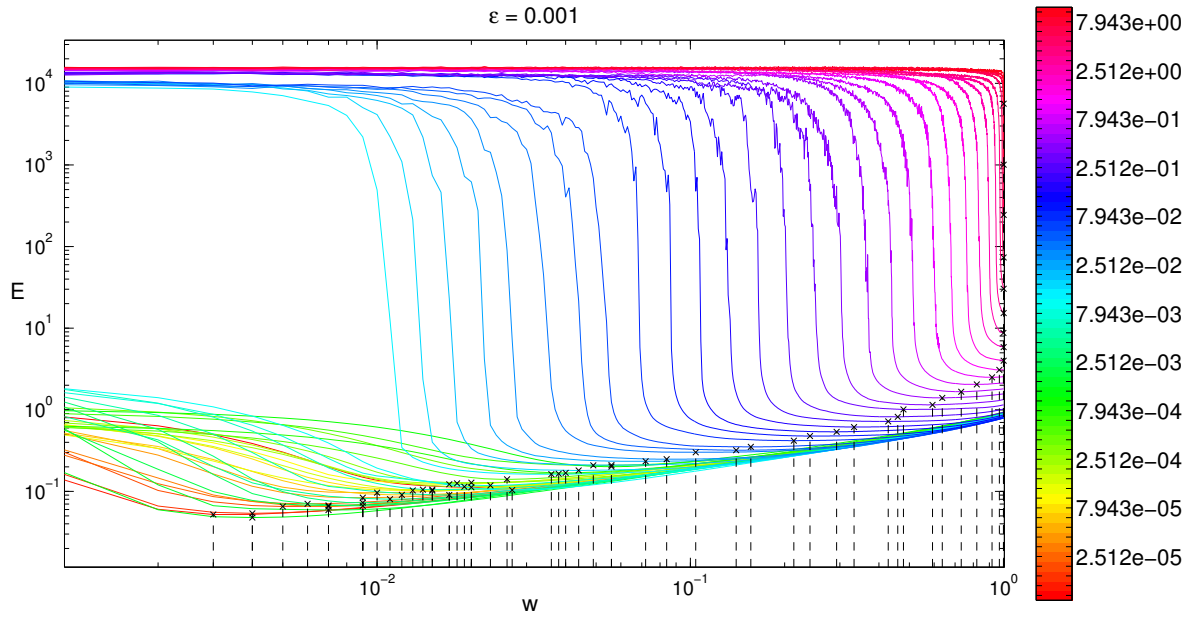

Figure 2.11: E **as a function of** w**, for different** T **values showing the shift in the minimum relative error. The cross marks show this value for each case of** T **and the corresponding optimal weight projected on the** x **axis.**

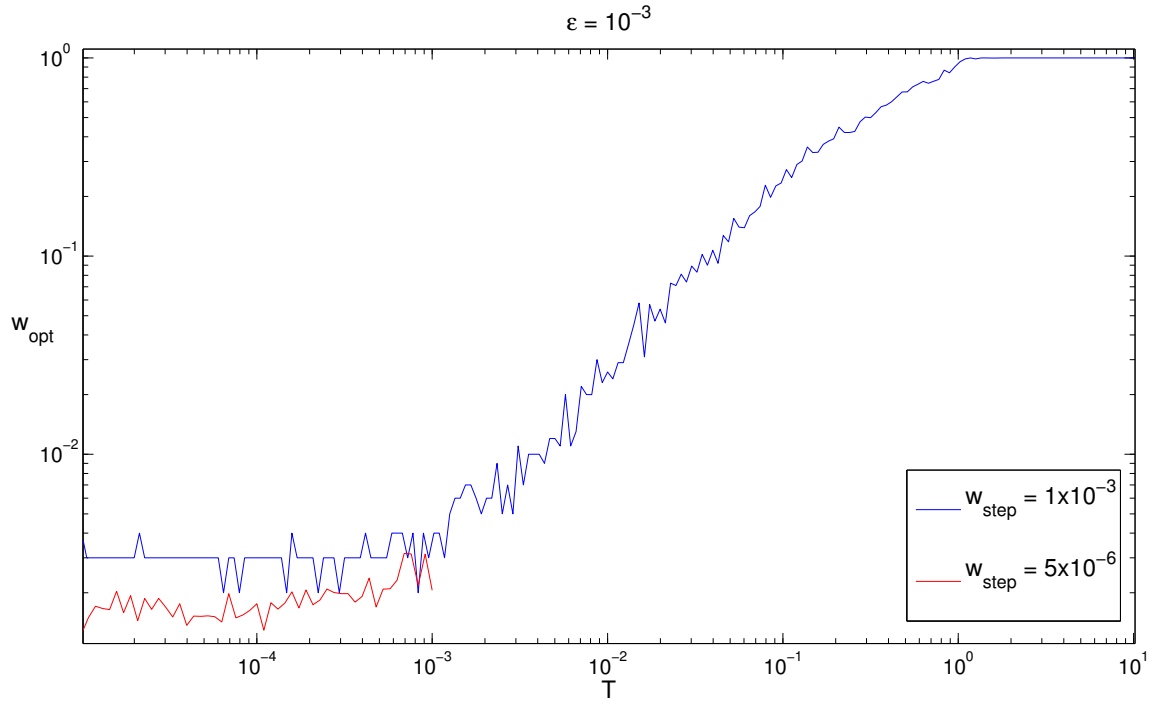

Figure 2.12: The increasing value of w_{opt} for a larger T is shown. The weight w needs to be incremented in smaller step sizes for very small T values to find optimal weights close to zero.

The first thing to note in the figure is that the curve shifts more to the right as T is increased. This is such that for very small values of T, the minimum relative error is found at an optimal weight of *almost* zero. This means, the observations are always further off than the model prediction, compared to the true solution, and the analysis suggests using a large contribution from the model prediction at each measurement as the new initial condition. It still weights in a small contribution of the observations, because at exactly $w = 0$ we would have a free running model which shall constantly diverge. Whereas for large values of T, the minimum relative error corresponds to a weight equal to one. This is a case where the error always grows beyond the ϵ neighborhood of the 'true solution', and the plot suggests using the 'observation' value at each measurement instance as the next initial condition (completely disregarding the model prediction).

The optimal weights can now be extracted from this plot, by taking the w value corresponding to the minimum E, which gives the dependence of w_{opt} on the choice of T and is shown in Figure 2.12, as the blue curve. The values of w_{opt} for the range of $T \sim 10^{-5} - 10^{-3}$ shows numerical artifacts because of the step size of w, making 0.001 the smallest value that can be assumed apart from 0 (which cannot be an optimal weight itself, as it represents a free running model). This is verified by performing a small set of runs over $T \sim 10^{-5} - 10^{-3}$, now varying w in steps of 5×10^{-6}, and the corresponding optimal weights are shown by the red curve. This no longer shows a 'flattening' effect seen for larger step sizes of w, and the optimal weight further reduces for smaller T values.

It is interesting to see that data assimilation already improves forecasts, based upon this simple study.

2.5 Analyis Using a Method of 'Cheating'

To form a reference case along with the fixed weights in assessing the quality of predictions using more advanced methods, a method of *cheating* for performing the analysis is proposed. Here, at each measurement point, a comparison is made between the error in model forecast (δ_m) and the observation (δ_o), using the true solution. First, the vectorial distances are calculated as

$$\delta_m(t_n) = \sqrt{(x_m(t_n) - x_t(t_n))^2 + (y_m(t_n) - y_t(t_n))^2 + (z_m(t_n) - z_t(t_n))^2}$$
$$\delta_o(t_n) = \sqrt{(x_o(t_n) - x_t(t_n))^2 + (y_o(t_n) - y_t(t_n))^2 + (z_o(t_n) - z_t(t_n))^2}$$

Now, if $\delta_m < \delta_o$ at a given measurement instance, the model forecast is used as the initial conditions for the next interval, (i.e. $\vec{x}_{\mathrm{a}} = \vec{x}_{\mathrm{m}}$), otherwise the observation alone is used ($\vec{x}_{\mathrm{a}} = \vec{x}_{\mathrm{o}}$). This method of 'cheating' is so called because it uses information of the *true state*, or the background variable, which is not practically available.

This method is initiated using the observation at t_0 (like the previous case of varying weights), which then 'cheats' at every measurement instance to closely follow the true solution. The algorithm should intuitively be always closer to the true state of the system, yielding a smaller relative error as opposed to a weighted case. This hypothesis is tested by comparing the relative error from the cheating case, and the previous case using optimal weights by defining an error reduction term.

2.6 Error Reduction

The simplest method of forecasting is using observation values alone at each measurement as the initial conditions for the forecast. The relative error for such a case can be found from Figure 2.11, corresponding to $w = 1$ (which effectively reduces Eq. 2.11 to $\vec{x}_{\mathrm{a}} = \vec{x}_o$). These values are referred to as 'E_{Obs}', the E values corresponding to the optimal weights as 'E_{wopt}' and those from the cheating case as '$\mathrm{E_{ch}}$'. Since using either optimal weight or cheating should reduce the error , an 'Error Reduction' term R is introduced for both cases as follows

$$R_{\mathrm{wopt}} = \left(\frac{E_{\mathrm{Obs}}}{E_{\mathrm{wopt}}}\right)$$
$$R_{\mathrm{ch}} = \left(\frac{E_{\mathrm{Obs}}}{E_{\mathrm{ch}}}\right) \tag{2.16}$$

This measure helps compare the performance of both the cases, and is plotted over varying T values in Fig 2.13. It is interesting to see that the cheating case does not necessarily perform better than using an optimal weight instead, and below a certain T value, optimal weights perform better than cheating. For very small values of T, using observations alone performs rather badly. This follows from the fact that an initial condition reaches the attractor through an evolution following the dynamics of the system. When T is so small that the point does not end up on the attractor by the next interval, using another observation again places it further off than the attractor. T in the range of $0.1 - 2.5$ shows a better prediction using the cheating algorithm than using optimal weights, which is the range of the maximum energy containing timescales as was seen in Figure 2.7 and shall be the focus for improving predictions.

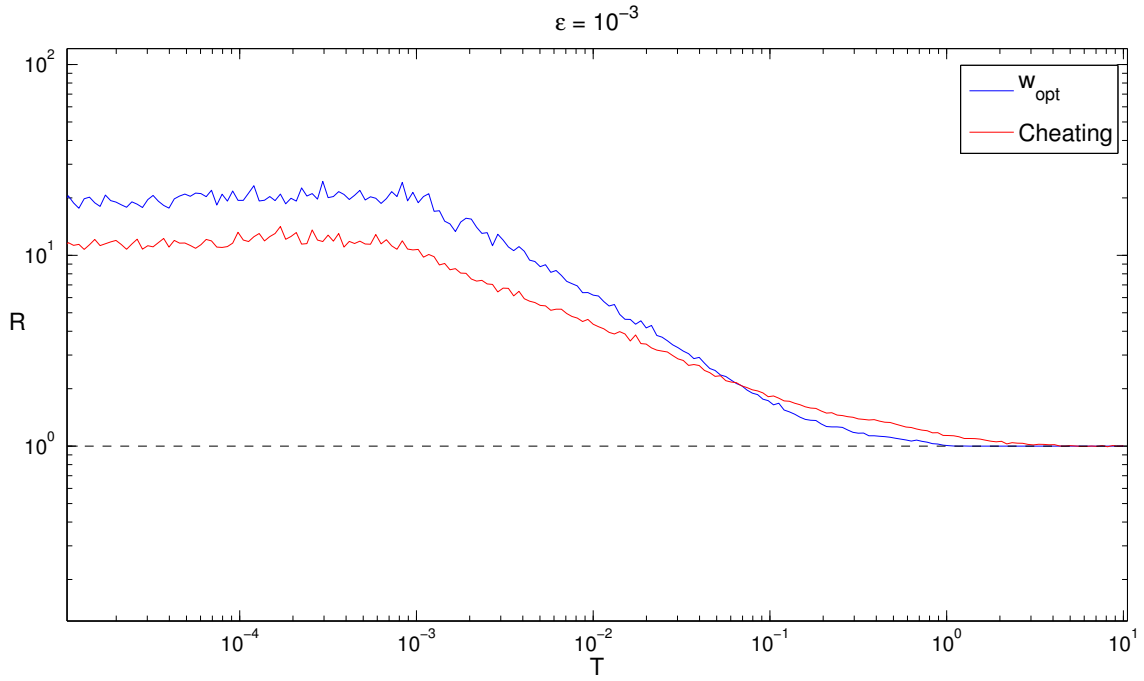

Figure 2.13: The reduction in error (R) upon using the optimal weights as opposed to the cheating cases is shown. The method of cheating outperforms optimal weights in the energy containing timescales of $T = 0.1 - 2.5$.

2.7 Adaptive Methods for Statistical Estimation

The method of using fixed scalar weights for the analysis is a simple model and serves a dual purpose - first, it clearly demonstrates the utility of DA in reducing forecasting error, and second, it can be used as a reference to compare advanced DA methods that shall now be studied. These methods are closer to the techniques in practice, finding their genesis in statistical methods to estimate the 'true' state of variables which shall now be described.

2.7.1 Least Squares Method for two Observations

A common method used to determine the 'true state' of a quantity (say ϕ_t), given two observations ϕ_1 and ϕ_2 where:

$$\begin{aligned} \phi_1 &= \phi_t + \epsilon_1 \\ \phi_2 &= \phi_t + \epsilon_2 \end{aligned} \tag{2.17}$$

is to minimize the combined variance. Here ϵ_1, ϵ_2 denote the unknown errors. Usually, a good estimate of the error margin ϵ is known, which helps in a better approximation of the background state ϕ_t. These errors are unbiased such that the mean $\langle \epsilon_i \rangle = 0$, and the variance is given as $\left\langle \epsilon_i^2 \right\rangle = \sigma_i^2$. The best estimate for ϕ_t based on ϕ_1 and ϕ_2 is a weighted sum which accounts for the individual variances from the mean, and is termed as the *analysis* value ϕ_a:

$$\phi_a = w_1\phi_1 + w_2\phi_2 \tag{2.18}$$

Taking the average (expected value) one gets

$$\langle \phi_a \rangle = (w_1 + w_2)\phi_t$$

as $\langle \phi_i \rangle = \phi_t$, we get $w_1 + w_2 = 1$. The variance σ_a^2 is now calculated using the independence $\langle \epsilon_1 \epsilon_2 \rangle = \langle \epsilon_1 \rangle \langle \epsilon_2 \rangle$

$$\begin{aligned} \left\langle (\phi_a - \phi_t)^2 \right\rangle &= \left\langle (w_1 \epsilon_1 + w_2 \epsilon_2)^2 \right\rangle \\ &= w_1^2 \langle \epsilon_1^2 \rangle + 2 w_1 w_2 \langle \epsilon_1 \rangle \langle \epsilon_2 \rangle + w_2^2 \langle \epsilon_2^2 \rangle \qquad (2.19) \\ \sigma_a^2 &= w_1^2 \sigma_1^2 + (1 - w_1)^2 \sigma_2^2 \qquad (2.20) \end{aligned}$$

The best estimate of ϕ_t is given by the value of w_1 that minimizes σ_a^2, and is found by calculating the minima as

$$\begin{aligned} \frac{d\sigma_a^2}{dw_1} = 2 w_1 \sigma_1^2 - 2(1 - w_1)\sigma_2^2 = 0 \qquad (2.21) \\ w_1(\sigma_1^2 + \sigma_2^2) = \sigma_2^2 \qquad (2.22) \\ w_1 = \frac{\sigma_1^{-2}}{(\sigma_1^{-2} + \sigma_2^{-2})}, w_2 = \frac{\sigma_2^{-2}}{(\sigma_1^{-2} + \sigma_2^{-2})} \qquad (2.23) \end{aligned}$$

This gives us the following expressions for ϕ_a and w

$$\begin{aligned} \phi_a = \frac{\sigma_1^{-2}}{(\sigma_1^{-2} + \sigma_2^{-2})} \phi_1 + \frac{\sigma_2^{-2}}{(\sigma_1^{-2} + \sigma_2^{-2})} \phi_2 \qquad (2.24) \\ \sigma_a^2 = \frac{1}{(\sigma_1^{-2} + \sigma_2^{-2})} \qquad (2.25) \end{aligned}$$

If $\sigma_2 \gg \sigma_1$ then $\phi_a \to \phi_1$ and $\sigma_a^2 \to \sigma_1^2$, disregarding any contribution from the second measurement as it has a very large variance and is more uncertain. This method can be generalized for two independent pieces of information about the system, which can also be a combination of observations and model predictions.

2.7.2 Prediction using Model and Observations

A model let to run 'free' can be written as

$$\phi_m^n = M \left\{ \phi_m^{n-1} \right\} \qquad (2.26)$$

where the value of a quantity ϕ at time n depends on its state at the previous step $(n-1)$, acted upon by the operator M. Now, if an observation ϕ_o^n is made at time t_n, the model can be initiated with an analysis value ϕ_a^n

$$\phi_m^{n+1} = M \{ \phi_a^n \} \qquad (2.27)$$

Where the analysis at t_n, in case of observations only, is

$$\phi_a^n = \phi_o^n \qquad (2.28)$$

Since the observations are not error free, an unbiased error of order ϵ_o should be accounted for, as well as an ϵ_m for the model forecast, then by using Eq. 2.23, this new framework of combining model and observations becomes

$$\phi_a^n = \frac{\sigma_o^{-2}}{\left(\sigma_o^{-2} + \sigma_m^{-2}\right)} \phi_o^n + \frac{\sigma_m^{-2}}{\left(\sigma_o^{-2} + \sigma_m^{-2}\right)} \phi_m^n \qquad (2.29)$$

with $\sigma_m^2 = \langle \epsilon_m^2 \rangle$ and $\sigma_o^2 = \langle \epsilon_o^2 \rangle$.

The unknown term here is the model error $\langle \epsilon_m^2 \rangle$, which is difficult to quantify. It stems from errors in the employed equations, parameter errors, and most importantly, those in the initial conditions which amplify during the evolution of the system. Hence, this term is always dependent on the immediate state of the system in phase-space, and needs to be resolved in a manner accounting for local variability.

The method used in Section 2.3.2 of using fixed weights is seen to reduce the relative error, although it does not account for local variability in the system and is hence non-adaptive. A method of using ensembles for prediction is now described, which overcomes this shortcoming.

2.8 Ensemble Based Forecasting

Using ensembles provides a measure to gauge the sensitivity of the system at different locations through the evolution in phase-space. For instance, there are small regions where a highly positive local Lyapunov exponent acts on the system, making parallel trajectories diverge rapidly, greatly reducing the quality of model prediction. There are also other regions where a very small or negative Λ_l can cause convergence of trajectories, which are locations where the model predicts well. An ensemble seed is used to assess these states, represented in the model variance in the following manner.

2.8.1 Ensemble Seed

To recall, we initiated the model using the observations as follows

$$\vec{x}_a(t_0) = \vec{x}_{\mathrm{o}}(t_0)$$

Now, an ensemble seed of N_e ensembles is initiated as

$$\vec{x}_e^i(t_0) = \vec{x}_{\mathrm{a}}(t_0) + \vec{\delta}_i \tag{2.30}$$

where $i \in \{1..N_e\}$ and $\vec{\delta}_i$ is a random perturbation of a specified magnitude. This forms a set of initial conditions in the neighborhood to $\vec{x}_{\mathrm{o}}$ that are solved along with the model $\vec{x}_{\mathrm{m}}$, and at the next measurement interval, the model variance is estimated.

2.8.2 Analysis Using Scalar Ensemble Spreads

To calculate the ensemble spread, first, the ensemble mean is calculated at the interval t_n as

$$\langle \vec{x}_e(t_n) \rangle = \sum_{i=1}^{N_e} \frac{\vec{x}_e^i(t_n)}{N_e} \tag{2.31}$$

Using the ensemble mean, the ensemble spread S_e is calculated as the average distance of all trajectories from the mean, which is a measure of σ_m at the instance t_n

$$S_e(t_n) = \sqrt{\frac{1}{N_e} \sum_{i=1}^{N_e} \left(x_e^i(t_n) - \langle \vec{x}_e(t_n) \rangle \right)^2 + \left(y_e^i(t_n) - \langle \vec{y}_e(t_n) \rangle \right)^2 + \left(z_e^i(t_n) - \langle \vec{z}_e(t_n) \rangle \right)^2} \tag{2.32}$$

This value of S_e is dependent on the choice of δ, such that it will be large for large values of δ (also emerging directly from Eq. 2.4). This makes the current definition of S_e a property of the

ensemble itself, and not solely representative of the system, hence it is normalized with δ and ϵ to represent σ_m as

$$\sigma_m(t_n) \propto S_e(t_n)\frac{\epsilon}{\delta}$$
$$\sigma_m(t_n) = \alpha S_e(t_n)\frac{\epsilon}{\delta} \tag{2.33}$$

where α is some constant. This is one way to estimate σ_m which is unknown, and can be assumed to be proportional to the ensemble spreads in some way. To that effect, first simulations are done with $\alpha = 1$, and then α is changed slightly to see how the behavior changes. The analysis is now performed as described by Eq. 2.24, taking σ_m^2 as the model variance and $\sigma_o^2 = \epsilon^2$ as the error variance

$$\vec{x}_\mathrm{a} = \vec{x}_\mathrm{m} + \frac{\sigma_m^2}{(\sigma_m^2 + \sigma_o^2)}(\vec{x}_\mathrm{o} - \vec{x}_\mathrm{m})$$
$$\vec{x}_\mathrm{a} = \vec{x}_\mathrm{m} + w_\mathrm{ens}(\vec{x}_\mathrm{o} - \vec{x}_\mathrm{m}) \tag{2.34}$$

Now in places where the model is highly sensitive, the spread is larger and $\sigma_m^2 \gg \sigma_o^2$, which gives $w_\mathrm{ens} = 1$, using the observation as the analysis, and where $\sigma_m^2 \ll \sigma_o^2$, $w_\mathrm{ens} = 0$, hence using the model value for the analysis. This method is conceptually able to work like the 'cheating' case, without using the true state as reference. It also adapts w_ens according to the local sensitivity of the model.

The relative error E is calculated for different T values using this method, and a new error reduction comparison is shown in Figure 2.14. The method is seen to closely approximate the 'cheating' case for a reasonable range of $T = 10^{-1} - 10^{1}$, but for smaller T values, does not perform better than the previous methods. This might be so because for very small interval times, the highly sensitive locations on the attractor can suddenly magnify the ensemble spread, and consequently σ_m, such that the w_ens increases, as opposed to the fixed weights case where a small w is consistently used throughout.

To see the effect of T on the ensemble spreads, and subsequently w_ens, the PDF of w_{ens} is plotted in Figure 2.15. The range of w_ens values being assumed increases from $T = 0.01$ to $T = 0.1$, although the average value w_avg remains almost the same. As T increases to 10, the value of w_ens is always 1, which is what is expected as well, since the spread invariably increases to around the maximum bound by Eq. 2.4 for $T = 10$. The method is seen to adapt well to local variability of them model, improving the quality of predictions.

Further, in Figure 2.16 the distribution of w_ens on the attractor for different T values is seen which reflects how the method of ensembles adapts to local variability. For $T = 0.01$, the lower portion of the attractor is generally assigned with a larger w_ens. To recall, the first panel of Figure 2.4 that showed the local Lyapunov exponents for an amplification factor of 2 showed similar zones to be more sensitive. The average Lyapunov exponent for $\alpha = 2$ was seen to be 2.61, which gives an average value of $T = 0.26$, which is near to 0.1. As T increases, a weight close to 1 is seen to occupy most of the phase-space, as the ensembles diverge to a larger extent, consequently increasing the model error variance.

A comparison can now be performed between the w_opt for different T values, and the w_ens obtained from the ensemble spread based forecasts, using Eq. 2.34, which is shown in Figure 2.17. The ensemble spread method is seen to have a larger w value on average for smaller interval times, and levels off to 1 at $T > 5$. This might be the reason why the ensembles do not perform as well as the optimal weights in the small T regime, as the method uses a larger w value, hence using a larger contribution of the observations during analysis.

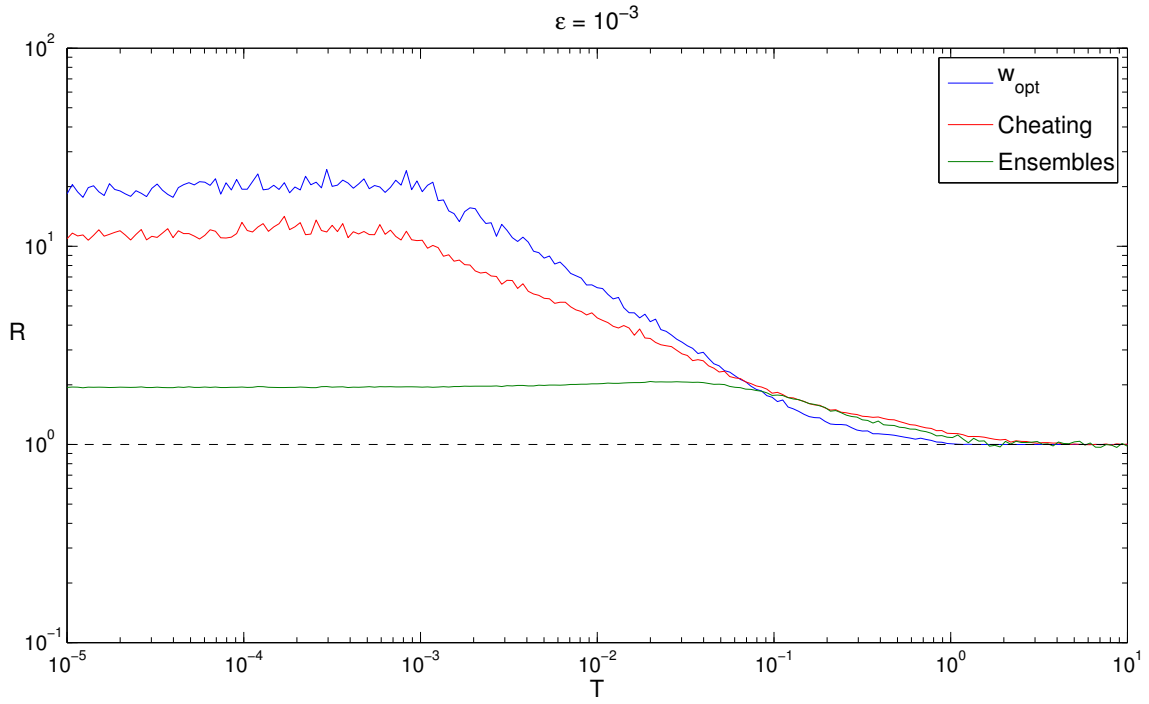

Figure 2.14: Error reduction for the method of ensemble spreads shows the method performs as good as the cheating case between $T = 0.1 - 10$, although not performing very well in the lower T range, where the method uses a larger contribution of the model for analysis than the fixed optimal weights.

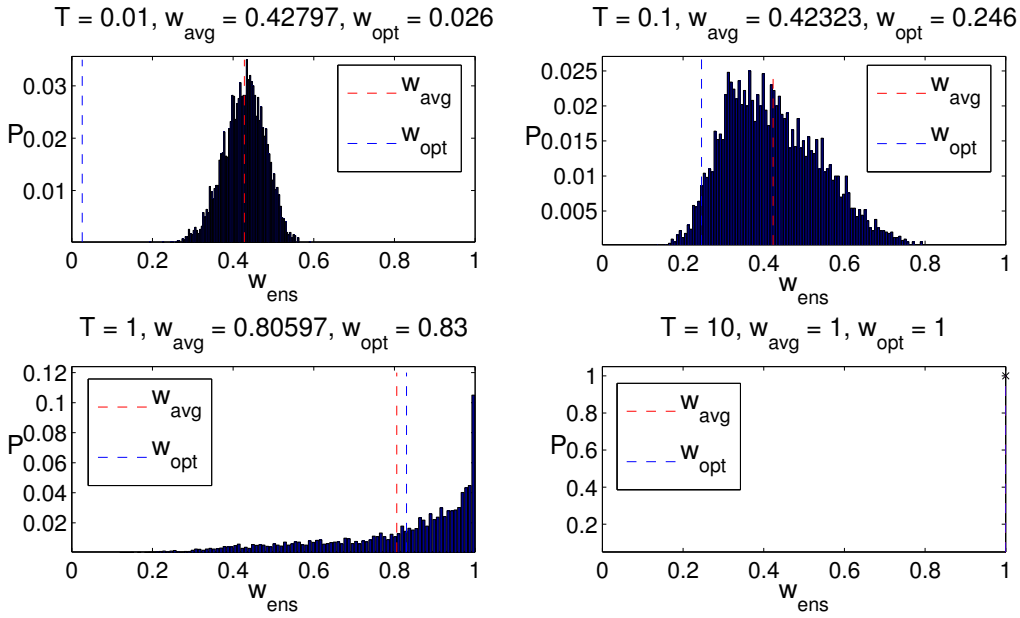

Figure 2.15: PDFs of w_{ens} for T varying over three orders of magnitude are shown. The ensemble forecasting is seen to adapt well to local variability assigning different weights, which is seen to shift more towards 1 as T goes to 10.

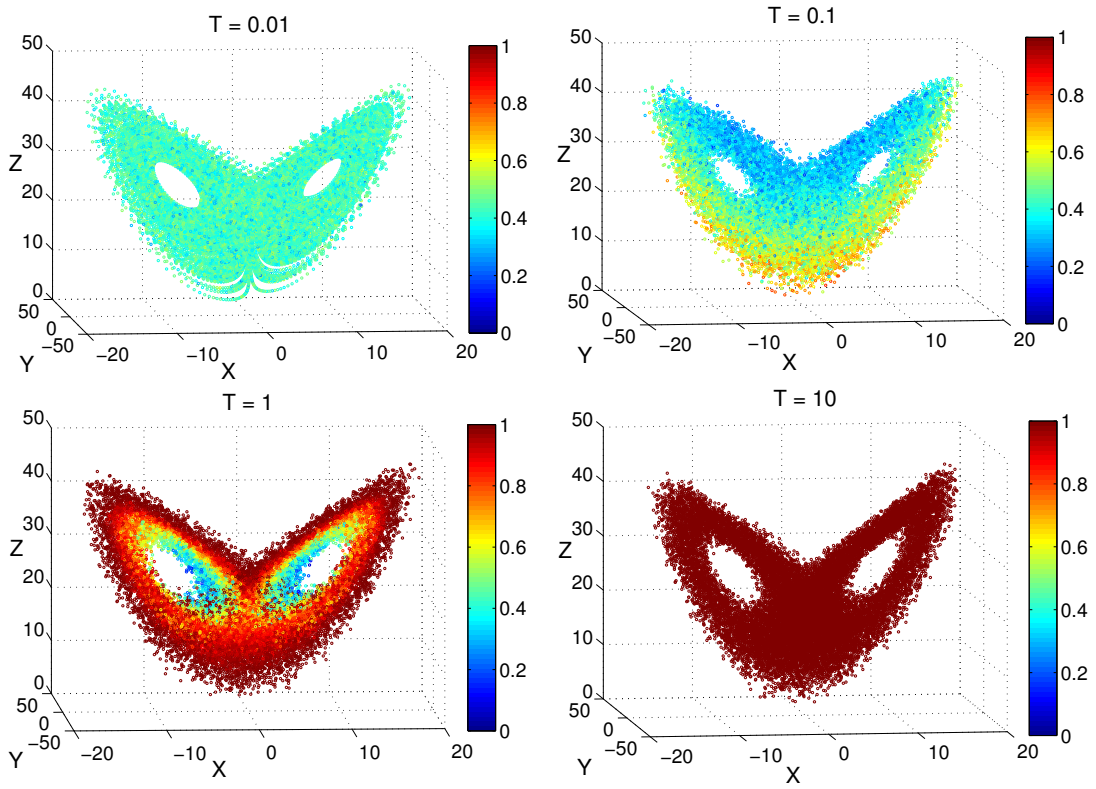

Figure 2.16: Distribution of $w_{\mathbf{ens}}$ through the phase-space of the attractor shows a close correspondence in the sensitive zones as seen in Figure 2.4. As T increases to 10, the model variance increases as well, consequently $w_{\mathbf{ens}}$ is seen to reach 1 over a large part of the attractor.

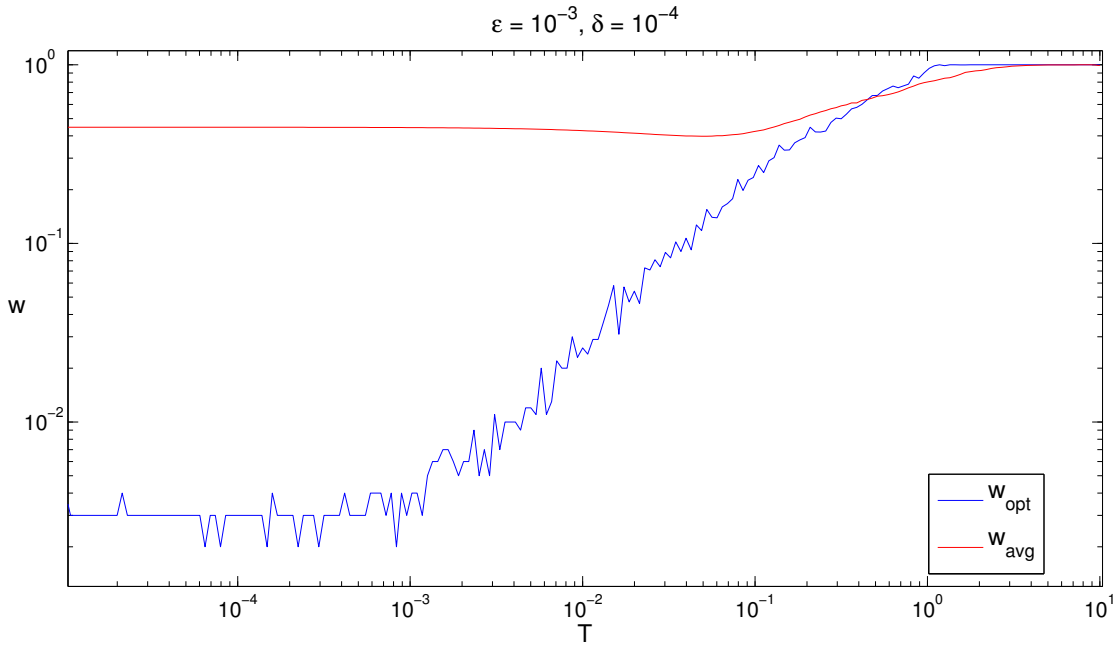

Figure 2.17: Comparison between $w_{\mathbf{opt}}$ and $w_{\mathbf{avg}}$ for different T values is shown. For smaller values of T, where the ensemble based forecast does not perform as well as optimal weights, it is seen that $w_{\mathbf{avg}}$ is much larger that $w_{\mathbf{opt}}$, i.e. the method uses more model contribution than it should.

Lastly, as α in Eq. 2.33 is not known, it is varied to see the change in the behavior of R. Since the dependence on α is quadratic, it is kept to within some limits, so it does not dominate the calculation of w_{ens}. Figure 2.18 shows that normalizing σ_m with $\frac{\epsilon}{\delta}$ and $\alpha = 1$ performs the best for the widest range of T values (the green curve stays closest to the 'cheating' case which is the red curve). Using $\alpha > 2$ or $\alpha < 0.5$ caused the predictions to perform very badly.

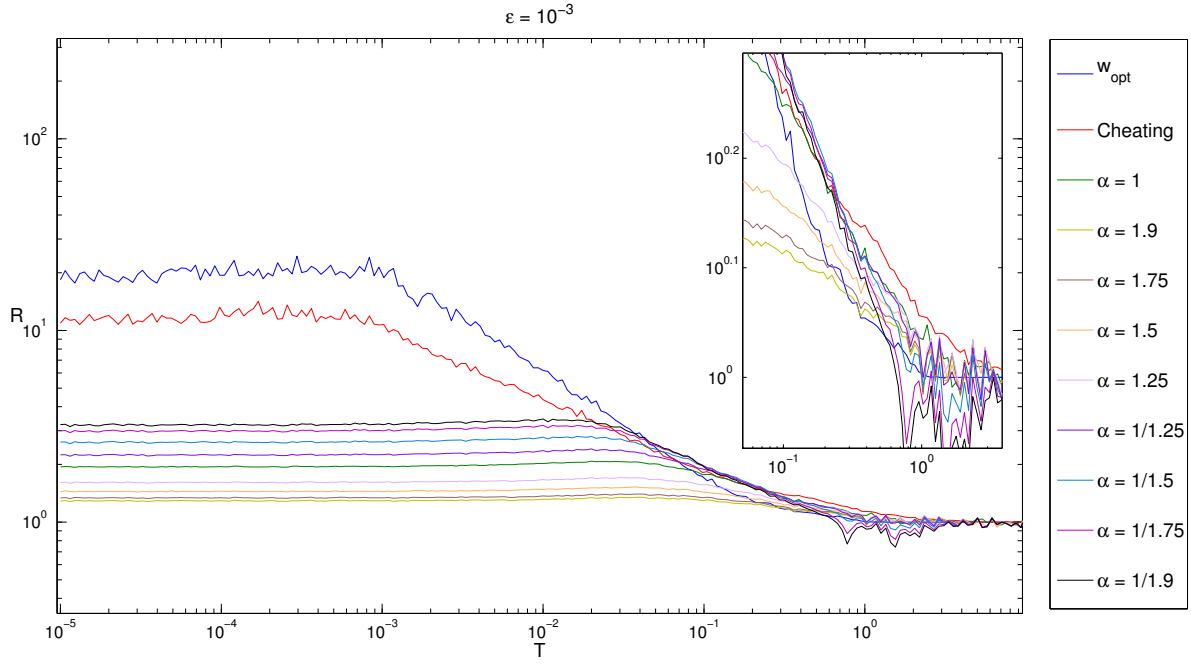

Figure 2.18: Error Reduction upon varying α values shows that $\alpha = 1$ is a suitable choice during the normalization of σ_m (ref Eq. 2.33).

2.8.3 Multivariate Best Estimate

The previous section described a method based upon a single representative variance for the model. However, a better measure of model variance in multivariate systems is to represent the variances and covariances in each variable individually. This expands the single σ_m used earlier to a 3×3 matrix (M) that accounts for the variances in x, y and z and the 3 covariances between each pair of variables. In general, the analysis for a N-dimensional vector ϕ becomes

$$\vec{\phi}_{\text{a}} = \vec{\phi}_{\text{m}} + W(\vec{\phi}_{\text{o}} - \vec{\phi}_{\text{m}}) \tag{2.35}$$

where W is a $N \times N$ matrix. M and O are the model and observations error covariance matrices taken as

$$\begin{aligned} M &= \langle \vec{\epsilon}_{\text{m}} \vec{\epsilon}_{\text{m}}^{\top} \rangle \\ O &= \langle \vec{\epsilon}_{\text{o}} \vec{\epsilon}_{\text{o}}^{\top} \rangle \end{aligned} \tag{2.36}$$

As described earlier, an optimal value of W is found by minimizing the error in the analysis equation, the details of which can be found in Kalnay [2003]. This W matrix is found to be

$$W = M[O + M]^{-1} \tag{2.37}$$

which makes the analysis

$$\vec{\phi}_{\rm a} = \vec{\phi}_{\rm m} + M[O+M]^{-1}[\vec{\phi}_{\rm o} - \vec{\phi}_{\rm m}] \tag{2.38}$$

Let us now review the M and O matrices.

Model Error Covariance Matrix

M is a symmetric 3×3 matrix that contains information about the 9 components of the variance in the 3 dimensional model and is given as:

$$M = \begin{bmatrix} \sigma_{xx}^2 & \sigma_{xy}^2 & \sigma_{xz}^2 \\ \sigma_{yx}^2 & \sigma_{yy}^2 & \sigma_{yz}^2 \\ \sigma_{zx}^2 & \sigma_{zy}^2 & \sigma_{zz}^2 \end{bmatrix}$$

The diagonal terms σ_{xx}^2, σ_{yy}^2 and σ_{zz}^2 represent the model variance in each of the three variables x, y and z. They are calculated similar to Eq. 2.32, although now individually as:

$$\begin{aligned}
\sigma_{xx} &= \alpha\frac{\epsilon}{\delta}\sqrt{\frac{1}{N_e}\sum_{i=1}^{N_e}\left(x_e^i(t_n) - \left\langle\vec{x}_e(t_n)\right\rangle\right)^2} \\
\sigma_{yy} &= \alpha\frac{\epsilon}{\delta}\sqrt{\frac{1}{N_e}\sum_{i=1}^{N_e}\left(y_e^i(t_n) - \left\langle\vec{y}_e(t_n)\right\rangle\right)^2} \\
\sigma_{zz} &= \alpha\frac{\epsilon}{\delta}\sqrt{\frac{1}{N_e}\sum_{i=1}^{N_e}\left(z_e^i(t_n) - \left\langle\vec{z}_e(t_n)\right\rangle\right)^2}
\end{aligned} \tag{2.39}$$

The off diagonal terms give the covariances between the three variables and are given as:

$$\begin{aligned}
\sigma_{xy} = \sigma_{yx} &= \alpha\frac{\epsilon}{\delta}\sqrt{\frac{1}{N_e}\sum_{i=1}^{N_e}\left(x_e^i(t_n) - \left\langle\vec{x}_e(t_n)\right\rangle\right)\left(y_e^i(t_n) - \left\langle\vec{y}_e(t_n)\right\rangle\right)} \\
\sigma_{xz} = \sigma_{zx} &= \alpha\frac{\epsilon}{\delta}\sqrt{\frac{1}{N_e}\sum_{i=1}^{N_e}\left(x_e^i(t_n) - \left\langle\vec{x}_e(t_n)\right\rangle\right)\left(z_e^i(t_n) - \left\langle\vec{z}_e(t_n)\right\rangle\right)} \\
\sigma_{yz} = \sigma_{zy} &= \alpha\frac{\epsilon}{\delta}\sqrt{\frac{1}{N_e}\sum_{i=1}^{N_e}\left(y_e^i(t_n) - \left\langle\vec{y}_e(t_n)\right\rangle\right)\left(z_e^i(t_n) - \left\langle\vec{z}_e(t_n)\right\rangle\right)}
\end{aligned} \tag{2.40}$$

where N_e is the number of ensembles. The normalization with $\frac{\epsilon}{\delta}$ is done as earlier, along with the factor α.

Observational Error Covariance Matrix

It is a matrix similar to M, and contains information about the error variances in the observation and is given as:

$$O = \begin{bmatrix} \epsilon_{xx}^2 & \epsilon_{xy}^2 & \epsilon_{xz}^2 \\ \epsilon_{yx}^2 & \epsilon_{yy}^2 & \epsilon_{yz}^2 \\ \epsilon_{zx}^2 & \epsilon_{zy}^2 & \epsilon_{zz}^2 \end{bmatrix}$$

The diagonal terms are given as

$$\epsilon_{xx}^2 = \epsilon_{yy}^2 = \epsilon_{zz}^2 = \epsilon^2 \tag{2.41}$$

where ϵ is the observation error. All the off diagonal terms in this matrix are zero because each observation error has been taken as a random perturbation, and hence their covariance is zero. The O matrix reduces to:

$$O = \begin{bmatrix} \epsilon_{xx}^2 & 0 & 0 \\ 0 & \epsilon_{yy}^2 & 0 \\ 0 & 0 & \epsilon_{zz}^2 \end{bmatrix}$$

The analysis as described by Eq. 2.35 can be expanded as follows

$$x_a = x_m + W_{xx}(x_o - x_m) + W_{xy}(y_o - y_m) + W_{xz}(z_o - z_m) \tag{2.42}$$

and similarly for y and z, where W_{xx} etc. are corresponding terms from the W matrix calculated from Eq. 2.37.

It can be immediately seen that as opposed to the previous methods, the analysis for each individual variable now also accounts for the influence of its covariance with the other variables. The error reduction for the multivariate best estimate method is now shown in Figure 2.19.

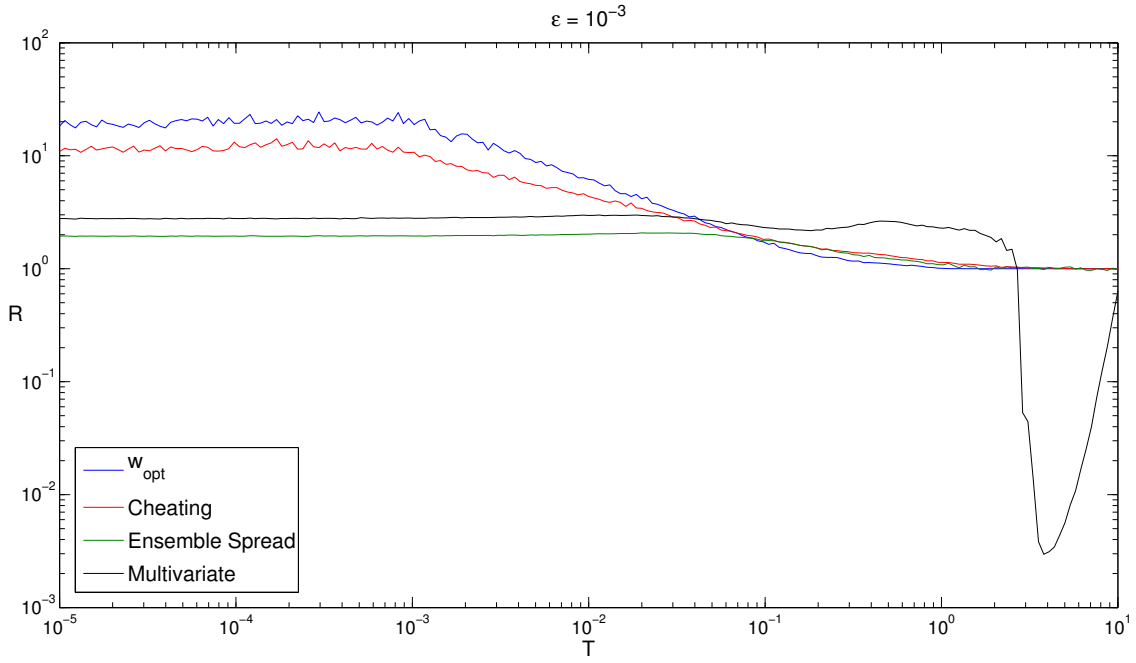

Figure 2.19: Error Reduction plot for the Multivariate Best Estimate method shows that it performs much better than the 'cheating' and fixed optimal weights case in the range of $T = 0.05 - 2$.

The method is seen to perform better by a factor of 2 than the cheating and fixed optimal weights case in the range of $T = 0.05 - 2$, although performing badly in the range of $T = 2 - 10$, where the method seems to be using the model more than it should. This might emerge from the normalization being performed on the different σ_{ij} components of the M matrix in the same way as in Eq. 2.33. The normalization is intuitively valid for the diagonal (σ_{ii}) terms. However, for the off diagonal terms (σ_{ij}, where $i \neq j$) it might not be the correct normalization. The multivariate analysis is performed again for varying δ values, without normalizing the

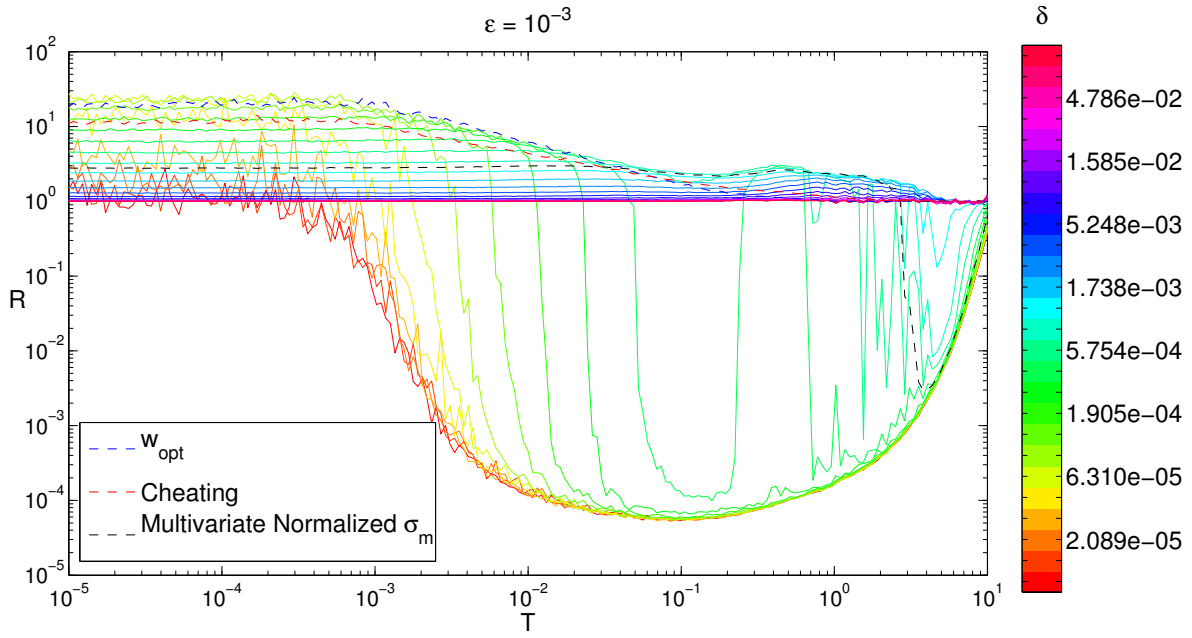

Figure 2.20: Error reduction plot for varying delta values without normalizing the components of the M matrix according to Eq. 2.33. The curve corresponding to $\delta \approx 1.6 \times 10^{-3}$ performs as good as the normalized case (seen as the broken black curve), and in the region of $T = 2 - 10$ performs better.

components of the M matrix, and the error reduction is plotted in Figure 2.20. It is seen from the figure that for a specific choice of $\delta \approx 1.6 \times 10^{-3}$, the error reduction works much better than the case of normalization (seen as the broken black curve).

Observing this, it can be asserted that the multivariate estimation for the Lorenz Model can be made to perform better with the right choice of δ, than to normalize the components of the model covariance matrix.

2.8.4 Best Estimate from Incomplete Observations

The last case studied in this section is one where the observation set is incomplete, and is only available for several of the few variables involved. Suppose $\vec{\psi}_o$ is a P-dimensional vector containing the observations, and H is an operator that converts the model variables $\vec{\phi}_m$ from N dimensional variable space to P dimensional observation space. Extending the method as described in Section 2.8.3, the W matrix for this case can be expressed as

$$W = MH^\top [O + HMH^\top]^{-1} \tag{2.43}$$

And the analysis can be expressed as

$$\vec{\phi}_a = \vec{\phi}_m + MH^\top [O + HMH^\top]^{-1} [\vec{\psi}_o - H\vec{\phi}_m] \tag{2.44}$$

The case considered here is one with observations available only in x, for which H is given as

$$H = \begin{bmatrix} 1 & 0 & 0 \end{bmatrix}$$

Also for this case, the observation error covariance matrix reduces to a single scalar value (as observations are one dimensional) and is given as

$$O = \epsilon^2$$

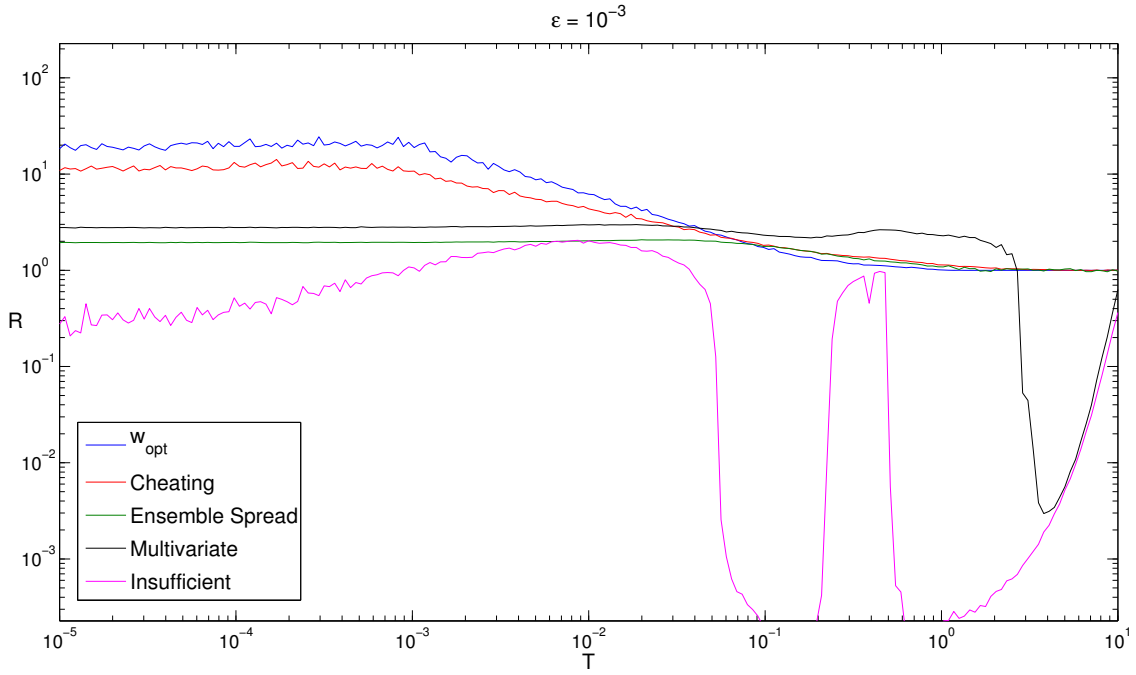

Figure 2.21: Error Reduction plot for the case of Insufficient Observations shows that the model performs badly being supplemented by observations in only one dimension.

Using Eq. 2.44 and the definition of M as given earlier, the analysis can be written as

$$\begin{aligned} x_a &= x_m + \frac{\sigma_{xx}^2}{\epsilon^2 + \sigma_{xx}^2}(x_o - x_m) \\ y_a &= y_m + \frac{\sigma_{xy}^2}{\epsilon^2 + \sigma_{xx}^2}(x_o - x_m) \\ z_a &= z_m + \frac{\sigma_{xz}^2}{\epsilon^2 + \sigma_{xx}^2}(x_o - x_m) \end{aligned} \tag{2.45}$$

This is similar to Eq. 2.42 to some extent, as the matrices reduce to scalars because the observation is 1-dimensional. The error reduction for this case is shown in Figure 2.21. It becomes increasingly difficult for the model to predict with any accuracy, and the error in prediction is much larger in this case. Consequently, the error reduction term becomes very small and even close to 0 for certain values of T.
This is not fair comparison, because the error reduction shown in Figure 2.21 is calculate using relative error obtained with predictions available in all the three dimensions. The method described in this section indeed performs badly throughout, as it is compared to a superior case, albeit primitive. Hence, another comparison for this specific case is done by first calculating E_{Obs} for each T value, using observations in x alone (while the model is free running in the other two dimensions), such that the analysis at each measurement is

$$\begin{aligned} x_a &= x_o \\ y_a &= y_m \\ z_a &= z_m \end{aligned} \tag{2.46}$$

The relative error is re-calculated and is shown in Figure 2.22, where the method is seen to now perform much better for a small range of T values, as compared to its simply observation assisted version of analysis.

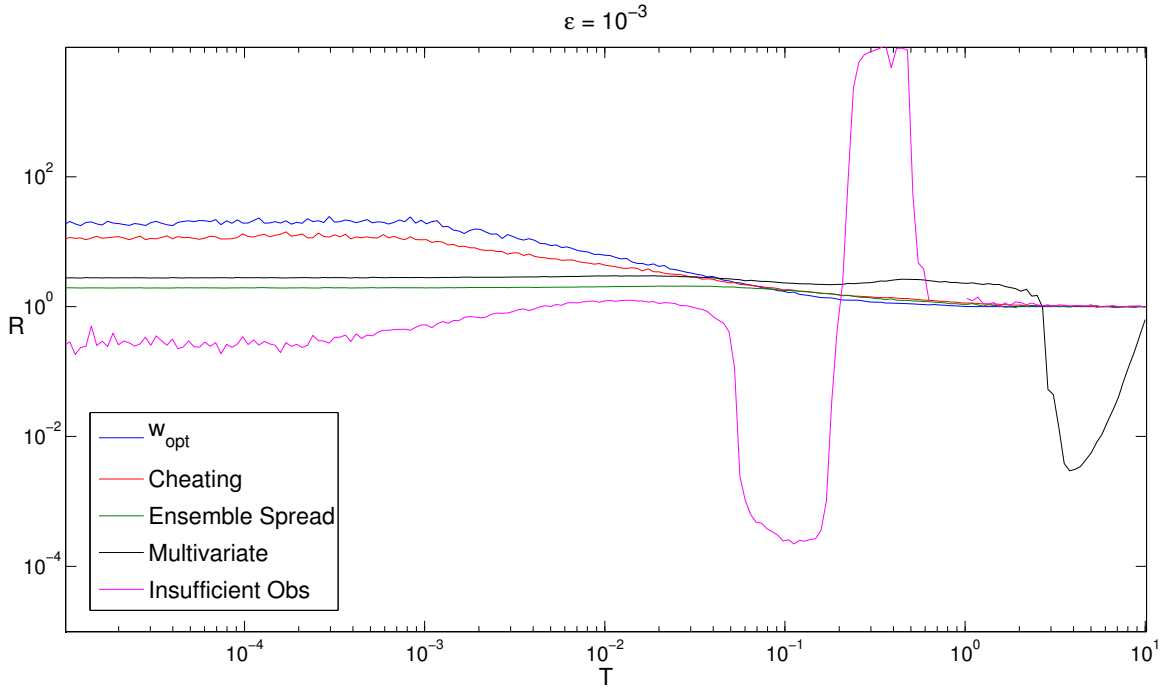

Figure 2.22: Error Reduction plot for the case of Insufficient Observations generated relative to a model run supplemented by observations only in x, where the analysis is given by Eq. 2.46.

In either case, being supplemented by observations in only one dimension for the highly chaotic Lorenz Model shows the limitation of predictability, which is also true for real physical models with multiple variables, where observations might not be available in the entire variable space. In such cases, this method is highly applicable, as it makes use of every available piece of information in the most optimal way.

This concludes the study on forecasting in the Lorenz Model. The issue of predictability extends to higher dimensional flows, that span several scales of motion. The atmospheric boundary layer is one such epithet, which has been the locus of interest for predictability, and holds relevance and purpose for science and society alike. The study now steers into modern flow simulation techniques like Large Eddy Simulations, studying how perturbations evolve through the various scales of turbulent motions that abound in the atmosphere shrouding predictability.

CHAPTER 3

Atmospheric Predictability: The Numerical Setup

The accurate description of turbulent fluid motion had been a subject of perennial scientific inquiry. Feynman even classified it as the last great unsolved problem of classical physics. As far back as the $15th$ century, the phenomenal polymath Leonardo da Vinci already started dabbling with fluid motion, pioneering the modern domain of 'flow visualization' in his attempts at understanding vortices in a turbulent fluid. He noted: "Observe the motion of the surface of water has two kinds of motion. One by its weight, the other by the direction of curls, thus the water has *eddying* motions, one part due to the principal current, the other due to a random and reverse motion."[Bell et al., 1970]. Lumley [1992] even commented that conceptually, this prefigures the now famous Reynolds decomposition of the Navier Stokes equations into a mean ($\overline{\phi}$) and a fluctuating (ϕ') component. Techniques developed over the years, aided with numeric computing, have evolved into present day methods for turbulence modeling like Large Eddy Simulations (LES) and Direct Numerical Simulation (DNS), that are capable of simulating three dimensional unsteady turbulent motions. The numerical techniques along with the set up used for this study are briefly described in this chapter.

3.1 Conserved Variables in the Atmosphere

In dealing with the atmospheric processes one often encounters the need to define certain conserved variables that can be easily studied. Of these, we shall focus only on the *potential temperature* θ as this study concerns a dry convective boundary layer. The potential temperature of an air parcel is defined as the temperature it would attain if brought adiabatically to some reference pressure. It is a conserved atmospheric variable in the absence of liquid water, and can be expressed as

$$\theta = \frac{T}{\Pi} \tag{3.1}$$

where Π is the *Exner function* given as

$$\Pi = \left(\frac{p}{p_0}\right)^{\frac{R_d}{c_p}} \tag{3.2}$$

Here, p is the pressure of the air parcel, p_0 is the reference pressure, R_d is the specific gas constant for dry air and c_p is the specific heat of air at constant pressure, and $R_d/c_p = 0.286$. This follows

from a simple derivation using the ideal gas law and the first law of thermodynamics and can be found in most texts on atmospheric physics like Seinfeld and Pandis [2012]. The temperature of an air parcel varies as the parcel ascends or descends, but its potential temperature remains conserved, hence making it easier to study.

3.2 Conservation Equations

Flow simulation techniques stem from numerical methods to solve the conservation equations that govern the physics of fluid motion. A numerical procedure is required because analytic solutions have yet not been found for the governing equations, barring the simplest flow configurations over simple geometries. The first equation is the *conservation of mass*, which can be written as

$$\frac{\partial \rho}{\partial t} + \frac{\partial (\rho u_i)}{\partial x_i} = 0 \tag{3.3}$$

where ρ is the density of the fluid, and u_i is the velocity in the x_i direction. Under an approximation of incompressibility (i.e. $D\rho/Dt = 0$) it reduces to the *continuity equation* given as

$$\frac{\partial u_i}{\partial x_i} = 0 \tag{3.4}$$

The continuity equation together with the conservation of momentum forms the set of Navier-Stokes equations. They are not written out here fully as this work does not directly focus on them. Instead, we review the equation for a conserved variable ψ (which can be θ) that can be written as

$$\overbrace{\frac{\partial \psi}{\partial t}}^{\text{Change in time}} + \underbrace{u_i \frac{\partial \psi}{\partial x_i}}_{\text{Advection}} = \underbrace{\frac{\partial}{\partial x_i} \nu \frac{\partial \psi}{\partial x_i}}_{\text{Diffusion}} + \underbrace{S}_{\text{Source}} \tag{3.5}$$

where the change in the variable in time is governed by an advection term, a diffusion term and a source term. An important technique in the formulation of turbulence arising out of these equations is the method of *Reynold's Decomposition*. A variable (ψ) is split into its mean ($\overline{\psi}$) and fluctuating (ψ') component as follows

$$\psi = \overline{\psi} + \psi' \tag{3.6}$$

Rewriting Eq. 3.4 in this form gives

$$\frac{\partial \left(\overline{u_i} + u_i'\right)}{\partial t} = 0 \tag{3.7}$$

and since

$$\frac{\partial \overline{u_i}}{\partial t} = 0 \quad \text{also} \quad \frac{\partial u_i'}{\partial t} = 0 \tag{3.8}$$

Equation 3.5 can now also be rewritten using turbulence decomposition, and can further be *averaged* into a form which is known as the *Reynolds Average* as follows

$$\overline{\frac{\partial \left(\overline{\psi} + \psi'\right)}{\partial t}} + \overline{\left(\overline{u_i} + u_i'\right) \frac{\partial \left(\overline{\psi} + \psi'\right)}{\partial x_i}} = \overline{\frac{\partial}{\partial x_i} \nu \frac{\partial \left(\overline{\psi} + \psi'\right)}{\partial x_i}} + \overline{S} \tag{3.9}$$

The bar over each term $\overline{(.)}$ represents an averaging operator. Using the equation of continuity, Eq. 3.9 can be written into

$$\frac{\partial \overline{\psi}}{\partial t} + \frac{\partial \overline{u_i}\,\overline{\psi}}{\partial x_i} = \frac{\partial}{\partial x_i}\nu\frac{\partial \overline{\psi}}{\partial x_i} + S - \frac{\partial \overline{u_i'\psi'}}{\partial x_i} \tag{3.10}$$

The first term on the right hand side of Eq. 3.10 is usually neglected, as the inertial forces largely dominate viscous forces in atmospheric flows. The last term involves the *turbulent flux* term which now enters the averaged conservation equation and is given as $u_i'\psi'$. Here u_i' is the turbulent velocity fluctuation in the direction x_i and ψ' is the turbulent fluctuation in the variable in the direction x_i. For instance $w'\theta'$ denotes the turbulent heat flux that is often encountered in this study, and relates the fluctuations in vertical velocity w and potential temperature θ, which shall be examined in more detail shortly. A brief description of the dynamics of the atmospheric boundary layer now serves a prelude to the numerical techniques that shall be described.

3.3 Atmospheric Boundary Layer - A Fugue in Turbulence

The Atmospheric Boundary Layer (ABL) is the lowest region of the atmosphere, and is influenced by the surface of the earth. Figure 3.1 shows a schematic of this region, marking its main features that are now described.

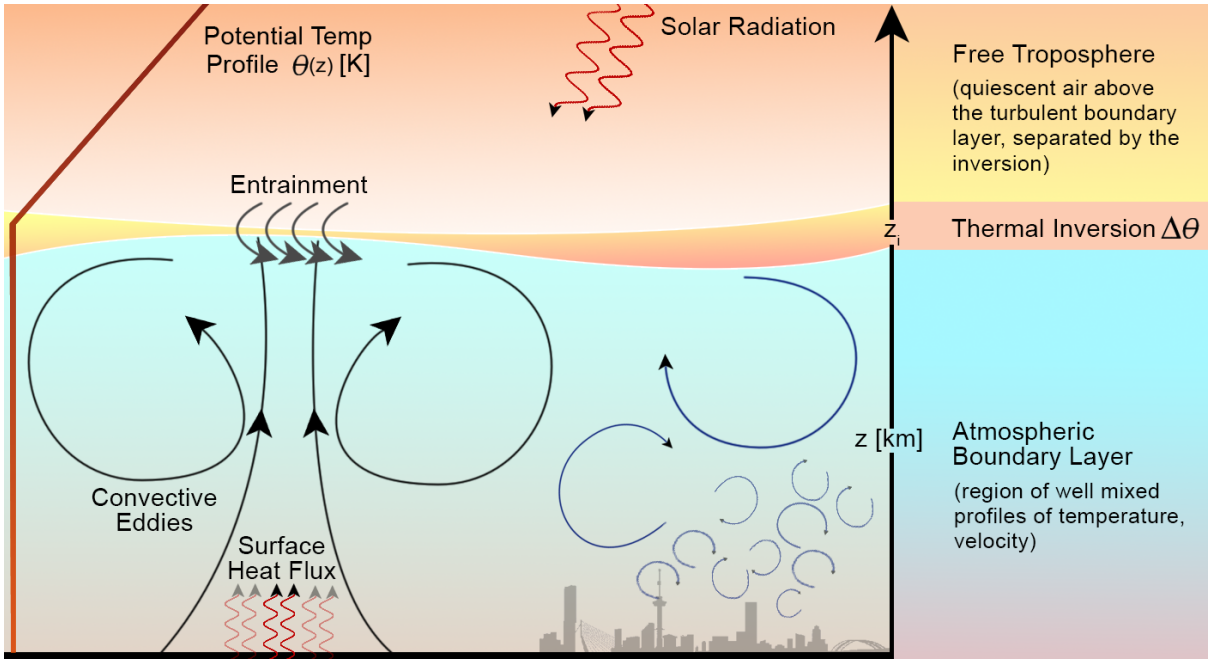

Figure 3.1: The schematic shows the lowest region of the atmosphere: the boundary layer, where the dynamics is influenced by the Earth's surface. The relevant features are illustrated, with convection driven by the surface heat flux, entrainment of quiescent air from above the thermal inversion into the growing atmospheric boundary layer, and a range of turbulent eddies that become smaller near the surface.

The ABL assumes myriad states of hydrodynamic stability throughout its evolution. Yet of these varied states, a highly turbulent regime is the most ubiquitous. It also undergoes a rather cyclic dynamic, specially over land where it has a diurnal cycle. Heated by solar radiation, the

land invigorates a convective motion through rising plumes which is the onset of the ABL growth. The potential temperature profile which is uniform within the well mixed boundary layer is capped by a thermal inversion. The inversion layer strength greatly determines the ABL growth which is slow for a stronger inversion case and vice versa. A jump in the potential temperature profile ($\Delta\theta$) at the inversion height z_i (which is followed by a lapse rate thereafter) acts as a physical barrier for the impinging thermal plumes rising from the surface, as seen in Figure 3.1. If $\Delta\theta$ is high, these thermals are forced to spread more laterally, temporarily thinning the inversion layer. In case of a weak inversion, these plumes are able to break through the capping layer into the air above. In either case, following a slightly different dynamic, entrainment mixes in air from above the inversion into the boundary layer which is then homogenized by the action of turbulence. This causes the boundary layer to grow gradually, also modifying the vertical temperature profile [Sullivan et al., 1998], which is shown subsequently in Figure 3.2. The growth of the boundary layer can alternatively be also driven by shear. This research focuses on convectively driven growth.

Further, within the *mixed layer*, a scaling velocity $w_\star$ and a scaling temperature $\theta_\star$ can be defined [Finnigan and Kaimal, 1994] as follows, such the statistical properties of turbulence in the mixed layer, non-dimensionalized with these numbers are functions of z/z_i

$$w_\star = \left[\frac{g}{\bar{\theta}}(\overline{w'\theta'})_0 z_i\right]^{1/3} \qquad (3.11)$$
$$\theta_\star = \frac{(\overline{w'\theta'})_0}{w_\star}$$

where g is the gravitational acceleration, $\bar{\theta}$ is the potential temperature in the mixed layer, $(\overline{w'\theta'})_0$ is the surface thermal flux that is imposed and the average inversion height is given by $\bar{z_i}$. As the convective motions begin, they broaden the spectrum of turbulent scales, making it increasingly difficult to fully represent the flow. Numerical techniques like LES and DNS are increasingly applied to this problem of studying turbulence in convective boundary layers, treating the system as an initial value problem and numerically solving it in time. However, the turbulent motions form a highly chaotic system, and any error in estimating the initial conditions, or perturbations in the flow, upon modeling, will cause the solution to rapidly diverge to yield a state not very different from an arbitrarily chosen final state that the system can assume. Such a proposition strongly presages loss of predictability.

3.4 Large Eddy Simulations

In LES, the energy containing larger three-dimensional scales of motion (that are not universal and are affected by the flow geometry) are directly represented, whereas the smaller scale motions (which are somewhat universal in nature), are modeled. In essence, it solves the governing equations for the flow over the specified *grid* of computation for the *filtered variables*, and all the sub-filter scale motions smaller than the grid are *modeled* using a turbulence closure to calculate the turbulent flux terms. In an LES set up, Eq. 3.10 (after neglecting the molecular diffusion term with the assumption that the turbulent flux dominates) is usually written as

$$\frac{\partial\widetilde{\psi}}{\partial t} + \frac{\partial\widetilde{u_i}\widetilde{\psi}}{\partial x_i} = S - \frac{\partial\widetilde{u_i'\psi'}}{\partial x_i} \qquad (3.12)$$

where $\widetilde{\psi}$ denotes the filtered variable. The sub-filter scale turbulent flux is modeled as

$$\widetilde{u_i'\psi'} = -K\frac{\partial\widetilde{\psi}}{\partial x_i} \tag{3.13}$$

where the new term introduced is K, which is called the *Eddy Viscosity*. It assumes a "diffusive" property for the small eddies (at the sub-filter scale) acting in favor of turbulent mixing and dissipation. Using this assumption, Eq. 3.12 can be rewritten as

$$\frac{\partial\widetilde{\psi}}{\partial t} + \frac{\partial\widetilde{u}_i\widetilde{\psi}}{\partial x_i} = S + \frac{\partial}{\partial x_i}K\frac{\partial\widetilde{\psi}}{\partial x_i} \tag{3.14}$$

The term K has been modeled in several ways in different studies based upon local gradients in the physical variables. The LES employed in this study (DALES, see Section 3.5) models K in the following manner

$$K = c_m\lambda e^{1/2} \tag{3.15}$$

where $c_m = 0.12$ is a constant, $\lambda = \Delta$ is a length scale, with $\Delta = \sqrt[3]{\Delta x\Delta y\Delta z}$ (where Δx,Δy and Δz are the LES grid box resolutions in the x, y and z directions respectively) and $e = \frac{1}{2}\widetilde{u_i'u_i'}$ is the sub-filter scale turbulent kinetic energy. For details see Heus et al. [2010].

The contribution of the sub-grid to the solution is usually limited, although near the surface where small scale motions dominate, it has a considerable contribution. Since K varies for each grid box, it models the fluid differently for different regions of the flow.

3.5 Case Setup with DALES

For the purpose of this study, the Dutch Atmospheric Large Eddy Simulation (DALES 3.1.1) code is used [Heus et al., 2010]. A standard case is chosen from Sullivan et al. [1998], corresponding to the *weak 06* (W06) specifics, which models a dry convective boundary layer growth, capped by a weak inversion of $\Delta\theta = 0.607$ K, and driven by a surface flux Q_0 $\left[\overline{w'\theta'}_0\right]$ of 0.060 K m/s. All the simulations are performed over a $3600 \times 3600 \times 1920$ m^3 domain in x, y and z, with periodic boundaries in the lateral directions, no slip boundary at the bottom and a sponge layer at the top (where fluctuations in the velocity and scalars are damped out using forcing/source terms added to the transport equations). The simulation proceeds with an adaptive time stepping scheme obeying the CLF law (with a fixed upper bound on the cell Courant number).

To study the growth of perturbations, DALES was modified by including a subroutine that creates perturbations and reports their evolution for ensembles of identical simulations. This study is limited to ensemble pairs, where one of the two identical simulations is perturbed at a specified *seeding* time. As the simulations diverge, they can have disparate time steps, hence proceeding asynchronously. To facilitate comparison between the two, the calculations for both the simulations are done with the smaller of the two time steps. To demonstrate the simulation of boundary layer dynamics, a sample LES using the setup described above is performed for a dry convective boundary layer over seven hours. The hour averaged vertical profiles of the potential temperature are shown in Figure 3.2.

It is seen that with each hour, the potential temperature profile shows warming (going from the blue to the red curve). This occurs because the boundary layer is constantly heated by the imposed surface flux. The profile is near vertical within the *mixed layer*, showing that

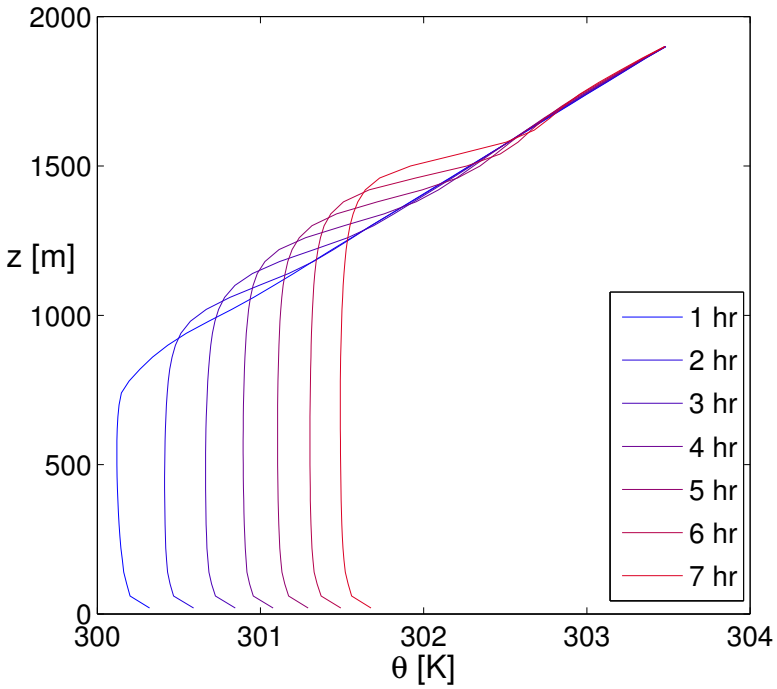

Figure 3.2: Boundary layer growth and the evolution of the vertical temperature profile. The sharp jump in the θ field marks the inversion layer, below which lies the mixed layer where θ is almost constant.

under the action of turbulence the boundary layer is well mixed. The inversion layer which is characterized by the jump in the potential temperature profile (the maximum gradient in θ) is also seen to grow from around 800 m in the first hour to 1500 m in the seventh hour, which shows the growth of the ABL following the dynamics described in Section 3.3. The flux profiles are described later in Section 3.7.

3.6 Direct Numerical Simulations

A DNS fully resolves all scales of motion in a turbulent fluid by numerically solving the Navier-Stokes equations completely. Conceptually it is the simplest method, providing an unrivaled insight into the flow characteristics. However, it makes these simulations highly computationally intensive, limiting DNS to low Reynolds number flows. In this research, the DNS simulations are done with a modified version of DALES. The *Eddy Viscosity* K in Eq. 3.14 is replaced by the kinematic viscosity ν. In effect, this reduces to the original equation of the conservation of a variable

$$\frac{\partial \psi}{\partial t} + \frac{\partial u_i' \psi'}{\partial x_i} = S + \frac{\partial}{\partial x_i} \nu \frac{\partial \psi}{\partial x_i}$$

The method must all the scales of motion present in the flow, the smallest of which are determined by the fixed viscosity which now causes the sub-grid model to represent molecular diffusion.

Although it stems from the LES code, this method of fixing the viscosity simulates a DNS very well. It is computationally unfeasible to simulate high Reynolds number flows, hence the viscosity cannot be arbitrarily reduced. This renders the DNS unable to sustain a thermal

inversion in the vertical profile of potential temperature by itself. This is due to a large diffusive entrainment flux which dissolves the sharp jump in potential temperature. To counter this effect and maintain a fixed inversion height, the domain is limited to a size of $3600 \times 3600 \times 960$ m^3 (i.e. half the LES domain in the vertical direction), and a fixed entrainment flux ratio is imposed at the top of the domain. This is given as ratio between the heat flux at the inversion and surface flux $\overline{w'\theta'}_{z_i}/\overline{w'\theta'}_0 = -0.2$, which is close to the value observed for the growth of a shear free convective boundary layer [Deardorff et al., 1980], and also that resolved by the LES. It acts as a solid boundary for the impinging thermals, which spread out laterally and unlike the LES, cannot penetrate the inversion layer. This impacts the variance production zones in turn, and the DNS simulations do not have the inversion layer as a large variance production zone and its contribution remains limited.

The vertical profile of $\overline{w'\theta'}$ is shown in Figure 3.3 as the solid black line which goes steadily from 0.06 K m/s at the surface to -0.01 K m/s at the top of the domain which is at 960 m. It is seen to closely follow the complete profile obtained from the LES (broken green line) upto the top of the DNS domain, which marks the inversion height for these simulations.

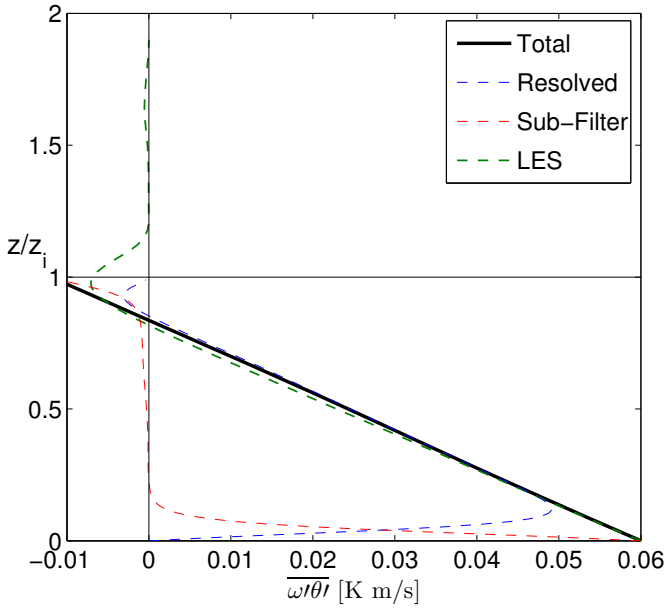

Figure 3.3: Vertical profile of the turbulent flux $\overline{w'\theta'}$ in the DNS and LES versions of DALES. It is seen to steadily decrease from 0.06 K m/s at the surface to 0.01 K m/s at the inversion height. The broken green curve shows the complete profile from the LES simulations.

Further, the evolution of the vertical potential temperature profile is shown in Figure 3.4, which is seen to closely resemble that obtained from the LES simulations upto the imposed inversion height. The solid curves show this evolution for a sample DNS simulation, along with the broken curves that show their LES counterparts. Unlike the LES, the boundary layer *cannot grow* in the DNS and remains at a fixed height of 960 m. The temperature profile evolves as the simulation proceeds and the shifts more to the right, wherein the potential temperature in the mixed layer gradually increases, strengthening the convective eddies.

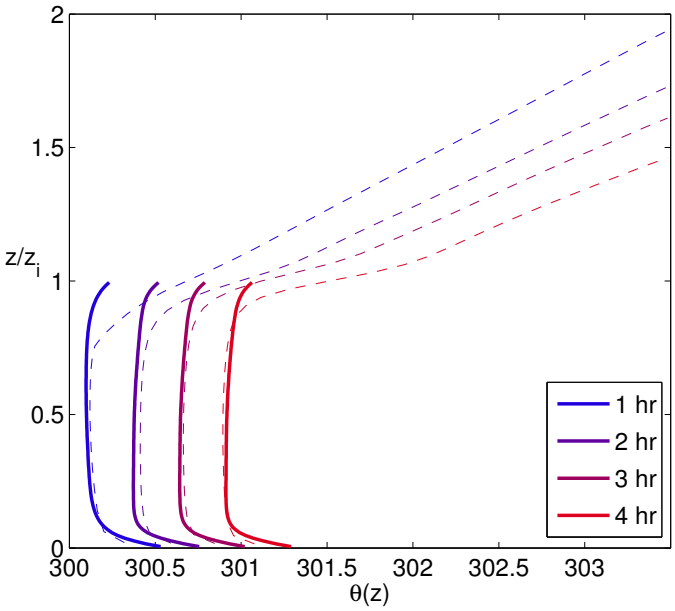

Figure 3.4: Evolution of the vertical potential temperature profile in a sample DNS simulation shows that it closely follows the complete profile obtained from the LES (broken curves) upto the inversion layer height.

3.7 Vertical Flux Profiles

Turbulent fluctuations form the major component of variance in the physical variables, and can play an important part in the growth of error, making the variance production zones sources of error. The vertical profiles of these variables are partly resolved and partly modeled by the LES. The temperature variance budget can be found from the potential temperature budget equation, which was given as

$$\frac{\partial \theta}{\partial t} + u_i \frac{\partial \theta}{\partial x_i} = \frac{\partial}{\partial x_i} \nu \frac{\partial \theta}{\partial x_i}$$

Multiplying by θ, we get

$$\theta \frac{\partial \theta}{\partial t} + \theta u_i \frac{\partial \theta}{\partial x_i} = \theta \frac{\partial}{\partial x_i} \nu \frac{\partial \theta}{\partial x_i} \tag{3.16}$$

which can be then rearranged to arrive at

$$\frac{1}{2}\frac{\partial \theta^2}{\partial t} + \frac{1}{2}\frac{\partial u_i \theta^2}{\partial x_i} = \nu \left[\frac{1}{2}\frac{\partial^2 \theta^2}{\partial x_i^2} - \left(\frac{\partial \theta}{\partial x_i} \right)^2 \right] \tag{3.17}$$

Applying Reynolds decomposition to these terms with an assumption of horizontal homogeneity [Finnigan and Kaimal, 1994] gives

$$\overbrace{\frac{1}{2}\frac{\partial \overline{\theta'^2}}{\partial t}}^{\text{Change in Variance}} = \underbrace{-\overline{w'\theta'}\left(\frac{\partial \bar{\theta}}{\partial z}\right)}_{\text{I}} - \underbrace{\frac{1}{2}\frac{\partial \overline{w'\theta'^2}}{\partial z}}_{\text{II}} - \underbrace{N_\theta}_{\text{III}} \tag{3.18}$$

The first term on the right hand side of the equation is the variance production term. It is given as the product of two components, the *covariance* of w and θ [i.e. $\overline{w'\theta'}$] and the *gradient* in the vertical potential temperature profile $\left[\partial\bar{\theta}/\partial z\right]$. An hour-averaged profile of $\overline{w'\theta'}$ and θ is shown in Figure 3.5 for a sample LES case.

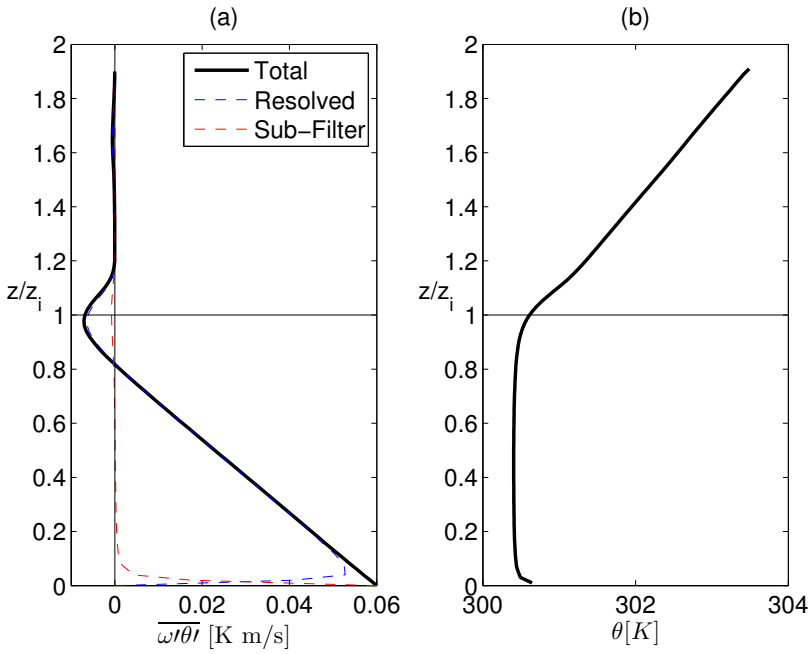

Figure 3.5: Vertical profiles of the components of the variance production term in Equation 3.18 for a sample LES case. Part (a) shows the *covariance* component $\overline{w'\theta'}$, and part (b) shows the vertical potential temperature profile.

The total turbulent flux $\overline{w'\theta'}$ is seen as the solid line in Figure 3.5.a, which is strongly positive near the surface, linearly decreasing with height to a negative value close to $z/z_i = 1$. The *sub-filter* contribution (in red) is largest near the surface, and within a few z levels, the *resolved* component (in blue) dominates the sum. Physically, when this term is positive, turbulent fluctuations transport relatively warmer air upward and cooler air downward, and both the variables are said to be positively correlated. Figure 3.5.b shows the vertical potential temperature profile, which has a negative gradient near the surface, is constant in the mixed layer and has a strongly positive gradient near the inversion, following a lapse rate thereafter. It can be seen that the variance production term is positive near the surface, (as $\overline{w'\theta'}$ is positive, and $\partial\bar{\theta}/\partial z$ is negative), and similarly at the inversion, and is shown in Figure 3.6.

Although the values appear to be small for the production zones, the variance of potential temperature $\overline{\theta'^2}$ is seen to be quite pronounced in these regions, the vertical profile of which is shown in Figure 3.6.b. These two zones are seen to be crucial for the production and growth of error in the subsequent sections. Term II of Eq. 3.18 represents the turbulent transport of variance, and is responsible for the advection of variance through the domain (specifically in the mixed layer where the production is zero). The last term (III) represents the dissipation rate of half the temperature variance, and is a sink term which depletes variance by the action of the smallest eddies in the Kolmogorov spectrum.

These two profiles are now shown for a sample DNS case in 3.7. There is a markedly strong production zone near the surface, which reflects in the variance profile of θ, whereas contrary to the LES, the near inversion profile does not show a pronounced peak for the DNS simulations.

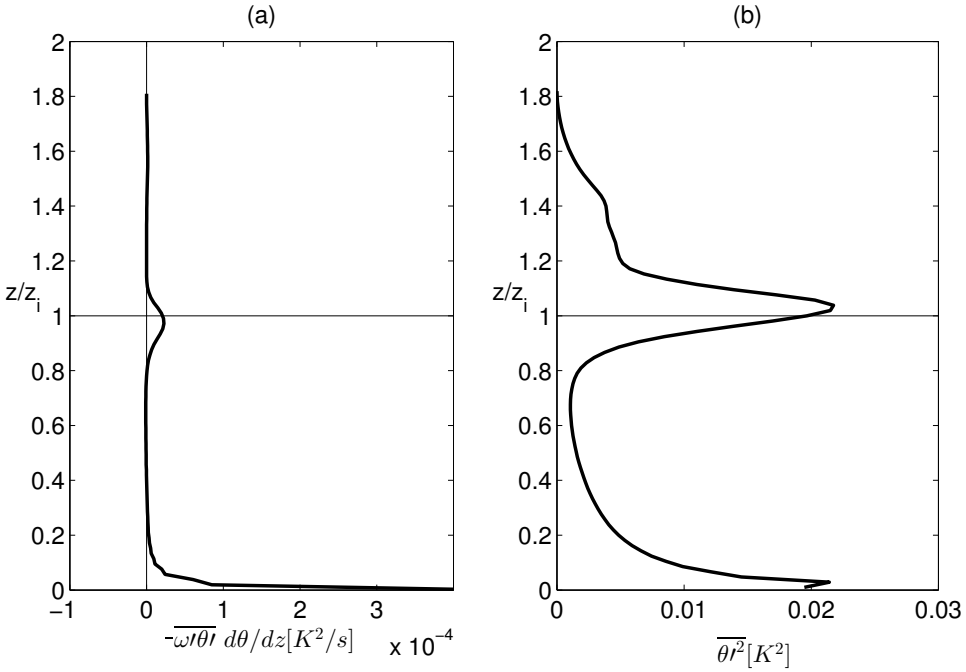

Figure 3.6: Vertical profiles of the variance production term from Eq. 3.18 and the potential temperature variance for a sample LES case.

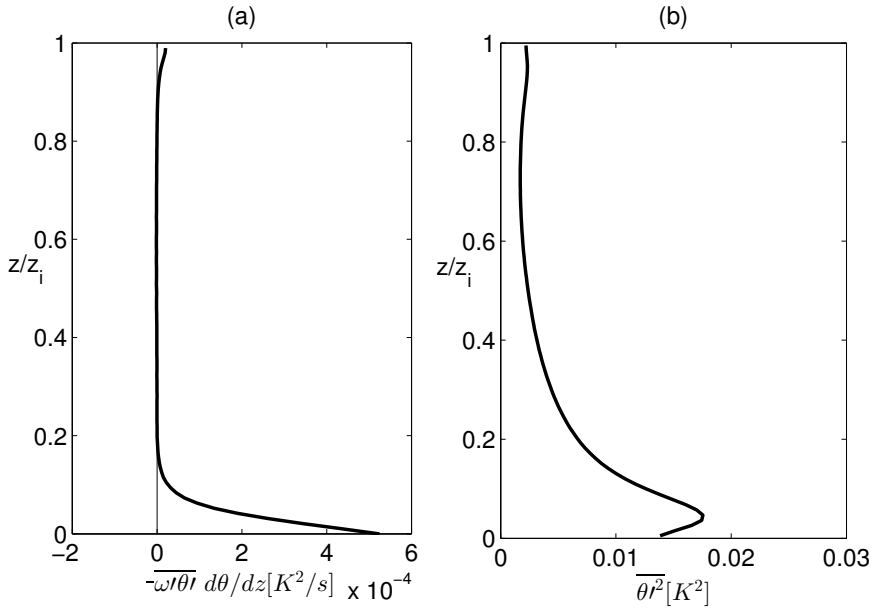

Figure 3.7: Vertical profiles of the variance production term [part (a)] and the variance of θ [part (b)] shows the surface to be the main source of variance.

3.8 Defining the Reynolds Number

The most daunting feature of atmospheric flows is that the waltz of turbulent eddies spans several orders of magnitude, ranging from a few thousand kilometers (associated with expansive mesoscale systems), to a few millimeters (near the Kolmogorov scale). Typically, such systems can have $Re \sim 10^8$ [Oboukhov, 1962], which makes it impossible to simulate the complete scales of motion. In this research, a limited range of Reynolds numbers is considered, which still provides sufficiently resolved turbulence to study the dynamics of perturbations over numerous scales of motion. The methods to characterize the LES and DNS Reynolds number are now described.

3.8.1 LES Reynolds Number

In the LES, the smallest scales are not resolved, and further, the eddy viscosity varies from region to region, making it difficult to characterize a Reynolds number based upon a bulk fluid viscosity. It is hence constructed based upon characteristic length scales. The first length scale is z_i or the *inversion layer* height (explained in Section 3.3), which marks the size of the largest energy containing eddies. The second is the characteristic length scale of the grid boxes (corresponding to the smallest resolved scale) $\Delta = \sqrt[3]{\Delta x \Delta y \Delta z}$. The LES Reynolds number [Sullivan and Patton, 2011] can then be approximated as

$$Re_l \sim \left(\frac{z_i}{\Delta}\right)^{4/3} \tag{3.19}$$

This shows that as the resolution becomes finer (yielding a smaller Δ), Re_l increases and smaller scales are resolved in a more turbulent environment. In this way, a LES maintains a balance between resolved and modeled turbulence. The amount of turbulence in the flow is highly dependent upon the resolution of the simulation.

3.8.2 DNS Reynolds Number

Since the viscosity of the flow is fixed in a DNS, a characteristic Reynolds number of the flow in the *mixed layer* can be calculated as

$$Re = \frac{z_i w_\star}{\nu} = \frac{z_i}{\nu}\left[\frac{g}{\overline{\theta}}\overline{w'\theta'}_0 z_i\right]^{1/3} \tag{3.20}$$

where z_i is the inversion height, ν is the kinematic viscosity, g is the acceleration due to gravity, $\overline{\theta}$ is the uniform potential temperature in the mixed layer, and $\overline{w'\theta'}_0$ is the surface heat flux [Finnigan and Kaimal, 1994].

3.9 Wavenumber Spectra of Turbulence

The description of turbulence greatly benefits from the elegant grammar of a *wavenumber space* representation of the energy contained in different scales of the system. To recall, the one dimensional Discrete Fourier Transform of a function ψ_x is given as

$$\hat{\mathcal{F}}_k = \sum_{x=0}^{N_x-1} \psi_x e^{-2\pi i x k / L_x}$$

Where the function ψ_x can be a physical variable along the x direction, such that $\psi_x \in \{\theta, \Delta\theta, w\}$, distributed over the domain length L_x and $\hat{\mathcal{F}}_k$ gives the contribution of the scalar dimensionless wavenumber k to the total function. Note that the exact definition of k varies from one text to another. Here it is expressed as a dimensionless number k, which represents the *number of oscillations* over the domain length L_x. The physical scale can be calculated as $\tilde{k} = k/L_x$ [m^{-1}]. Further, the power spectrum can be computed from the Fourier Transform as was mentioned in Eq. 2.8, which gives the energy contained in each wavenumber.

A classical portrait of isotropic turbulence (at high Reynolds numbers) has often been fashioned as a power spectrum, with an energy containing range of eddies corresponding to small wavenumbers, followed by an inertial sub-layer and a dissipation range at the higher end of wavenumbers. The larger eddies that feed in kinetic energy correspond to the smallest wavenumbers (k_0) and their motion is entirely dominated by inertia. In such flows, a range of smaller scale motions exist, associated to wavenumbers $k \gg k_0$ that have a universal form uniquely determined by the viscosity ν and rate of energy transfer at the larger scales ε, which is called the *inertial sublayer* and follows from *Kolmogorov's first similarity hypothesis*. Here, the energy spectrum function $E(k,t)$ depends only on the Fourier coefficients with magnitude k and follows the famous "$-5/3$ power law". The shape of this spectrum, non-dimensionalized, is self similar and has a universal form [Batchelor, 1953]. Also widely separated from the energy containing range is the dissipation range of wavenumbers k_d starting from a critical value and extending upto $k \sim \infty$. These eddies lie in what is now called the "Kolmogorov range", and act as a sink for the kinetic energy in the system. At this scale, the inertial and viscous forces become comparable and the Reynold's number locally drops to 1.

This study extensively deals with perturbation fields (described in Section 3.10), and how they interact and propagate with the different scales of turbulence. They are mostly referred to with their wavenumbers which makes it easy to distinguish different scales.

3.10 Perturbation Field

To study the growth of error in the ABL, a perfect knowledge of its background state is assumed, which serves as the control run. An ensemble pair is then created by slightly perturbing one of the two identical simulations after a *spin-up* time of 1 hour (by when the dynamics of the ABL sufficiently evolves), which is called the *seeding*. This is done by adding a sinusoidal perturbation of a specified wavenumber to the θ field. The amplitude of this perturbation is taken as ϵ_0. This is such that

$$\theta(i,j,k) = \theta(i,j,k) + \epsilon_0 \sin(2\pi k\, i/N_x) \sin(2\pi k\, j/N_y) \tag{3.21}$$

where i, j and k vary from 1 to N_x, N_y and N_z respectively, which are the number of grid points in the three directions of the LES domain. In this manner, the field is perturbed throughout the 3D volume, although the perturbation can be readily modified as a planar or line source of initial error. Figure 3.8 shows how this perturbation field looks from the top for two values of k. Smaller $\tilde{k}$ values perturb the larger scales of motion whereas larger $\tilde{k}$ values perturb the smaller scales. This can be better seen in Figure 3.9, where the two different perturbations are added to a sample background field.

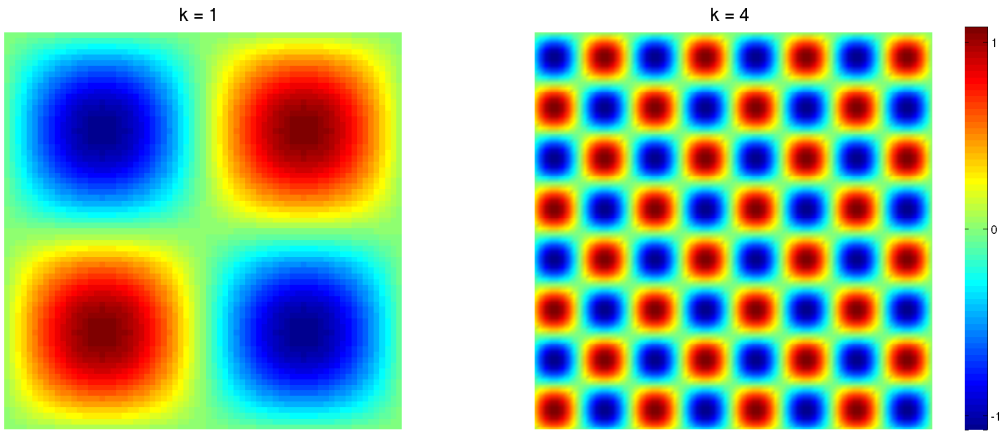

Figure 3.8: The sinusoidal perturbation fields for $k = 1$ and $k = 4$ with a magnitude ϵ as seen from the top. Larger k values perturb the smaller scales of motion and vice versa.

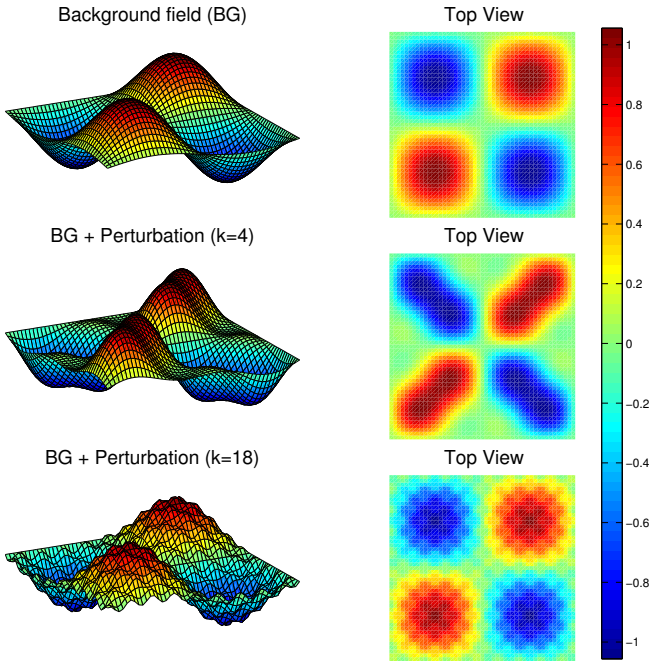

Figure 3.9: The effect of the sinusoidal perturbation field is seen for two wavenumbers $k = 4$ and $k = 18$ on a simple background field. It can be seen how the choice of k selects the scales of the system to be perturbed.

3.11 RMS Error

To study the difference between the two runs, the error is calculated as the volume averaged root mean square of the difference over the entire domain as follows

$$\delta(t) = \sqrt{\frac{\sum_{i=1}^{N_x}\sum_{j=1}^{N_y}\sum_{k=1}^{N_z}\left(\theta_1^t(i,j,k) - \theta_2^t(i,j,k)\right)^2}{N_x N_y N_z}} \tag{3.22}$$

where θ_1^t & θ_2^t are the potential temperature fields for the 2 runs in the ensemble pair at a time t. Also for the purpose of visualization and subsequent power spectrum analysis, the difference between the two runs is reported as $(\theta_1^t - \theta_2^t)$ at a chosen fixed vertical and horizontal plane.

3.12 Slices of the Error Field

For the purpose of visualization and power spectrum analysis, a slice of the error field is also reported for each time step after seeding. The vertical slice at the middle of the domain is given as

$$\Delta\theta(i,k) = \theta_1(i,k) - \theta_2(i,k) \tag{3.23}$$

where i and k are the number of grid points in the x and z directions. Note that $\Delta\theta$ (not to be confused with the jump in the potential temperature at the thermal inversion) gives the difference between the θ fields in the two simulations at each time t. The horizontal slice is also reported in a similar manner.

3.13 Error Energy Spectrum

The error energy spectrum is calculated by first performing a *Fast Fourier Transform* along one direction of the error slice, and then taking the mean over the other direction. For the vertical slice of error this amounts to first an FFT in the x direction, then taking the mean over the z direction. The error energy spectrum is then calculated according to Eq. 2.8. This gives the distribution of the energy over the *dimensionless wavenumber* k. Its physical scale can be calculated as $\tilde{k} = k/L_x$ [m^{-1}] where L_x is the domain length in the direction of the FFT.

This sets us up for studying the evolution of perturbations in an evolving boundary layer. First, the results from the LES studies are discussed in Chapter 4.

CHAPTER 4

Large Eddy Simulations

Large eddy simulations of the turbulent atmospheric boundary layer are now studied for the evolution of perturbations. A sample case is examined to establish whether the error grows in these simulations, and to find its general characteristics. A simulation pair with resolution $\Delta x, \Delta y = 25$ & $\Delta z = 20$ m is used, which is seeded at a time of 1 hr with a sinusoidal perturbation of magnitude $\delta_0 = 10^{-6}$ K and wavenumber $k = 18$, at a z level corresponding to 500 m.

Evolution of the RMS Error

The evolution of the RMS error in the θ fields of the simulation pair (as described in Section 3.11) is shown below in Figure 4.1.

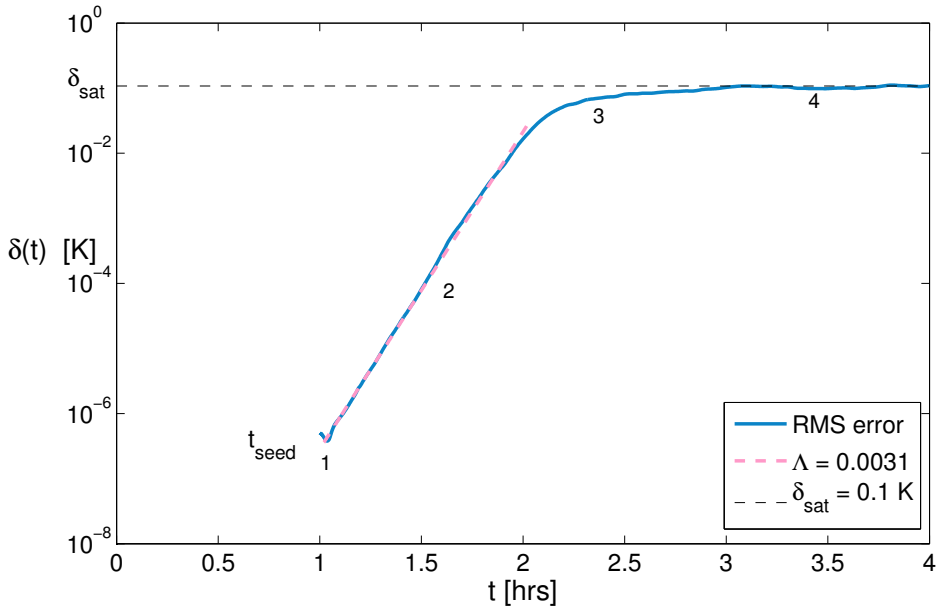

Figure 4.1: Evolution of the RMS error in the LES simulation pair for a sample case shows that the error grows at a constant exponential rate after seeding, upto its saturation value. An exponent can be found for the *growth* phase to express the error as $\delta(t) = e^{\Lambda t}$.

Figure 4.1 shows that the error clearly grows in the LES at an exponential rate (note the logarithmic y axis) upto a saturation value marked as δ_{sat}. This feature is highly reminiscent of the average error growth in the Lorenz model (see Figure 2.3). It is also remarkable how within a short span of 1.5 hours, a very small error ($\sim 10^{-6}$ K) grows over several orders of magnitude to the fuller scales of the system. The hallmarks of a chaotic system, namely extreme sensitivity to initial conditions and an exponential error growth, make themselves evident.

The growth is further marked by a Lyapunov exponent, which can be found from the best exponential fit using a method of least squares to the phase of constant RMS error growth. It is found that $\Lambda = 0.0031$, which describes error growth of the form $\delta_t = \delta_0 e^{\Lambda t}$. Lastly, the RMS error growth shows four phases which shall be further investigated, namely 1.) an *initial phase* which follows the seeding, and is marked by a small reduction in the error attributed to dissipation 2.) a region of *constant exponential growth* which starts after the initial dissipation phase, and lasts upto 3.) a region of *transition to saturation*, and finally 4.) the *saturated phase* of the error. An identical behavior is also noted for the error in the vertical velocity (w) field, yielding the same value of Λ, and is not shown here. We limit ourselves to the analysis of the θ field in this study.

Evolution of the Error Energy Spectrum

The error field along with its spectrum is shown together in Figure 4.2 for four time instances.

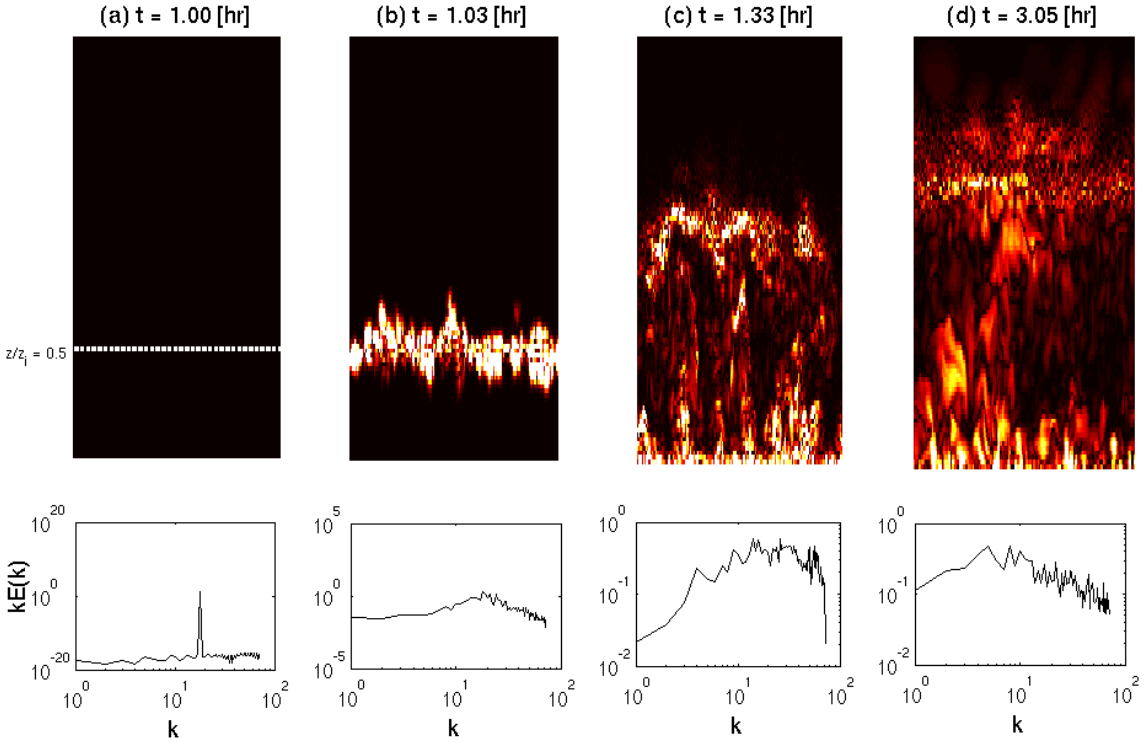

Figure 4.2: Comparison of the Power Spectra during stages of evolution of the error show in (a) the seeding at $t = 1$ [hr], with a single peak in the power spectrum at $k = 18$; (b) soon thereafter at $t = 1.03$ [hr] during the reduction in error phase shows a rapid redistribution of energy across wavenumbers; (c) at $t = 1.33$ [hr] during the constant exponential growth phase showing the predominance of the higher wavenumebers; (d) in the saturated phase at $t = 3.05$ [hr] shows an energy spectrum similar to the turbulence spectrum for θ.

Panel (a) shows the perturbation seed which peaks at a single wavenumber ($k = 18$) in the power spectrum. Next, in panel (b) the perturbation is seen to rapidly span out through the entire spectrum in the short regime when the RMS error reduces initially due to dissipation, before it again starts to grow after the onset of error production. The third panel (c) shows that soon thereafter, a constant exponential growth sets in, and the error increases with a fixed Lyapunov exponent. In this phase, the balance of energy is tipped largely towards the smaller scales, more energy being contained in the higher wavenumbers as is seen in the power spectrum. This self similar shape of the power spectrum during the phase of constant exponential error growth is seen for all the subsequent LES studies as well. The last panel (d) shows the error after saturation, which resembles a θ field, and the power spectrum returns to dominance by larger scales or smaller wavenumbers, characteristic of the power spectrum of a turbulent physical variable. The dependence of error growth on the characteristics of the perturbation is now be examined.

Experiments With Perturbations

The dynamics of error propagation through the various scales of turbulent motion could be probed using an inexhaustible array of methods. Several easily controllable parameters defining the perturbation are hence isolated, which are tested in the following sections. These include the wavenumber of the perturbation field, the location of the error in the boundary layer etc., constructing several experiments with perturbations in an attempt to understanding the phenomena of error propagation.

4.1 The Effect of Perturbation Wavenumber

Turbulence is marked by a superposition of multiple scales of motion, where perturbations to a specific scale evolve over the associated timescale. For instance, smaller turbulent structures have a shorter lifetime, and the error is expected to grow more rapidly for these higher wavenumbers, then triggering a slower growth in the larger structures with smaller wavenumbers, until the error grows to the scales of the system and saturates. This is the generally accepted mechanism for error growth in systems with a superimposition of multiple scales [Lorenz, 1969; Rotunno and Snyder, 2008; Morss et al., 2009].

The first parameter that is studied is the wavenumber of the perturbation field (ref Figure 3.8). Discretizing the domain to 288 points in the x and y directions and 192 points in the z, the wavenumber k is varied from $4 - 36$ ($\tilde{k} = 0.001 - 0.01$ m^{-1}) for a perturbation with magnitude of 10^{-6} K which is introduced throughout the volume. The growth of the RMS error upto saturation is shown for the different cases in Figure 4.3.

Strikingly, the rate of error growth is seen to be *independent* of the perturbation wavenumber, and after a brief initial phase each case attains to the constant growth phase with its characteristic Lyapunov exponent, until the error saturates. In the initial transient period, there is a drop in the error, which is larger for the higher wavenumber perturbations. This might be alluded to the initial dissipation of the error field, which is a phenomena acting on the smaller scales which have sharper gradients and dissipate more than the larger scales characterized by milder gradients. Convergence to the constant exponent shows that the growth of error follows from a similar mechanism after perturbing any scale of the system. This hints at a redistribution of the error energy to its governing modes within the short initial phase, which is further investigated in the subsequent study. Next, the effect of introducing the perturbation

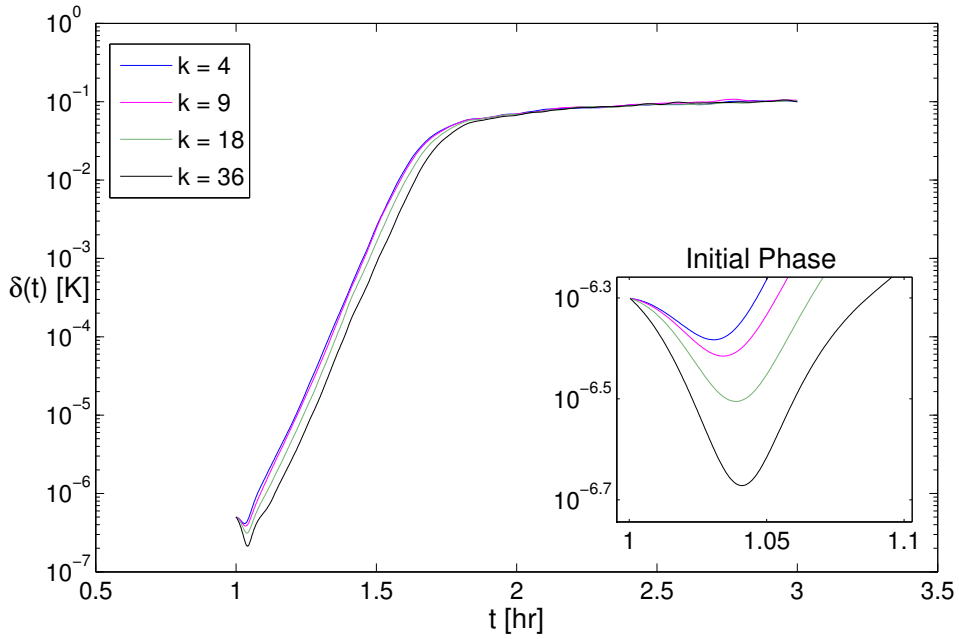

Figure 4.3: The error growth is shown for different values of k, where $\epsilon_0 = 10^{-6}$ for a domain discretized to $288 \times 288 \times 192$ points. The error growth is seen to be independent of the wavenumber, and attains to a constant exponent after a brief initial phase.

at different locations in the ABL is investigated.

4.2 The Effect of Perturbation Height

The vertical profile of variance in potential temperature (ref Figure 3.6) shows strong zones of error production at the surface and the inversion, while the mixed layer is a zone of turbulent transport. The ABL is perturbed at different locations by introducing planar perturbations ($k = 18$, $\epsilon_0 = 10^{-6}$) at different heights corresponding to $z_p \in \{20, 500, 1000\}$ m.

The evolution of the RMS error growth, upto the attainment of the constant exponent, is shown in Figure 4.4. The initial behavior of the three cases is markedly different, although the error propagates in a similar fashion after the transient period. The first case ($z_p = 20$ m) is the fastest to acquire the constant exponent indicating that surface region dominates the onset of the error production. The third case ($z_p = 1000$ m), where the perturbation is added within the inversion layer, takes the longest to attain its characteristic Λ. In this case the error does not reduce in the beginning as much as it does for the other two cases, which could be alluded to the fact that the inversion layer is a constant variance production zone as well. This is further seen from the immediate growth of error in this case which seems to follow from a weaker exponential rate set by the inversion, until it reaches the surface and the characteristic Λ dominates production. The plane introduced in the middle of the boundary layer ($z_p = 500$ m) shows the maximum drop in error for the initial phase, which is because this region has no production of variance, and turbulent transport carries the error to the production zones (both above and below), whence the error growth ensues. Visualizing the fields shows that the characteristic Λ growth is achieved only after the error is transported to the surface, where it is constantly produced and carried forward by the smallest scales as shall be described

shortly.

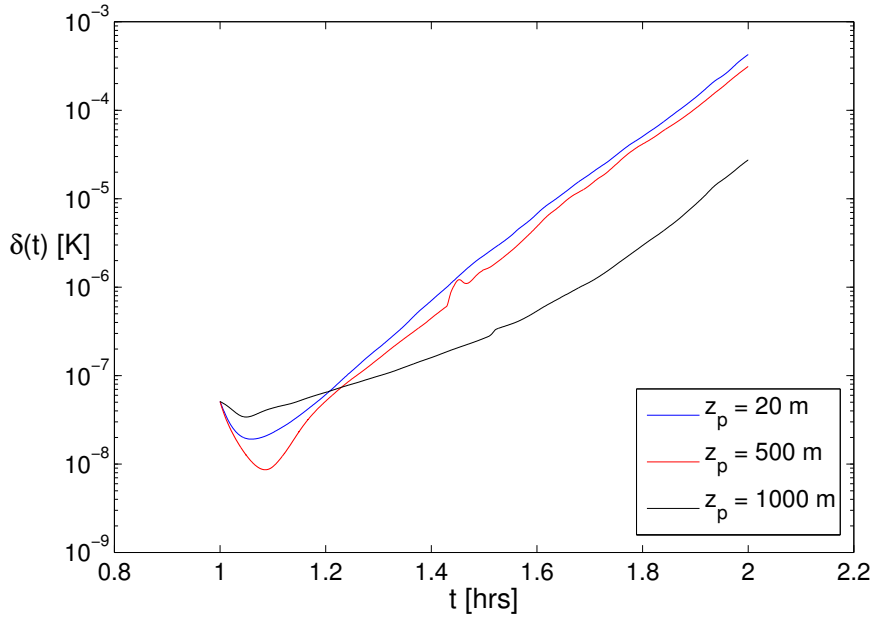

Figure 4.4: The evolution of planar perturbations introduced at different heights within the ABL. The fastest case to acquire the characteristic exponential growth is $z_p = 20$ m, suggesting the surface to be the main production zone for the error.

4.3 Integrated Error Profiles and Error Production Zones

The variance production zones in the potential temperature field are also intimately associated to the production of error. To ascertain the vertical distribution of error during the evolution of the perturbation field, horizontally integrated error profiles are generated from the vertical slice of the error for these three cases. This is done by first integrating an error slice at time t in the x direction, followed by normalization by the total error in that slice. This gives the integrated profile at each time instance which shows the *fraction* of the total error that is present at each z level. These profiles are shown in Figure 4.5, where the x axis now represents time, and the y axis shows the height. The panels on the right show the further time-averaged profile, which is simply the mean of the vertical profiles shown on the left panels over the entire simulation.

It is evident that the inversion layer and the surface layer are strong sources of error, while the mixed layer in between is a region of error transport (evident from the case of $z_p = 500m$, where the error is transported to the top and bottom, from where it is then produced and grows). Further, the global averages of error on the right panel closely resemble the vertical profile of variance production in the potential temperature, as was seen in Figure 3.6.

4.3.1 Power Spectrum Octaves

The evolution of octaves of the error energy spectrum shows the contribution of different scales in carrying the error energy, independent of each other. This is done by combining the energy contained in wavenumbers corresponding to a each octave, representing a range of scales. For instance the first four octaves include wavenumber ranges of $1,\ 2,\ (3-4)\&\ (5-8)$, and in

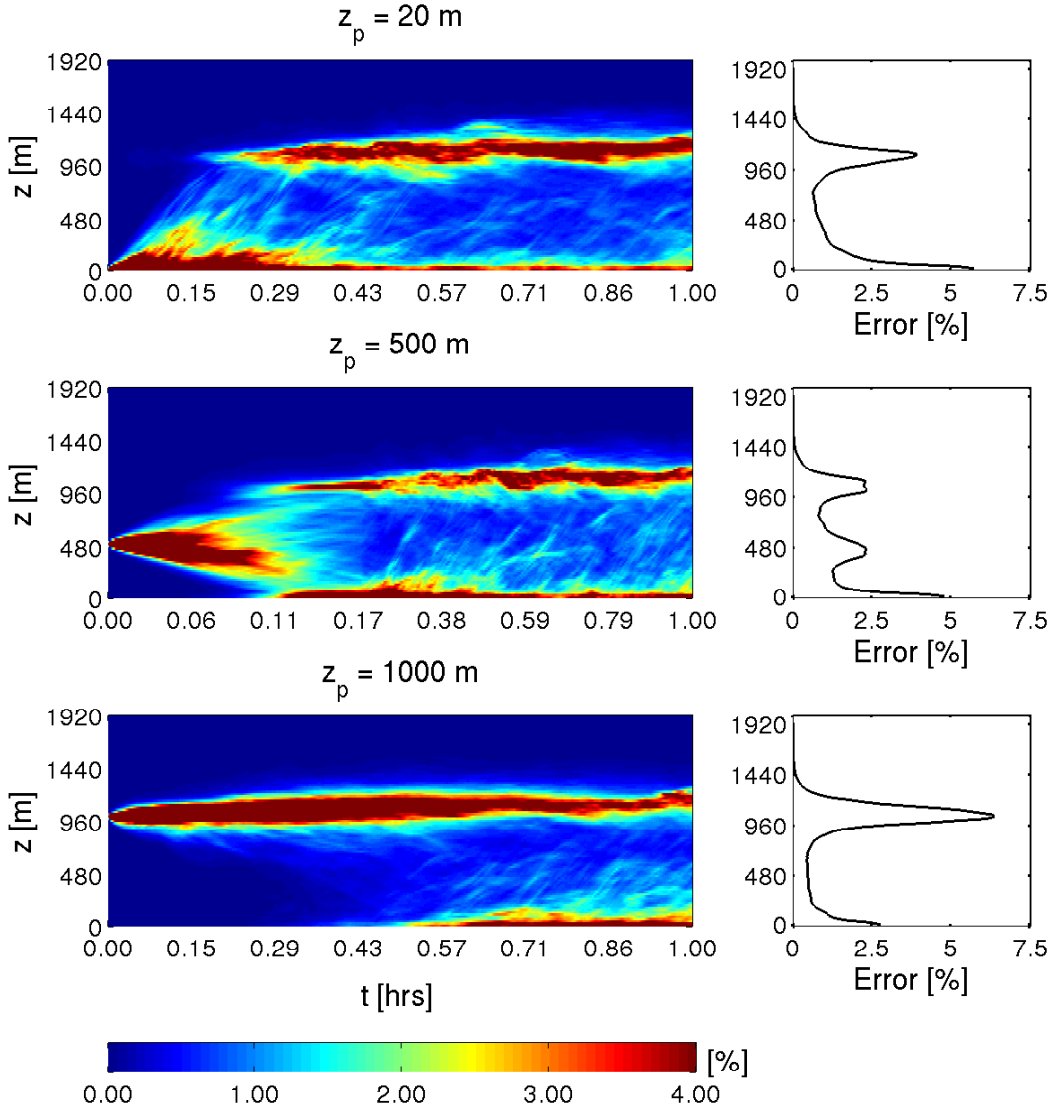

Figure 4.5: Horizontally integrated error profiles, for perturbations introduced at different heights in the boundary layer, show the evolution of the vertical distribution of error concentration. The inversion layer and the surface layer are seen to be strong zones of production of error, and the time-averaged integrated error profiles on the right panel show a close correspondence to the vertical temperature variance profiles (ref Figure 3.6).

general the n^{th} octave is given as

$$E_{\text{oct}}(n) = \sum_{k\,=\,2^{(n-2)}+1}^{2^{(n-1)}} E_k(t) \tag{4.1}$$

The octave evolution is shown in Figure 4.6 for the three different cases which were presented in Section 4.2. It becomes evident now that the smallest scales of the system (the last two octaves, i.e $k = 33 - 64$, and $k = 65 - 72$) carry the maximum error energy, which is seen to dominate the contribution to the total error. This shows the "redistribution" of the error energy as was suspected from the results of comparison of different wavenumbers in Section 4.1. Contrary to

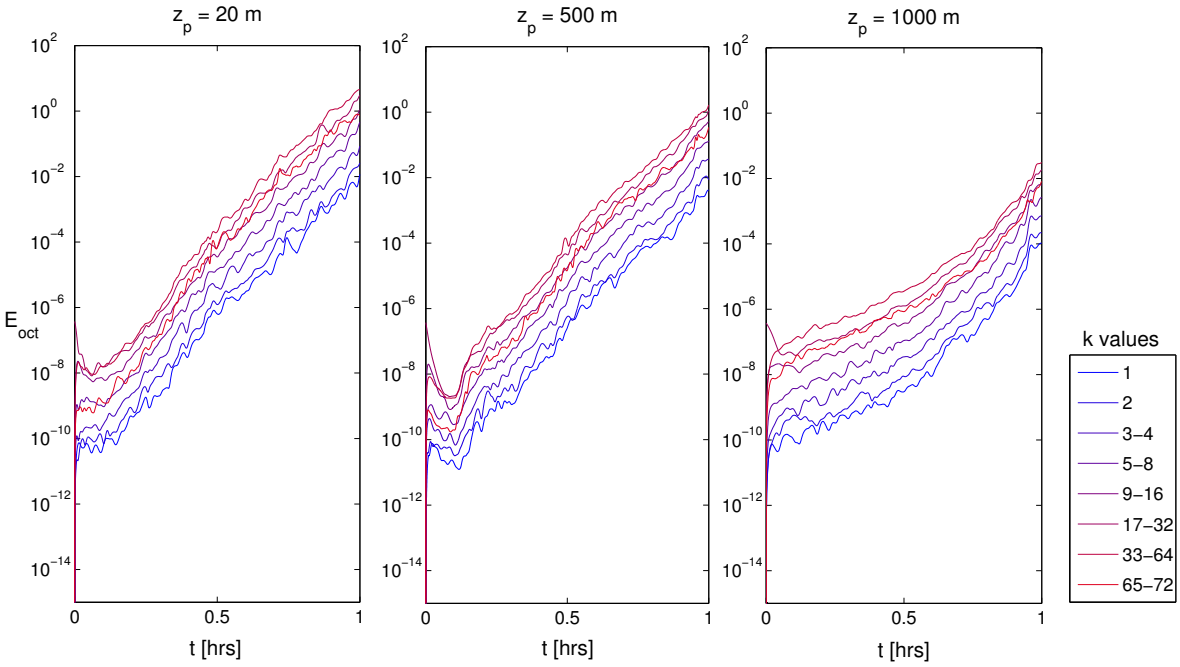

Figure 4.6: Comparison of the evolution of power specrum octaves for planar perturbations introduced at different heights. The smallest scales (the red curves) are seen to dominate the propagation of error, whereas the larges scales (the blue curves) carry a smaller portion of the total error. The various scales are seen to propagate at the same exponential rate, unlike the classical notion of saturation of error.

the classical notion of a faster growth of small scale errors, the different scales of the system attain the same growth rate in these simulations.

4.4 The Influence of Grid Resolution

The resolution of the LES determines the size of the grid boxes in the x, y and z directions, and is a choice often based upon factors like the aspect ration of the boxes and available computational power. A larger number of grid boxes (higher resolution) amounts to more resolved turbulence. The LES Reynolds number as given by 3.19 can be recalled as

$$Re \sim \left(\frac{z_i}{\Delta}\right)^{4/3}$$

where z_i is the inversion layer height and $\Delta = \sqrt[3]{\Delta x \Delta y \Delta z}$ relates to the size of the grid boxes. The effect of resolution on the growth of error can be crucial, and is studied for different cases by successively doubling the number of points in the horizontal direction i.e. $N_{x,y} \in \{36, 72, 144, 288, 576\}$. A fixed aspect ration of the boxes ($\Delta x/\Delta z = 1.25$) is maintained by varying the number of points in the z direction to $N_z \in \{24, 48, 96, 192, 384\}$. A volumetric perturbation ($k = 4, \epsilon_0 = 10^{-6}$ K) is introduced after a seeding time of 1 hr. The RMS error growth along with the best exponential fit for each case is shown in Figure 4.7.

It is immediately apparent that the effect of increasing the resolution is profound, as the rate of error propagation increases without signs of saturation. Upon increasing the total number of grid points by a factor of 8 (due to resolution doubling in x, y and z), the Lyapunov exponent is seen to almost double as well. A higher resolution simulation has a higher Reynolds

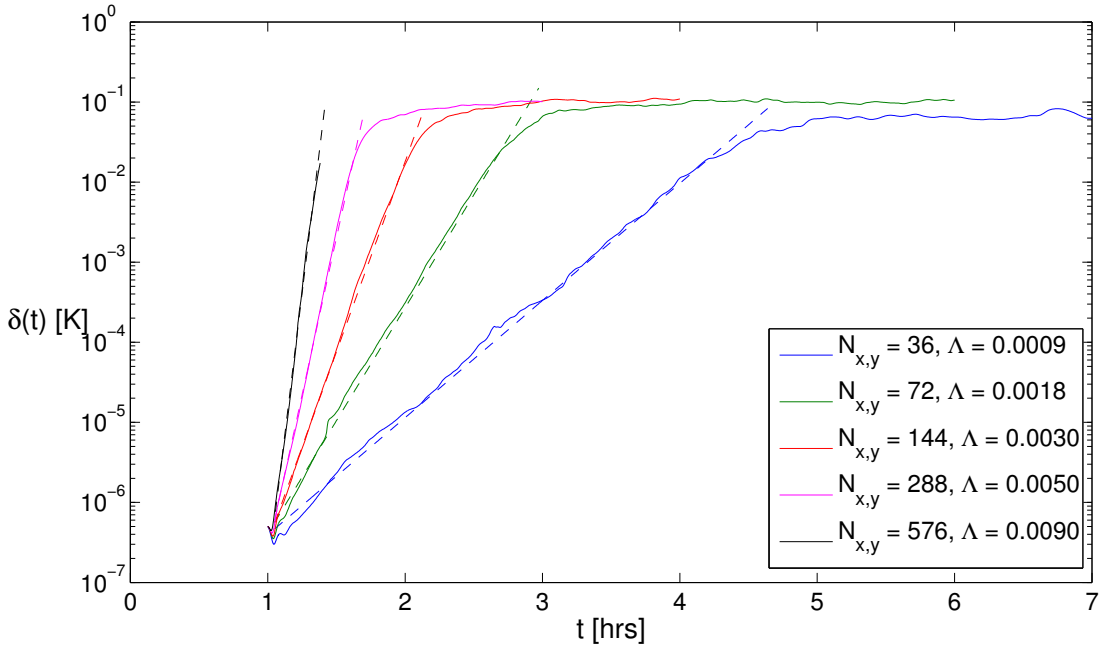

Figure 4.7: The effect of varying the resolution of the domain on the error growth is shown. A higher resolution simulation has a higher effective Reynolds number, increasing the rate of error propagation without signs of saturation.

number, which represents more resolved turbulence. Finer scales (higher wavenumbers) become increasingly available for the faster propagation of error. This is seen in Figure 4.8 which shows horizontally integrated error profiles, where increasing the Reynolds number allows finer structures to be resolved, which in turn govern the growth of error (with the white band marking the approximate time of error saturation).

This is further investigated in the power spectrum analysis of the error field, which shall cast to light the sovereign modes of error growth.

4.4.1 Average Power Spectra During Error Growth

The average power spectrum is calculated for the growth phase of the error, which is marked between the two points on each RMS error curve on the left panel of Figure 4.9. It is seen that the error is concentrated in the higher wavenumbers, and the power spectrum shifts to the right as the resolution becomes finer and smaller scales are increasingly resolved. The power spectrum retains this self similar shape throughout the growth phase (not shown here), and smaller scales are not seen to saturate at a faster rate, again discordant to the general notion of error growth in systems with multiple scales.

4.4.2 Dimensionless $\Lambda t_\star$ as a Function of Re_l

The exponent Λ has units of $[s^{-1}]$, and can be non-dimensionalized by multiplying it with $t_\star$, the large eddy turnover timescale calculated as $t_\star = z_i/w_\star$. Figure 4.10 shows $\Lambda t_\star$ as a function of the LES Reynolds number Re_l calculated using Eq. 3.19 for the different grid resolutions.

Over a single large eddy turnover timescale, the error is seen to increase almost linearly with Re_l. For $Re_l \sim 10^3$, the amplification of an initial error (calculated as $e^{\Lambda t_\star}$) is already $\sim 10^4$ times within a single $t_\star$. Further, the curve shows no apparent signs of saturation, and

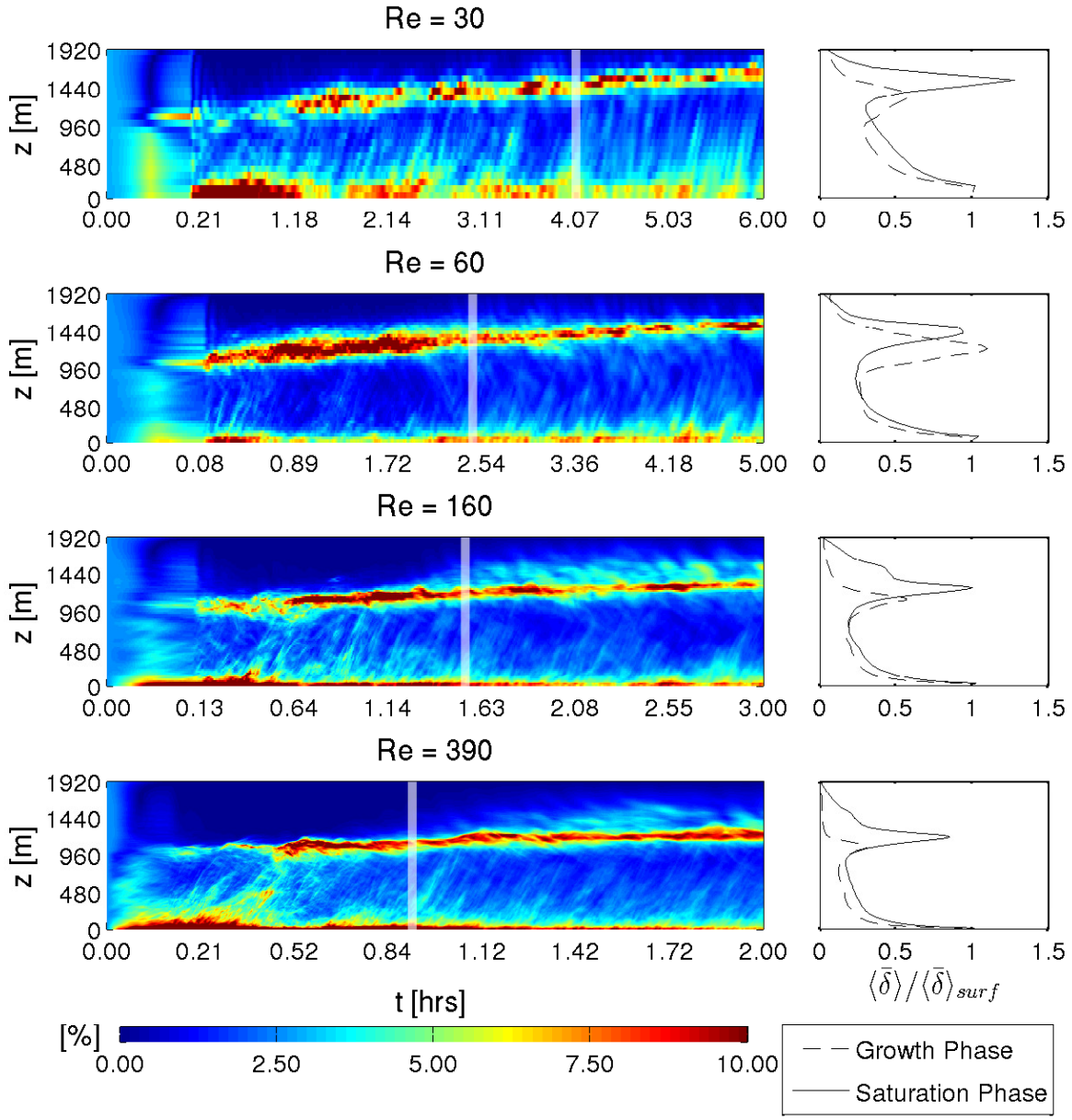

Figure 4.8: Integrated error profiles for different resolution LES cases (normalized and scaled for visualization). The white lines mark the time of error saturation. Increasing the resolution adds finer features to the error profiles which represent smaller scales.

if extrapolated to Reynolds numbers encountered in the atmosphere ($\sim 10^8$), would imply the saturation of an initial error, however small, within timescales of the smallest eddies. This has a dire implication on predictability, where on the one hand a finer resolution is often sought for a closer representation of the dynamics, which in turn is seen to render the system highly sensitive to perturbations, greatly shortening the yardstick of predictability.

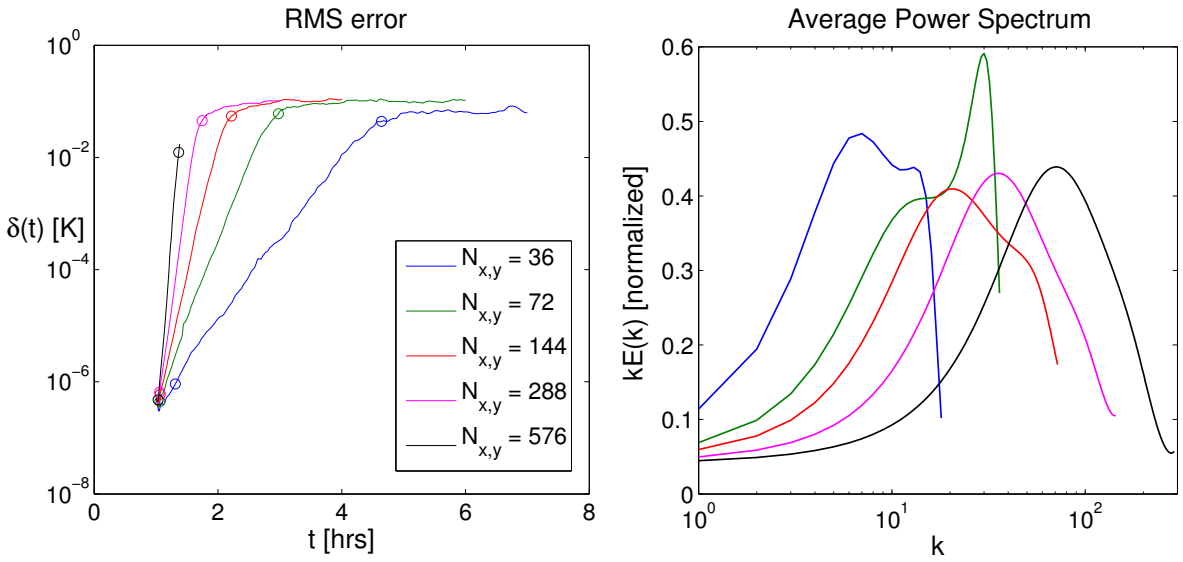

Figure 4.9: The average power spectra during the error growth phase (marked by the two points on each RMS error curve on the left) is shown. The spectrum is increasingly dominated by the smaller scales (higher wavenumbers) as they become available for a higher resolution simulation, which also resolves finer scales of turbulence.

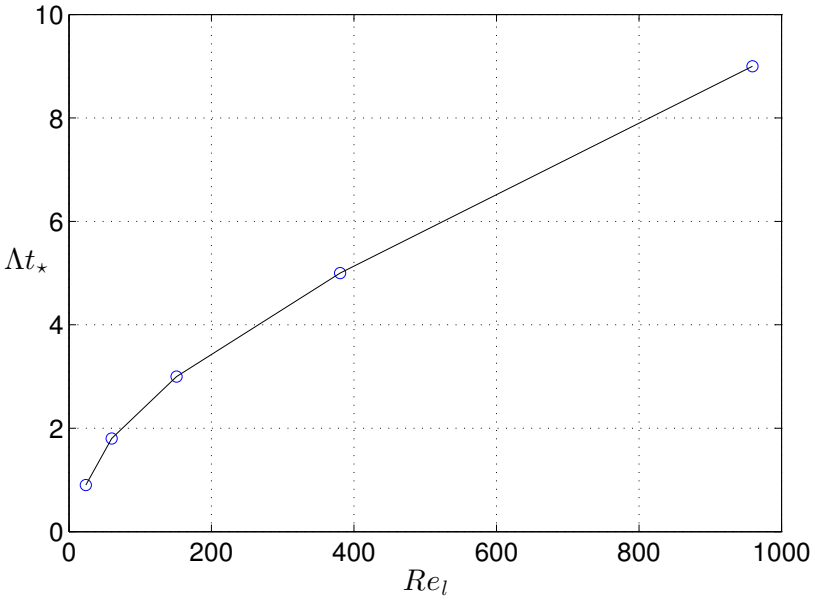

Figure 4.10: The dependence of $\Lambda t_\star$ on the LES Reynolds number Re_l calculated using Eq. 3.19 shows that Λ grows consistently with Re_l, without any signs of subsequent saturation. For $Re_l \sim 1000$, $\Lambda t_\star \sim 9$, which makes $e^{\Lambda t_\star} \sim 10^4$ which means that an initial error of magnitude 10^{-6} saturates in slightly more time than the large eddy turnover timescale.

4.5 The Recurring Motif of Turbulence

The results from the LES study affirm the dominance of the higher wavenumbers in the error energy spectrum. After the error saturates, its spectrum re-configures to the turbulence energy spectrum, resembling a physical field variable. This follows from the two simulations becoming uncorrelated, and is indeed observed in Figure 4.11. The average error energy spectrum for an LES with $144 \times 144 \times 96$ grid points is shown for the growth phase (in red) and saturated phase (in blue). The spectrum of the potential temperature field itself (broken black curve) is also shown. During the growth phase, the error energy spectrum is largely dominated by the higher wavenumbers, but upon saturation the smaller wavenumbers contain more energy, and the spectrum begins to resemble the self-similar turbulence energy spectrum which is observed for the θ field.

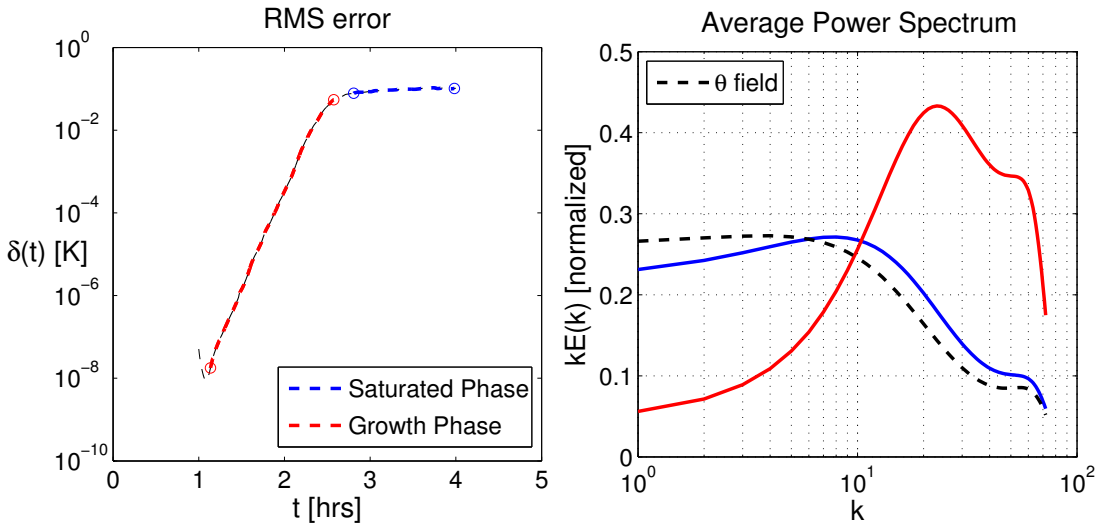

Figure 4.11: The error energy spectrum is seen to re-configure to the turbulence energy spectrum upon saturation. During the growth phase (shown in red), the higher wavenumbers dominate, but after saturation (shown in blue), the larger scales take over the energy distribution, resembling the power spectrum of the θ field.

The LES resolves turbulence appreciably, although there are caveats. First, different regions of the flow are modeled with a different eddy viscosity, making it difficult to interpret the properties of the fluid. Secondly, the Reynolds number of the flow is completely dependent on the resolution. To address these two issues, this research now focuses on DNS, where the fluid viscosity (and hence the Reynolds number) is independent of the grid resolution.

CHAPTER 5

Direct Numerical Simulations

The nature of error propagation in the LES is seen to maintain a strong indifference to several parameters that were examined, including different wavenumber regimes for introducing the perturbation, the location in the PBL or the type of perturbation (i.e. across the 3D volume or in a 2D plane). The error is seen to soon adjust to its governing mode and spectrum of propagation, determined by the Reynolds number of the flow (which was given by Eq. 3.19). As turbulence is increasingly resolved with finer resolution, the larger wavenumbers become successively available for carrying the error energy. Although the small eddies carry a small part of the energy individually, these are numerous, and their cumulative effect results in a faster propagation of error. This is seen from the linearly increasing $\Lambda t_\star$ over Re_l (refer Figure 4.10).

To decouple the effect of resolution dependence and Reynolds number on the error growth, DALES is run in a *DNS* setting. This enables control on the Reynolds number of the flow, which can be made constant by fixing the *viscosity* while the resolution is varied independently (see Section 3.6 for an overview of the setup).

5.1 Resolution Independence of Error Growth

The first factor that is investigated is the effect of changing the resolution of the simulation on the growth of the RMS error. For a fixed viscosity of $\nu = 10$ ($Re \sim 120$), two simulations are performed with identical initial conditions, with a planar perturbation at the middle of the boundary layer ($z_p = 480$ m), where the resolution of the second simulation is twice that of the first in each of the three directions. The growth of the RMS error is shown in Figure 5.1, where after the initial phase, the constant exponential growth sets in and both the simulations are seen to have an identical exponent. The doubling of the resolution, as opposed to the case of the LES, does not effect the flow anymore. This shows that by fixing the eddy viscosity, the effect of changing the resolution can be eliminated, and the flow characteristics can be independently varied to study the propagation of error.

5.2 The Effect of Perturbation Wavenumber

Similar to the LES study, the effect of perturbing different wavenumbers is studied. This is done for a simulation over a domain of $576 \times 576 \times 192$ points in the x, y and z directions with a

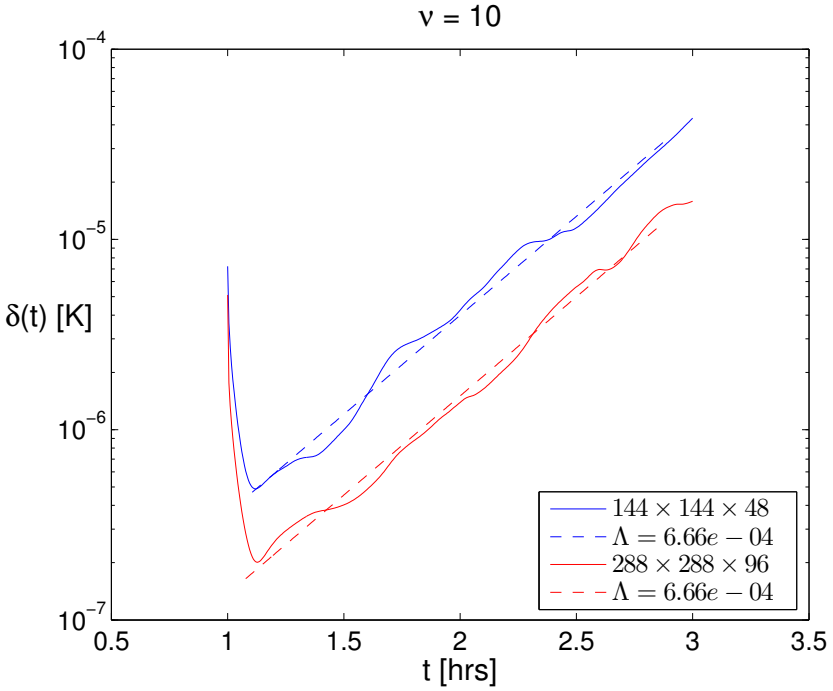

Figure 5.1: Growth of the RMS error for two simulations with the same Reynolds number ($\sim$ 120), shows that doubling the resolution has no effect on the *Lyapunov exponent* in the constant exponential growth phase of the error. This shows that by fixing the Eddy Viscosity the growth of error can be made independent of resolution.

fixed eddy viscosity $\nu = 1.6$. The perturbation has a magnitude of $\epsilon_0 = 10^{-6}$ and is introduced at a plane in the middle of the boundary layer at $z = 480$ m. Figure 5.2 shows that the initial drop in error increases for a higher wavenumber perturbation, but soon the same constant exponent $\Lambda = 0.0022$ is attained with which the error propagates upto saturation. Again, an independence of the perturbation wavenumber is observed, and after a rapid redistribution of the error energy, the governing modes of error growth dominate.

5.3 The Effect of Perturbation Height

As was done for the LES in Section 4.2, planar perturbations (with $k = 9$) are introduced at different heights in the boundary layer. The RMS error growth is shown in Figure 5.3, where now the largest initial drop in error is seen for the perturbation added at a height near the inversion ($z_p = 952$ m), whereas the fastest to acquire the constant exponential growth is the perturbation near the surface, which was also seen for the LES (ref Figure 4.4). This behaviour can be further understood from the integrated vertical error profiles for the three cases, seen in Figure 5.4. The inversion is not a dominant error production region, unlike the LES, and the main source of error is the surface region. This is probably due to the artificial construction of the "inversion". Hence, the production of error at a constant rate is attained *after* the error is advected to the surface, which is seen from the profiles for $z_p = 480, 952$ m. The panels on the right show the time-averaged integrated profile of error concentration in the vertical direction, which closely resembles the variance profile of θ as was shown in Figure 3.7.

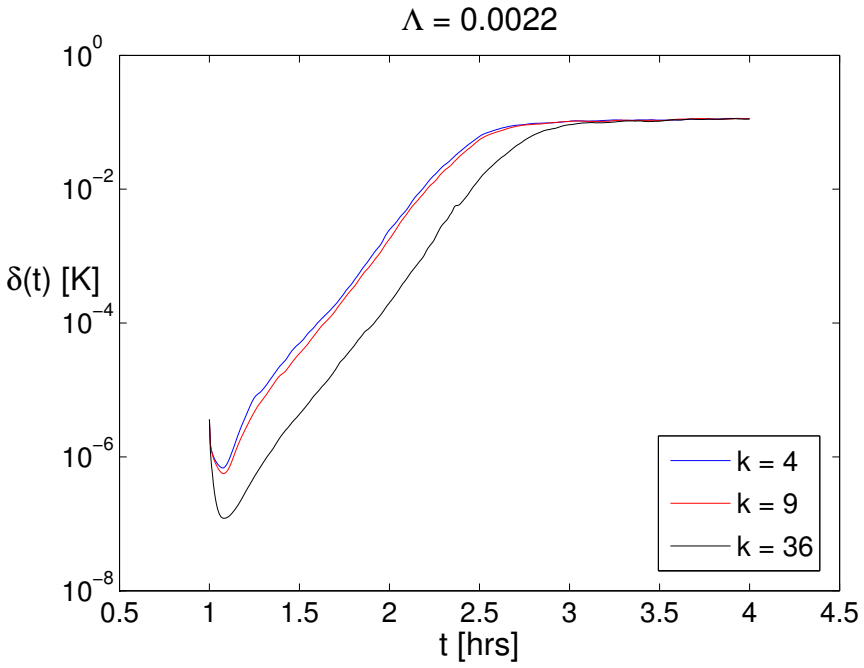

Figure 5.2: The dependence of error propagation in the DNS on the wavenumber of the initial perturbation field is shown. After an initial phase of redistribution, the error is seen to propagate at the constant exponent determined by the flow itself ($\Lambda = 0.0022$), which is a behaviour consistent with the LES results (ref Figure 4.3).

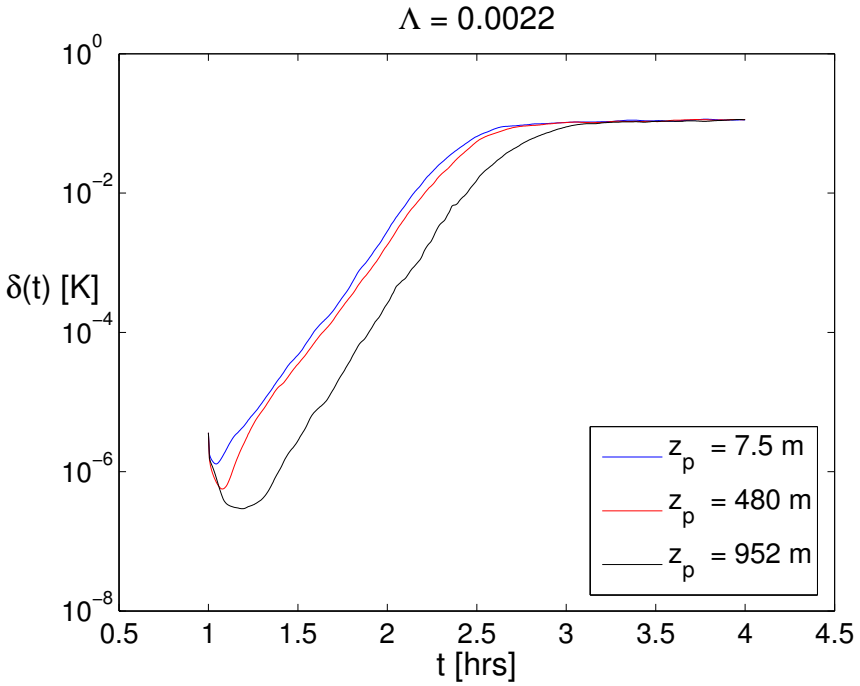

Figure 5.3: Error propagation for perturbations introduced at different heights in the boundary layer is shown. The last one to attain constant exponent is the case where the error is introduced near z_i, which shows that the error production starts at the surface after the field is advected downward.

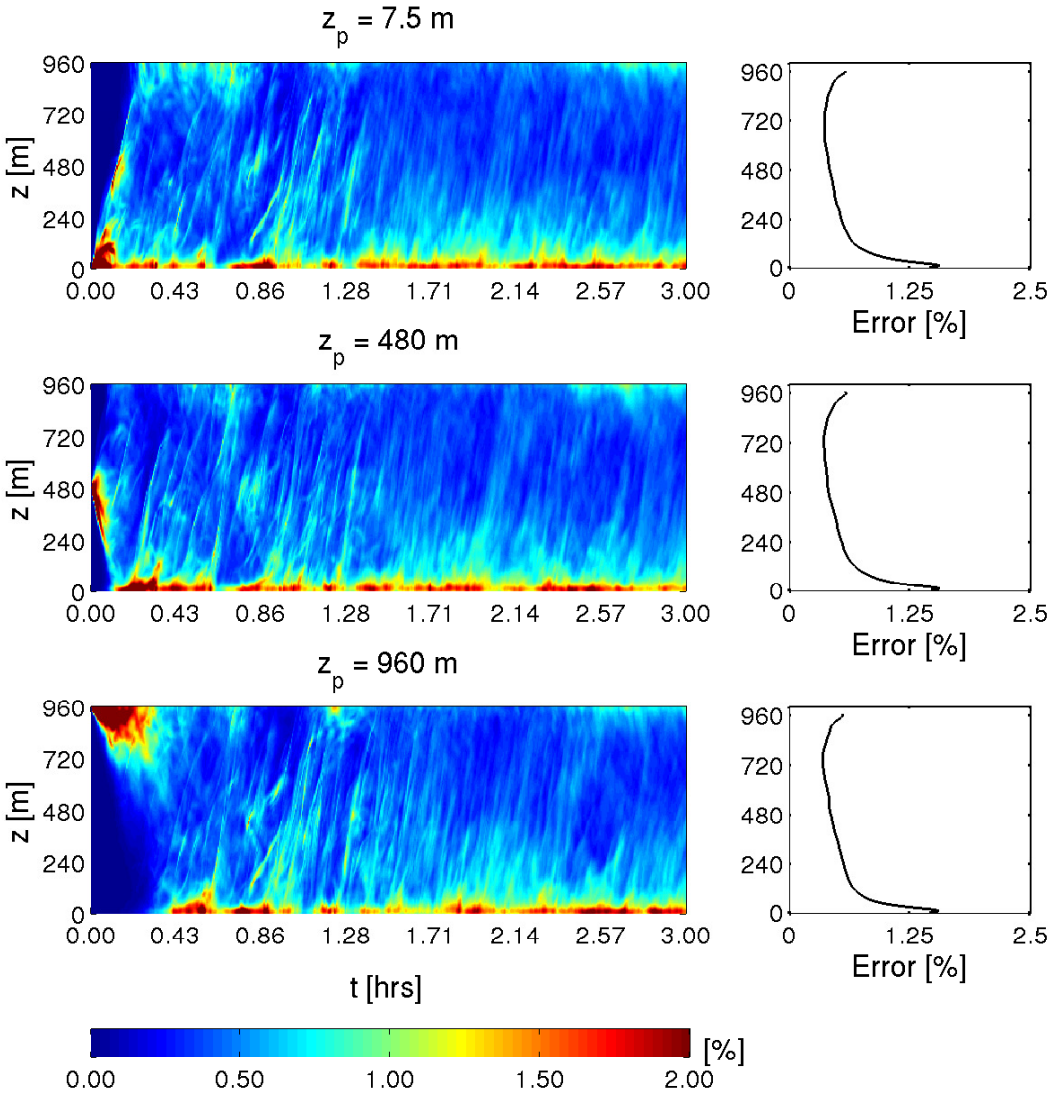

Figure 5.4: Horizontally integrated error profiles (normalized and re-scaled for visualization) for perturbations introduced at different heights in the boundary layer for the DNS simulations. The surface layer is here seen to be region of error production, and the time-averaged integrated error profiles on the right panel show a close correspondence to the vertical temperature variance profiles (ref Figure 3.7).

5.4 Reynolds Number Dependence of the Error Growth

By changing the eddy viscosity, the Reynolds number of the flow is varied to construct various cases. The domain is discretized to $288 \times 288 \times 96$ points in the x, y and z (except for the simulation with $\nu = 1.6$, where the resolution is increased to $576 \times 576 \times 192$), and the growth of the RMS error is shown in Figure 5.5. The rate of error growth is seen to increase sharply for the lower viscosity (higher Reynolds number) simulations. This result is comparable to the LES study (refer Figure 4.7) where changing the resolution increased the Lyapunov exponent, which was an aftermath of the increase in the effective flow Reynolds number

The Λ calculated from the best exponential fits to the growth phase of the error is normalized

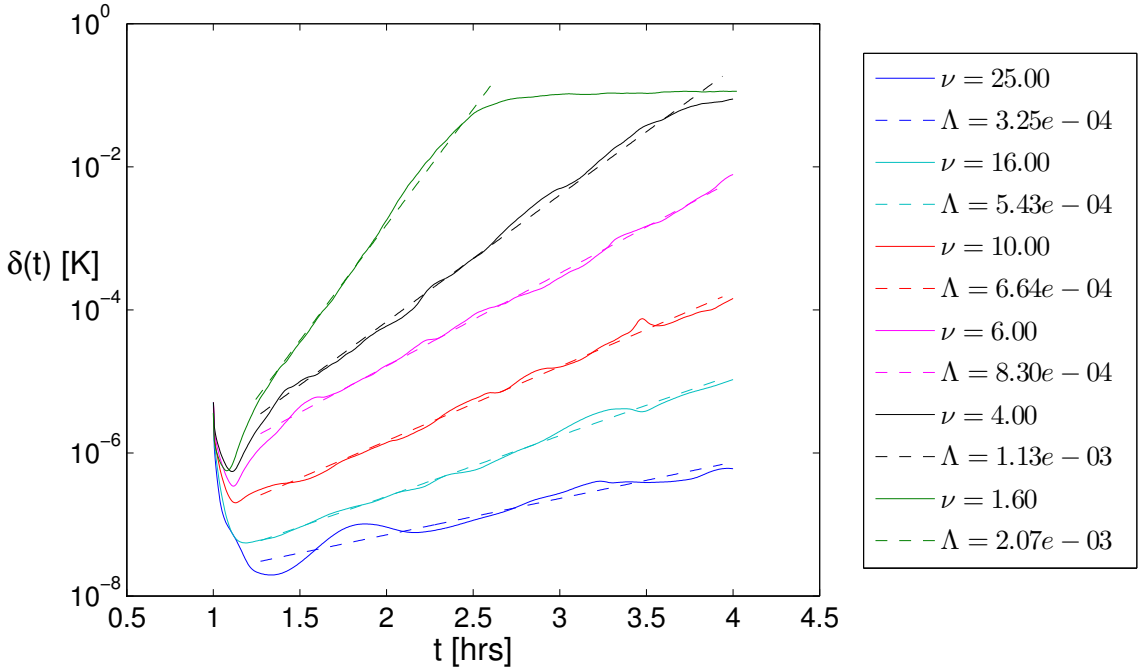

Figure 5.5: The effect of increasing the flow Reynolds number by varying the viscosity is shown. The rate of propagation again increases for more turbulent flows.

by $t_\star$ and shown in Figure 5.6 as a function of the Reynolds number calculated using Eq. 3.20.

The dimensionless $\Lambda t_\star$ increases linearly with the Reynolds number, similar to what was seen for the LES study. Its magnitude, for a comparable Reynolds number in the LES, is seen to be smaller. This stems from the fact that there is a singular variance production zone (the surface) in the DNS, as opposed to two strong zones in the LES (the surface and the inversion layer). Again, the rate of error propagation does not show any signs of saturation as the Reynolds number increases. This is further investigated in the later sections.

5.4.1 Average Power Spectrum During Error Growth

The average (normalized) power spectrum during the growth phase of error (calculated between the points marked on each RMS error curve in the left panel) for the different Reynolds number cases is shown in Figure 5.7. It is seen that the spectrum shifts more to the right, i.e. the higher wavenumbers contain more energy as the Reynolds number of the flow increases. The error energy in the larger scales of motion (of the order of the largest eddies, corresponding to around $k \sim 3-5$) reduces for the higher Reynolds numbers.

5.4.2 Evolution of the Power Spectrum Octaves

Evolution of the octaves of the error energy spectrum is shown for the higher resolution simulation ($576 \times 576 \times 192$) with $\nu = 1.6$, in Figure 5.8. It is evident that the different scales again attain the same Λ, in contrast to the accepted notion on error propagation. Further, the higher wavenumbers carry most of the error energy during the growth phase ($k \sim 32-128$). Although, unlike the LES, this maximum energy containing range of wavenumbers corresponds

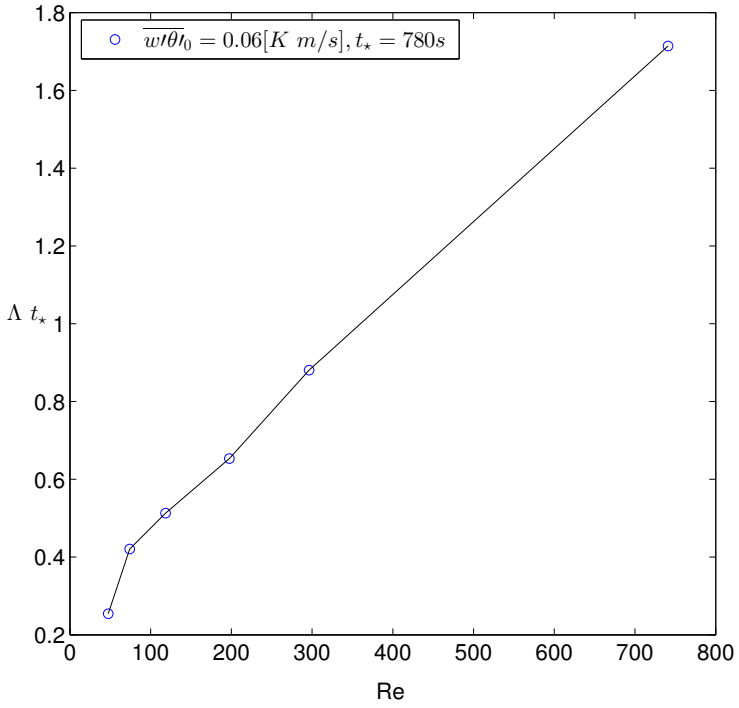

Figure 5.6: The Lyapunov exponent normalized with $t_\star$ is plotted against the Reynolds number (given by Eq. 3.20). An increase in the Reynolds number causes a linear increase in $\Lambda t_\star$ which represents the growth in error over a single large eddy turnover timescale.

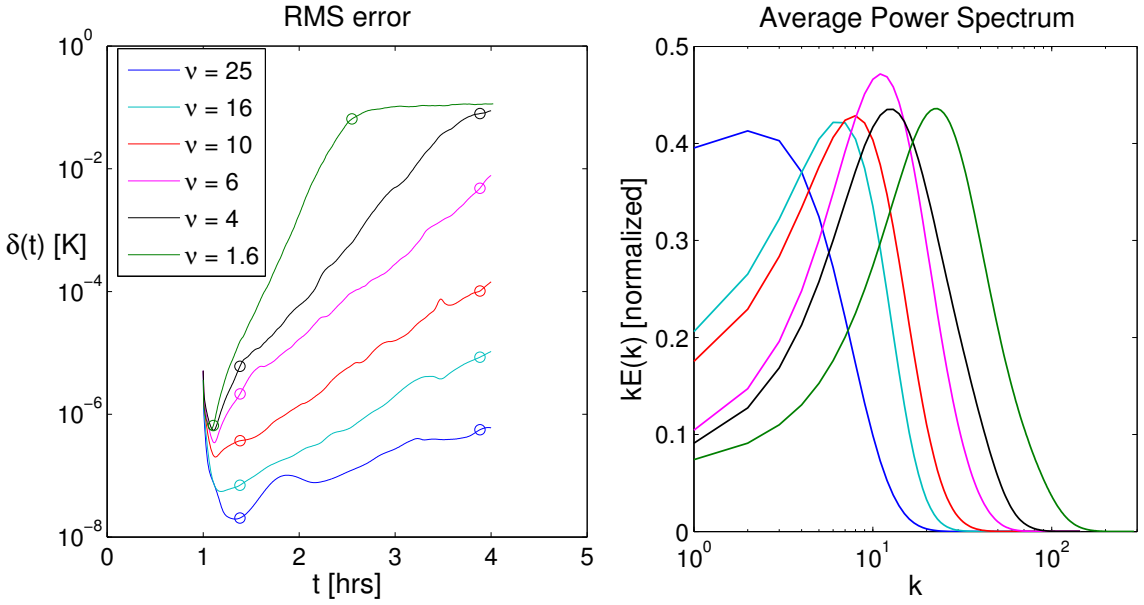

Figure 5.7: The average normalized power spectrum during the growth phase of error (marked for each case by the two points on the RMS error growth curve) for different Reynolds numbers is shown. As the Reynolds number increases, more of the energy is seen to reside in the higher wavenumbers, and the power spectrum shift successively to the right, with a drop in the contribution from the lower wavenumbers.

to a smaller octave.

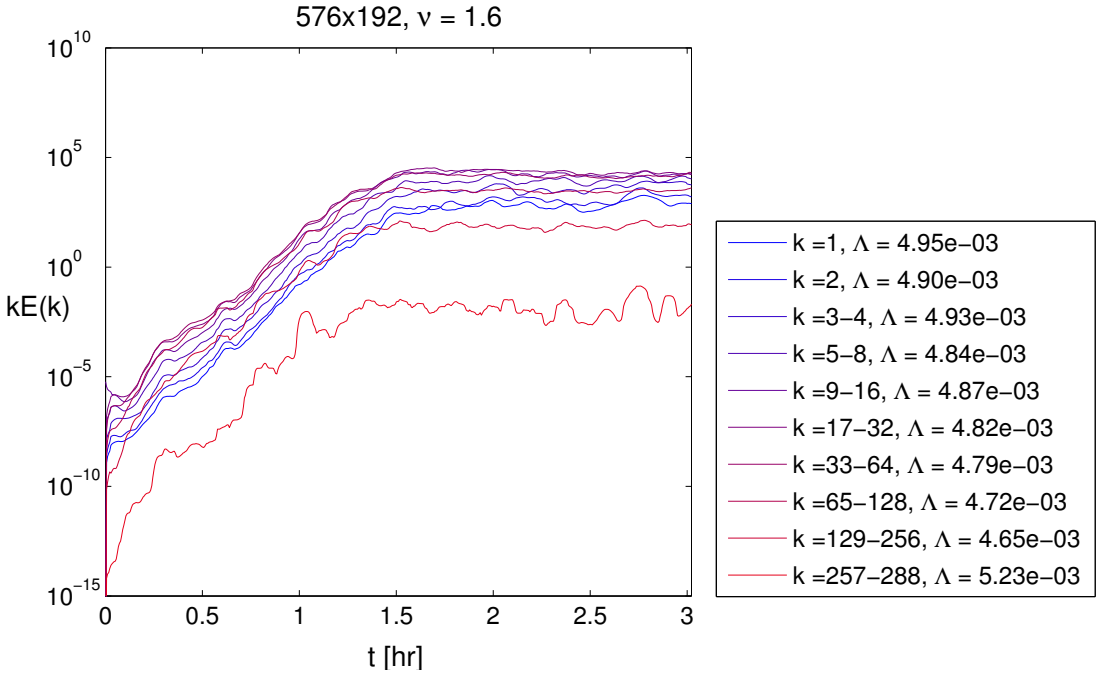

Figure 5.8: The evolution of the power spectrum octaves shows that the error propagates with a comparably similar Lyapunov exponent for all the range of scales. The smaller scales are not seen to have a faster rate than the larger scales.

5.5 Effect of Changing Larger Scales of Motion

The kinetic (and error) energy spectrum, in its frequency domain, is known to peak at a timescale roughly corresponding to $t_\star$. This means that the largest amount of energy is contained in scales of motion which have a lifetime that scales with $t_\star$. Further, $1/\Lambda$ can also be interpreted as an *e-folding* timescale (τ [s]) of error growth (or the time taken for the error to amplify by a factor of e). In the simulations performed, $\tau \sim 10^3$ for the higher resolution cases, wherein $\tau > t_\star$. Hence, in the frequency domain, τ would have a smaller frequency than $t_\star$, such that the timescale over which a single e-folding occurs is longer than the timescale of the largest eddies. It is interesting to investigate whether the error propagation rate saturates as $\tau \to t_\star$. This can be attempted in two ways. First would be to simply increase the Reynolds number (by further reducing the viscosity), and doubling the resolution, which would move τ towards $t_\star$. But such a simulation would be very expensive. The other method would be to rather vary the dynamics of the flow itself, by modifying the fluxes and governing parameters such that $t_\star$ is modified. This is done by reducing the surface flux by a factor of 8 ($\overline{w'\theta'}_0 = 0.0075$ K m/s), which in turn halves the convective velocity scale $w_\star$ calculated using Eq. 3.11, doubling the value of $t_\star$, which brings it to a smaller frequency. As such, the Reynolds number for the flow can be maintained at the same value by further reducing the Eddy Viscosity for each corresponding case presented in Section 5.4, by a factor of 2. How such a change in the flow shall effect the Lyapunov exponent and error growth is now studied, and Λ normalized by the *modified* $t_\star$ is shown in Figure 5.9 in comparison to the previous case.

It is remarkable to note that although the value of Λ corresponding to Re changes with a

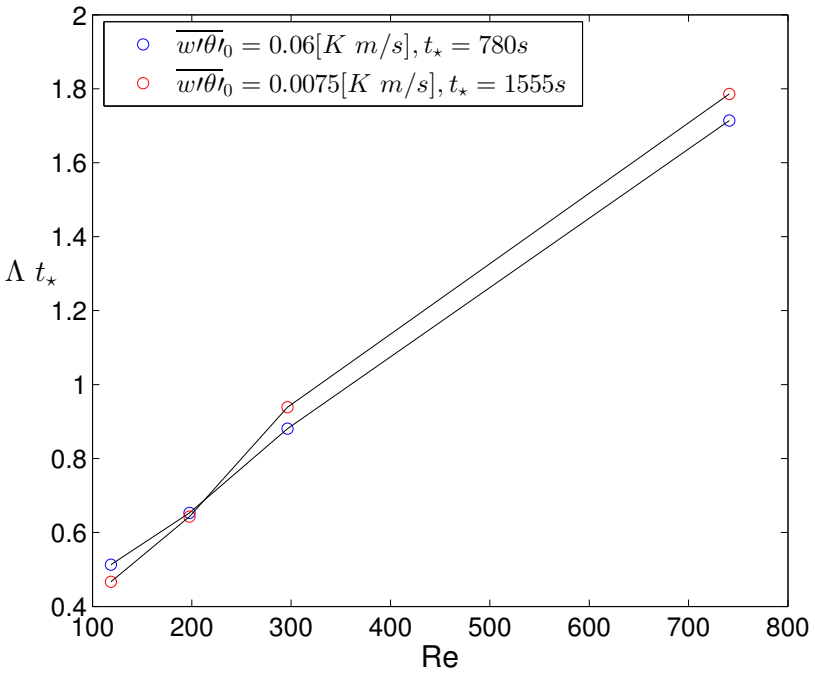

Figure 5.9: Λ normalized by $t_\star$ is seen to be solely dependent on the Reynolds number of the flow. The pair linearly increases with Reynolds number without signs of saturation.

change in the system dynamics, its allied effect upon normalization with $t_\star$ remains unmoved. This establishes the $t_\star$ in the relation $\Lambda t_\star \sim Re$, and the rate of error growth Λ manifests from the combined effect of the Reynolds number and the convective velocity timescale.

Extrapolating to Reynolds numbers definitive of physical atmospheric flows again suggests, not only the amplification of initial errors of any magnitude, but also their immediate saturation to the scales of the system. The mechanism of such a rapid growth of initial errors is still not understood, and calls for further investigation. This proposition casts predictability in LES and DNS to strong constraints of the flow Reynolds number.

CHAPTER 6

Conclusions

This work dealt with the predictability of atmospheric flows. First, the process of forecasting using data assimilation was performed on the Lorenz [1963] model. Several DA methods of increasing complexity were tested, including the varying of fixed scalar weights, ensemble spread based predictions, further leading to multivariate analysis. This provided a first cursory understanding of the propagation of error in a chaotic dynamical system, and its implications on predictability. Steering to a more realistic setup, the second part of this study explored the propagation of perturbations in a turbulent flow. As Large Eddy Simulations and Direct Numerical Simulations are the most applied computational techniques to resolve turbulence, the Dutch Atmospheric Large Eddy Simulation (DALES 3.1 [Heus et al., 2010]) was adapted to study error propagation in simulations of a dry convective boundary layer capped by a weak inversion (modeled after the $W06$ specifics from Sullivan et al. [1998]) over a domain of $3600 \times 3600 \times 1920$ m^3. Following which, various experiments were conducted to assess the sensitivity of error growth to different perturbation characteristics, including power spectrum analysis to find the dominant modes of error growth. The conclusions of these studies are now presented.

6.1 Forecasting in the Lorenz Model

The Lorenz Model is marked by an extreme sensitivity to initial conditions, with an exponential growth of initial errors upto saturation, which is characterized by its Lyapunov exponent $\Lambda = 0.904$. This feature is observed for varied dynamical processes relevant to the atmosphere, and it manifests as a barrier to predictability, deprecating the quality of purely observation based forecasts. The process of data assimilation (DA), combining model predictions with observations improves the quality of forecasts. A first simple DA based forecast is done by varying a fixed scalar weight, the value of which decides the fractional contribution of the model in initiating the next forecast cycle. It shows the existence of an optimal weight which yields smaller error in forecasting than does a purely observation based forecast. The value of this weight is seen to be inversely related to the duration of the measurement interval T for forecasting, where a larger T causes the system to diverge more, yielding a small w (~ 0). This method is surpassed by ensemble spread based forecasting, which accounts for the quality of model predictions based upon local sensitivity of the attractor evaluated with ensemble spreads. A further improvement in forecasting over the maximum energy containing range of $T = 0.1 - 2$ is then observed with

the multivariate analysis which accounts for the model quality separately for each variable, and also their mutual influences. This method even extends to forecasting when the observations available are incomplete.

6.2 Large Eddy Simulations

The LES study starts with examining the evolution of perturbations in a turbulent atmospheric boundary layer. An initial error is seen to exponentially grow to saturation, reminiscent of the Lorenz model. A characteristic Lyapunov exponent Λ can be associated to this constant growth phase of error. Remarkably this growth remains independent of the wavenumber k of the perturbation introduced, except for the brief initial phase when there is a dip in the error due to dissipation (which is more for a larger k). The power spectrum evolution shows a rapid redistribution of the error energy to a self similar shape within few minutes of seeding, which is dominated by the higher wavenumbers and maintains itself during the growth phase till saturation. Further, perturbing different locations of the boundary layer shows that the constant exponential growth dominates the error production after it is advected to the surface and the inversion, which represent the dominant variance production zones. The rate of error propagation (Λ) is seen to be independent of these parameters. It has a strong resolution dependence, and grows without signs of saturation as the resolution of the simulations is increased. This is alluded to the dominance of the higher wavenumbers in the power spectrum of the error, which become increasingly available upon resolving finer turbulent structures, as the resolution in LES directly relates to the Reynolds number. This effect is eliminated in the DNS studies.

6.3 Direct Numerical Simulations

Running DALES in a DNS setup eliminates the resolution dependence of the error growth, which is again seen to be independent of the wavenumber of the perturbation and its location in the boundary layer. The classical view on error propagation in atmospheric systems, where the smaller scales saturate faster, consequently triggering the larger scales upto complete loss in predictability [Lorenz, 1969; Leith and Kraichnan, 1972; Rotunno and Snyder, 2008] is not observed in these simulations. An octave analysis of the error energy spectrum shows that the different scales attain to the same Λ. The Reynolds number is now increased by reducing the viscosity, which directly reflects in an increase in the rate of error propagation. This effect again stems from the dominance of the higher wavenumbers in the error energy spectrum. Lastly, upon altering the dynamics of the system by changing the timescale of convective motions $t_\star$, it is seen that the dimensionless pair $\Lambda t_\star$ remains invariant and increases linearly with the Reynolds number (as was also seen for the LES). If this curve remains consistent, an extrapolation would imply that at Reynolds numbers encountered in the atmosphere ($\sim 10^8$), an initial error, however small, would grow to the scales of the system *within* the timescales of the smallest eddies.

6.4 Suggestions For Future Work

This study delves into an exciting avenue of research: predictability in resolved turbulence. The phenomenon of turbulence has been observed under the lens of physics and mathematics alike, and has eluded an exhaustive definition. However, it is now widely agreed upon to be a highly chaotic phenomena, the tune to which this research was set.

Some of the recommendations for future work, which could broaden the scope of these results are enlisted below.

- The characteristics of the initial phase of dissipation of error, and the brief transition to saturation can be further investigated. Their exact dependence on the wavenumber k, viscosity and height of the perturbation can be studied for a better understanding of the growth of the RMS error.
- The sources of error correspond to the surface and the inversion, and a further dominance of the higher wavenumbers in the growth of error is seen. The region near the surface consists of most of these small eddies. As the error reaches the surface, it rapidly modifies the structure of the smallest eddies in the surface due to a homogeneous surface flux, which in turn modify the larger scales. Similar studies as performed here would be beneficial in a setup where the larger scales of the system have a biased motion, arising from a heterogeneous surface. For instance, with the introduction of a fixed hot spot that drives convection, these large eddies can be made to originate at a specific location. This should be expected to inhibit the uncontrolled growth of an initial perturbation, and can reveal features to the growth that were not observed in this study.
- Turbulence is often driven by shear in the ABL. This study focused solely on a convective system. An understanding would benefit from similar studies applied to a shear driven boundary layer growth.
- A further step to combine the two parts of this study is the application of the data assimilation techniques studied for the Lorenz model to predictions using LES and DNS simulations. It would make a more realistic forecasting study, similar to the practices of Numerical Weather Prediction. How far do these methods assist predictions in resolved turbulence could improve the scope of these high resolution simulations for forecasting.

Acknowledgments

My desire to do this research stemmed somewhere from the stimulating discussions I had with my supervisor *Harm Jonker* during his lectures on *Chaotic Processes* and *Atmospheric Science*. I deeply thank him for having suggested this work as my master thesis project, bringing together my interests, and guiding me into a process of learning that I have grown to immensely enjoy. This learning, however, was fraught with nuances which I discovered in the course of my work, an understanding of which was largely aided by *Jerôme*, who was always kind to answer even the most trivial queries, explaining phenomena and programming alike. Discussions with him were vital in steering this work into coherence, and I thank him for his continued motivation and witty reasoning.

I also thank the entire Atmospheric Physics group, with Pier, Stephan, Johan, Patrick, Vincent, Sara, Jessica and the masters students Louise, Marijke and Chiel for making the duration of this work an experience I shall forever cherish. I specially thank Bauke for his help, and also Erwin, who made sure the network behave predictably.

APPENDIX **A**

Lorenz Model

A.1 Integration Schemes

A fourth order explicit Runge Kutta scheme is used for integrating the Lorenz Model. The 3 ODEs (Eq. 2.1) can be expressed in the vector form as

$$\dot{\vec{x}} = \vec{f}(\vec{x})$$

where $\vec{x} = (x, y, z)$ and $\vec{f} = (fx, fy, fz)$. Furthermore, $\vec{x}_n$ is the value at time t_n and $\vec{x}_{n+1}$ is the value at time t_{n+1}. Given an initial condition and the integration time step dt, the Runge Kutta method works as

$$\begin{aligned}
\vec{a}_n &= \vec{f}(\vec{x}_n) \\
\vec{b}_n &= \vec{f}\left(\vec{x}_n + \frac{dt}{2}\,\vec{a}_n\right) \\
\vec{c}_n &= \vec{f}\left(\vec{x}_n + \frac{dt}{2}\,\vec{b}_n\right) \\
\vec{d}_n &= \vec{f}(\vec{x}_n + dt\,\vec{c}_n)
\end{aligned} \tag{A.1}$$

The value at the next step is then given as

$$\vec{x}_{n+1} = \vec{x}_n + \left(\frac{dt}{6}\right)(\vec{a}_n + 2\vec{b}_n + 2\vec{c}_n + \vec{d}_n) \tag{A.2}$$

The value of time step is taken to be $dt = T/50$ if $T < 0.1$ and $dt = 0.001$ otherwise (where T is the interval length in DA).

A.2 Forecasting in the Lorenz Model

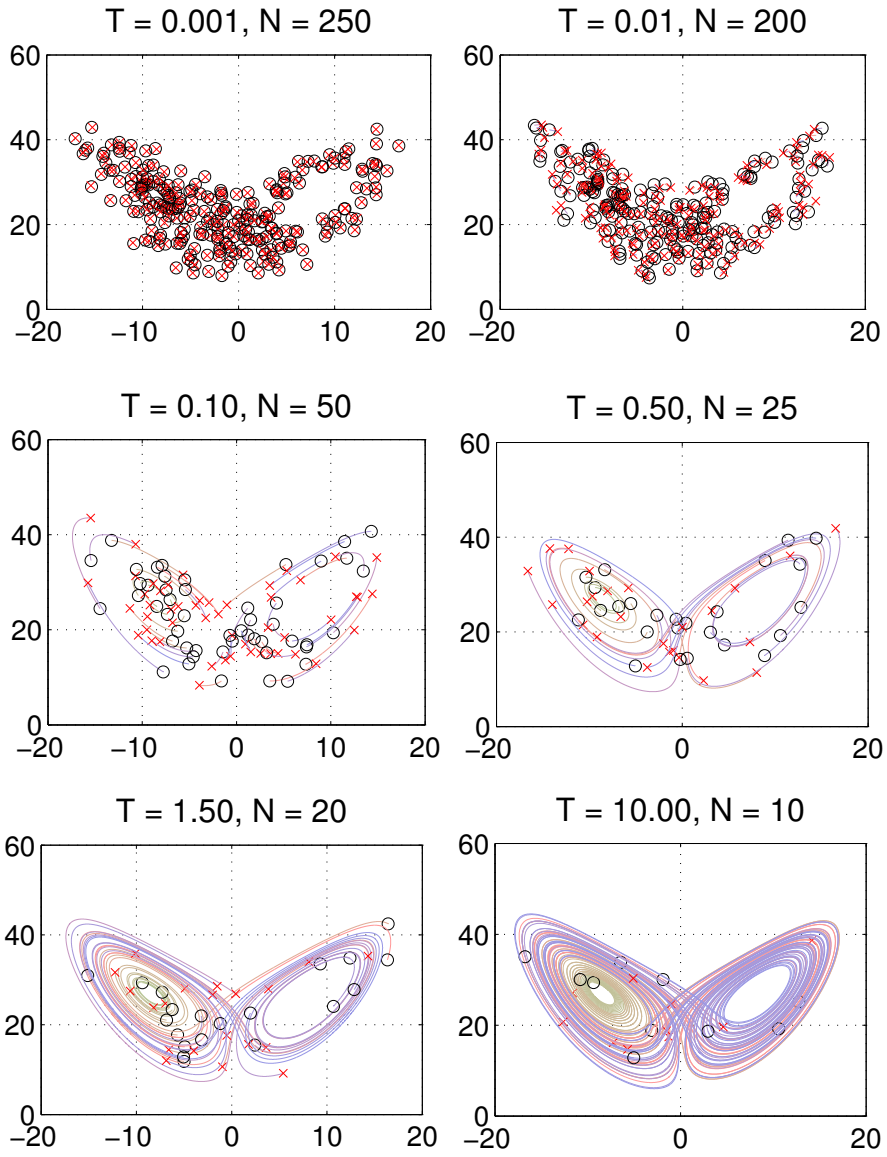

Figure A.1: Trajectories for different durations from random points on the attractor show how much of the attractor is swept in the length of the interval T. It is seen that around $T = 1.5$, the trajectories start to go around one wing of the attractor. This timescale also shows a peak in the power spectrum and is hence relevant for forecasting.

Bibliography

George Keith Batchelor. *The theory of homogeneous turbulence*. Cambridge university press, 1953.

Mrs RC Bell, Jean P Richter, et al. *The Notebooks of Leonardo Da Vinci*, volume 2. Dover-Publications. com, 1970.

Vilhelm Bjerknes. *Das Problem der Wettervorhersage: betrachtet vom Standpunkte derMechanik und der Physik*. 1904.

JW Deardorff, GE Willis, and BoH Stockton. Laboratory studies of the entrainment zone of a convectively mixed layer. *Journal of Fluid Mechanics*, 100(01):41–64, 1980.

John J Finnigan and JC Kaimal. *Atmospheric boundary layer flows*. Oxford university press, 1994.

T Heus, CC van Heerwaarden, HJJ Jonker, A Pier Siebesma, S Axelsen, K Dries, O Geoffroy, AF Moene, D Pino, SR de Roode, et al. Formulation of and numerical studies with the dutch atmospheric large-eddy simulation (dales). *Geoscientific Model Development Discussions*, 3 (1):99–180, 2010.

Brian R Hunt and James A Yorke. Maxwell on chaos. *Nonlinear Science Today*, 3(1):1, 1993.

Eugenia Kalnay. *Atmospheric modeling, data assimilation, and predictability*. Cambridge university press, 2003.

CE Leith and RH Kraichnan. Predictability of turbulent flows. *Journal of the Atmospheric Sciences*, 29(6):1041–1058, 1972.

Edward N Lorenz. Deterministic nonperiodic flow. *Journal of the atmospheric sciences*, 20(2): 130–141, 1963.

Edward N Lorenz. The predictability of a flow which possesses many scales of motion. *Tellus*, 21(3):289–307, 1969.

JL Lumley. Some comments on turbulence. *Physics of fluids A*, 4(2):203–211, 1992.

Peter Lynch. *The emergence of numerical weather prediction: Richardson's dream*. Cambridge University Press, 2006.

Allen Mandelbaum et al. The divine comedy of dante alighieri: Inferno. 1980.

Benoit B Mandelbrot. *The fractal geometry of nature*, volume 173. Macmillan, 1983.

Gordon E Moore et al. Cramming more components onto integrated circuits, 1965.

Rebecca E Morss, Chris Snyder, and Richard Rotunno. Spectra, spatial scales, and predictability in a quasigeostrophic model. *Journal of the Atmospheric Sciences*, 66(10):3115–3130, 2009.

AM Oboukhov. Some specific features of atmospheric turbulence. *J. Fluid Mech*, 13(1):77–81, 1962.

Alan V Oppenheim, Ronald W Schafer, John R Buck, et al. *Discrete-time signal processing*, volume 2. Prentice-hall Englewood Cliffs, 1989.

Lewis Fry Richardson and Sydney Chapman. *Weather prediction by numerical process*. Dover publications New York, 1965.

R Rotunno and C Snyder. A generalization of lorenz's model for the predictability of flows with many scales of motion. *Journal of the Atmospheric Sciences*, 65(3):1063–1076, 2008.

John H Seinfeld and Spyros N Pandis. *Atmospheric chemistry and physics: from air pollution to climate change*. John Wiley & Sons, 2012.

Colin Sparrow. *The Lorenz equations: bifurcations, chaos, and strange attractors*, volume 41. Springer-Verlag New York, 1982.

Peter P Sullivan and Edward G Patton. The effect of mesh resolution on convective boundary layer statistics and structures generated by large-eddy simulation. *Journal of the Atmospheric Sciences*, 68(10):2395–2415, 2011.

Peter P Sullivan, Chin-Hoh Moeng, Bjorn Stevens, Donald H Lenschow, and Shane D Mayor. Structure of the entrainment zone capping the convective atmospheric boundary layer. *Journal of the atmospheric sciences*, 55(19):3042–3064, 1998.

O. Talagrand. Assimilation of observations, an introduction. *Journal of the Meteorological Society of Japan*, 75:191–209, 1997.

John M Wallace and Peter V Hobbs. *Atmospheric science: an introductory survey*, volume 92. Academic press, 2006.